

# Optical Studies of DNA-wrapped Carbon Nanotubes

by

Shin Grace Chou

Submitted to the Department of Chemistry  
in partial fulfillment of the requirements for the degree of

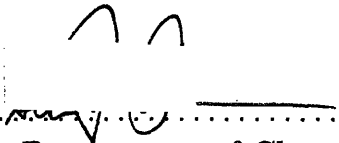
Doctor of Philosophy


at the


MASSACHUSETTS INSTITUTE OF TECHNOLOGY

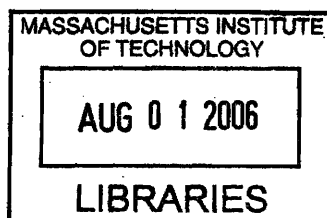
June 2006

© Massachusetts Institute of Technology 2006. All rights reserved.

Author .....  .....  
Department of Chemistry  
May 20, 2006

Certified by .....  .....  
Mildred S. Dresselhaus  
Institute Professor  
Thesis Supervisor


Accepted by .....  .....  
Robert Field  
Chairman, Department Committee on Graduate Students



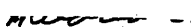
ARCHIVES

This doctoral thesis has been examined by a committee of the Department of Chemistry as follows:


Professor Sylvia Ceyer

  
\_\_\_\_\_  
Chairman

Professor Mildred S. Dresselhaus

  
\_\_\_\_\_  
Thesis Supervisor

Professor Andrei Tokmakoff

\_\_\_\_\_  


# Optical Studies of DNA-wrapped Carbon Nanotubes

by

Shin Grace Chou

Submitted to the Department of Chemistry  
on May 20, 2006, in partial fulfillment of the  
requirements for the degree of  
Doctor of Philosophy

## Abstract

This thesis presents a series of detailed optical studies of phonon-assisted relaxation processes in DNA-wrapped single walled carbon nanotubes. Using resonance Raman spectroscopy (RRS) and photoluminescence spectroscopy (PL), a careful characterization has been carried out on different DNA-wrapped SWNT samples to study the effects of DNA wrapping on the electronic and vibrational structure of SWNTs. Then, by using a DNA-wrapped SWNT sample that is highly enriched in (6, 5) SWNTs, I was able to separately identify the individual phonon-assisted relaxation channels that could not be clearly observed in bulk materials system. In light of the recent developments in the excitonic theory of 1D systems in general and of 1D carbon nanotubes in particular, the observed phonon-assisted processes are interpreted and examined in terms of excitonic states. An intense up-shifted phonon-assisted transition observed in PL spectra of SWNTs suggests the presence of a strongly coupled exciton-phonon bound state due to the strong 1D confinement condition. The presence of such exciton-phonon bound state confirms the excitonic nature of the optical transitions observed in semiconducting SWNTs.

To further understand the role of phonon assisted processes in exciton relaxation, the dynamics of such phonon-assisted processes has been studied using time-resolved spectroscopy. By using a carefully chosen  $E_{\text{pump}}$  that corresponds to  $E_{11}^{0A_2}(6, 5) + 2\hbar\omega_D$  and probing at  $E_{11}^{0A_2}(6, 5)$ , an intermediate decay time component that is associated with the hot D-band phonon-absorption and relaxation process is identified and studied in detail. The experimental results suggest that in the event of a multi-phonon assisted relaxation process, it is possible for an additional excitonic state to participate in the relaxation process and to give rise to an intermediate relaxation time component. The detailed information obtained from the experimental studies clarifies the role of hot phonon absorption and emission processes, as well as the Auger process, in the filling and depletion of band edge exciton populations for individual SWNTs. The experimental result also gives insights into how dark excitons, which are predicted by theory, might indirectly participate in the exciton relaxation process.

Lastly, to further understand the structural-property relation for short nanotubes, a series of RRS studies have been carried out on DNA-wrapped SWNTs samples

that are sorted by length using size exclusion chromatography. The consequences of broken translational symmetry in short SWNTs are examined by monitoring the intensities of the Raman features in the extended intermediate frequency mode (IFM) region between  $600\text{cm}^{-1}$  and  $1500\text{cm}^{-1}$ . Many of the IFM features show an increased Raman cross section with decreasing average length of the nanotubes. The extent of the Raman intensity increase is found to be dependent on the origin of the IFM features. The changes in the D-band intensity are also examined in the context of the crystalline size effect as the nanotubes become shorter.

Thesis Supervisor: Mildred S. Dresselhaus

Title: Institute Professor

## Acknowledgments

To begin with, I would like to thank the members of my family for their love and support. During a time in Taiwan when rote memorization is used interchangeably with the term "education", my parents have taught me to keep an open mind, to ask questions, and to seek answers. Over the years, my brother Henry has been the quiet force that pushes me forward and kept my feet to the ground in this foreign land, populated with foreign people and their foreign ways. My grandparents, aunts, uncles, and cousins from both Taiwan and US have also generously and unconditionally offered their love and support throughout the past nine years I study in the US. I am very grateful.

Working for Drs. Millie and Gene Dresselhaus has been the best decision I have ever made in my life, and I must thank them for providing me with the opportunity to work with them. Millie has taught me the ways to achieve greatness through scientific excellence and through helping others. Her passion for science is not only overwhelming but also contagious. Gene has taught me the intuitive approach for solving physical problems, as well as the various survival principles of the academic jungle. Together, they have provided me with a support network that allows me to pursue my research interests, with the tools and the resources I needed. More importantly, they have helped me to grow into the young scientist I have aspired to become.

Professionally, I was blessed with the opportunity to learn from many of the most talented scientists in the field. I am grateful for the guidance and the support from our brilliant Brazilian collaborator Dr. Ado Jorio, Dr. Marcos Pimenta, Dr. Flavio Plentz and Dr. Antonio Souza Filho. The work of Dr. Adelina Santos has shaped the earlier part of my project, and Dr. Christiano Fantini, Mauricio Souza and Henrique Ribeiro have helped me in numerous occasions throughout the frequency domain optical studies. On the opposite side of the globe, I am grateful for the opportunity to work with the first-class nanotube theory team in Sendai, Japan (R. Saito sensei and Dr. J. Jiang). The team has never failed to provide compelling insights into my

experimental observations. These insights have shaped the directions of my research, as the field of nanotube optics transition from a band-to-band model to an excitonic model. The talented team from Boston University (Prof. Anna Swan, Prof. Bennet Goldberg, Dr. Yin Yan, and Andy Walsh) has also helped me throughout the years in a number of frequency domain experiments with their sophisticated micro-Raman system. I am especially thankful to Professor Anna Swan for her mentoring during my early years in graduate school.

I was fortunate to have the opportunity to work with Dr. M. Decamp at Professor Andrei Tokmakoff's lab on the time-resolved experiments. The technical expertise of the Tokmakoff group in two-color IR pulse generation has provided me with high quality IR pulses in the desired energy region. The availability of such high quality IR pulses has led to the success of my experiments. I am thankful to Dr. Decamp for teaching me about time-resolved experiments and IR pulse generation, using a specially designed parametric amplification system.

I thank the Dupont-MIT alliance for supporting my work throughout most of my graduate career. Our collaboration with scientists at Dupont has been a fruitful one. The scientific achievement of Dupont scientists Dr. Ming Zheng, Dr. Bibiana Onoa, and Elen Semke has allowed me to tackle my research project using a unique sample that is tailored to the problem. I am also thankful to the local DMA team (Prof. Yet-Ming Chiang, Caroline Lau, and Dr. Elen Humphrey) who have provided me with regular feedback for my work over the past four years.

The local MGM team at MIT has provided me with supports on all aspects of my graduate life. Laura, her beautiful voice ringing down the hall, as well as her flawless administrative work over the years, have kept me out of trouble. Dr. Yu-Ming Lin, Dr. Marcie Black, and Dr. Steve Cronin have taught me many things on group theory and solid state physics. More importantly, they have introduced me to the mysterious yet enlightening existence of life after graduate school, and I will remember to pass the message on to younger students. My ex-officemate Georgii is the quiet stabilizing force of the group who quietly and patiently grinds away the computer and physics problems we run into over the years. The group will be

lost without him. I am also grateful to his guidance throughout my earlier years in the group. Bin is an amazing engineer who has single handedly built the tunable Raman system in the George Harrison Spectroscopy lab. I owe the success of many later frequency domain experiment to him and the lab he built. My gratitude also goes to other members of MGM: Federico, Ming, Eduardo, Aurea, Dan, and Mario. Their friendship and support have made MIT a much more tolerable place. Their creative approaches to problems and their scientific insights have also helped me, on numerous occasions, in formulating BS models that eventually turn into scientific interpretation of experimental data. Professor Jing Kong and her faith in God has offered me inspirations during the self-reflection phase in the last year of my graduate study. The friendship, the support, and the free mango strips provided by the Jing Kong group (Bin, Dan, Aurea, Stevie, Alfonso, and Hootan) have also lighten up the dark, snowy days in building 13.

My friends at MIT have helped me through the roller-coaster ride of my graduate years. Dr. Yin Thai Chan and Bryan Wong have cheered me on over the years with their Asian pessimism. The girly chatters with Jelena Mirkovic are always sources of joy and comfort. I also acquire courage and inspiration from Riccardo Signorelli and his romantic vision for life in the midst of many angst and frustration-filled time. Furthermore, my gratitude goes to many of my friends from TAS and Bryn Mawr College. Their worldly wisdom and advices have helped me keep the academic environment in perspective.

At the end, I would like to thank my teachers and mentors who have continued to believe in me after I left Bryn Mawr College. The encouragement and support of Dr. Ed Wovchko from Bryn Mawr college has kept me afloat through the strenuous first year of graduate school. Dr. Michelle Francl from Bryn Mawr College and Dr. David Pratt from University of Pittsburgh (my undergraduate research supervisors) have helped me discovered the beauty of scientific research, and they were always willing to offer advice and has remained a source of encouragement over the years.

# Contents

<b>1</b>	<b>Introduction</b>	<b>22</b>
<b>2</b>	<b>Background</b>	<b>25</b>
2.1	Structure and Notation of SWNTs . . . . .	26
2.1.1	Electronic Structure . . . . .	30
2.1.2	Phonon Structure . . . . .	32
2.2	Resonance Raman Scattering Processes . . . . .	34
2.3	Resonance Raman Spectroscopy of SWNTs . . . . .	36
2.3.1	First order Raman Spectra . . . . .	36
2.3.2	Overtones and Second Order Features . . . . .	41
2.4	PL Spectroscopy and beyond . . . . .	52
2.5	Exciton Formalism and Optical Selection Rules . . . . .	54
<b>3</b>	<b>Nanotube Growth and Separation</b>	<b>57</b>
3.1	Introduction . . . . .	57
3.2	Controlled Growth of SWNTs . . . . .	57
3.2.1	CO Chemical Vapor Deposition . . . . .	59
3.3	Nanotube Separation . . . . .	63
3.3.1	Polymer and DNA-assisted Dispersion and Separation . . . . .	63
3.3.2	Length Sorting . . . . .	65
3.4	Summary . . . . .	67
<b>4</b>	<b>Optical Characterization of DNA-wrapped SWNTs</b>	<b>68</b>



4.1	Introduction . . . . .	68
4.2	Experimental . . . . .	70
4.3	Resonance Raman Characterization Based on First Order Raman Features . . . . .	71
4.3.1	RBM . . . . .	71
4.3.2	G-band . . . . .	73
4.4	$E_{ii}$ Determination . . . . .	75
4.4.1	$E_{22}^S$ Determined from RRS anti-Stokes to Stokes Intensity Ratio . . . . .	75
4.4.2	Photoluminescence (PL) Measurements . . . . .	80
4.4.3	Learning From Excitonic Transition Energies . . . . .	84
4.5	Concluding Remarks: New Opportunities . . . . .	85
<b>5</b>	<b>Phonon-assisted Excitonic Recombination Channels Observed in the Frequency Domain</b> . . . . .	<b>87</b>
5.1	Introduction . . . . .	87
5.2	Experimental . . . . .	88
5.3	Phonon-Assisted Processes . . . . .	89
5.3.1	Multi-Phonon Processes . . . . .	91
5.3.2	One Phonon Process and Phonon Sideband . . . . .	96
5.3.3	Hot Phonons . . . . .	97
5.3.4	Fluorescence Resonance Energy Transferring . . . . .	98
5.4	Summary - Phonon Assisted Processes in 1D Systems . . . . .	100
<b>6</b>	<b>Time Domain Study of Phonon-Assisted Processes in DNA-wrapped SWNTs</b> . . . . .	<b>102</b>
6.1	Introduction . . . . .	102
6.2	Experimental . . . . .	104
6.3	Results . . . . .	105
6.4	Discussion . . . . .	111
6.4.1	State filling via exciton-phonon interactions . . . . .	111
6.4.2	Different Decay Channels . . . . .	113

6.4.3	Probing The Minority Species In The Sample . . . . .	116
6.4.4	Photoinduced Absorption Processes . . . . .	118
6.5	Summary . . . . .	121
<b>7</b>	<b>Finite length effects in DNA-wrapped carbon nanotubes</b>	<b>122</b>
7.1	Introduction . . . . .	122
7.2	Experimental . . . . .	123
7.3	Enhanced Features in the Extended IFM Region . . . . .	124
7.3.1	Length-Dependent Intensity Evolution . . . . .	125
7.4	Other Crystalline Size Effects in Carbon Nanotubes . . . . .	133
7.4.1	D-band intensities and End-Cap Effects . . . . .	133
7.5	Other Second Order Raman Features . . . . .	136
7.6	Summary . . . . .	137
<b>8</b>	<b>Conclusions</b>	<b>139</b>
8.1	Conclusions . . . . .	139
8.2	Future Studies . . . . .	141

# List of Figures

2-1	The unrolled honeycomb lattice of a nanotube. When we connect sites $O$ and $A$ , and sites $B$ and $B'$ , a nanotube can be constructed. The vectors $OA$ and $OB$ define the chiral vector $\mathbf{C}_h$ and the translational vector $\mathbf{T}$ of the nanotube, respectively. The rectangle $OAB'B$ defines the unit cell for the nanotube. The figure is constructed for an $(n, m) = (4, 2)$ nanotube [1]. . . . .	26
2-2	(a) The unit cell containing sites A and B where carbon atoms are located, and (b) the Brillouin zone of a graphene or two-dimensional graphite layer are shown as the dotted rhombus and the shaded hexagon, respectively. The vectors $\mathbf{a}_i$ , and $\mathbf{b}_i$ , ( $i = 1, 2$ ) are basis vectors and reciprocal lattice vectors, respectively. The high symmetry points, $\Gamma$ , $K$ and $M$ are indicated [2]. . . . .	28
2-3	(a) The calculated constant energy contours for the conduction and valence bands of a graphene layer in the first Brillouin zone using the $\pi$ -band nearest-neighbor tight-binding model [1]. Solid curves show the cutting lines for the $(4, 2)$ nanotube [3]. (b) Electronic energy band diagram, $E(\mathbf{k})$ for the $(4, 2)$ nanotube obtained by zone-folding from (a). (c) Density of electronic states for the band diagram shown in (b). . . . .	31
2-4	Phonon dispersion relation of graphite, calculated using the force constants determined by fitting of the experimental points obtained from electron energy loss spectroscopy, inelastic neutron scattering, velocity of sound, and X-ray diffraction techniques [4-6] . . . . .	33

- 2-5 (a) The calculated phonon dispersion relations of an armchair carbon nanotube with  $(n, m) = (10, 10)$ . The number of degrees of freedom is 120 and the number of distinct phonon branches is only 66 because of the degeneracy of these modes due to symmetry arguments [1]. (b) The corresponding phonon density of states for a (10,10) nanotube [7]. (c) The corresponding phonon density of states for a 2D graphene sheet [1]. . . . . 35
- 2-6 (a) Raman spectra from HiPco SWNT bundles (see text) [8]. (b) Raman spectra from a metallic (top) and a semiconducting (bottom) SWNT at the single nanotube level. The spectra show the radial breathing modes (RBM), *D*-band, *G*-band and *G'* band features, in addition to weak double resonance features associated with the *M*-band and the iTOLA second-order modes [9]. The isolated carbon nanotubes are sitting on an oxidized silicon substrate which provides contributions to the Raman spectra denoted by ‘\*’, and these Si features are used for calibration purposes [10]. . . . . 37
- 2-7 The Raman-active modes of A, E<sub>1</sub>, and E<sub>2</sub> symmetries and the corresponding cutting lines  $\mu = 0$ ,  $\mu = \pm 1$ , and  $\mu = \pm 2$  in the unfolded 2D Brillouin zone. The  $\Gamma$  points of the cutting lines are shown by solid dots. The table gives irreducible representations and basis functions for the Raman-active modes according to group theory. The Z axis is parallel and the XY plane is perpendicular to the nanotube axis. [1, 11] 37
- 2-8 Polarization scattering geometry dependence for the *G*-band from two (a) and (b) isolated SWNTs in resonance with  $E_{\text{laser}} = 2.41$  eV. The Lorentzian peak frequencies are in  $\text{cm}^{-1}$ .  $\theta'_S$  and  $\theta''_S$  are the initial angles between the light polarization and the SWNT axis directions, not known a priori. From the relative intensities, and the polarization behavior of the *G*-band modes, we assign  $\theta'_S \sim 0^\circ$  and  $\theta''_S \sim 90^\circ$  [12]. . 40

2-9	(a) First-order and (b) one-phonon second-order, (c) two-phonon second-order, resonance Raman spectral processes: (top) incident photon resonance and (bottom) scattered photon resonance conditions. For one-phonon, second-order transitions, one of the two scattering events is an elastic scattering event (dashed lines). Resonance points are shown as solid circles[13]. See text for details. . . . .	41
2-10	(a) Calculated Raman frequencies for the double resonance condition as a function of $E_{\text{laser}}$ (bottom axis) and the $q$ vector along $\Gamma$ -K (top axis). Solid and open circles correspond to phonon modes near the $K$ and $\Gamma$ points, respectively. (b) The 6 graphite phonon dispersion curves (lines) and experimental Raman observations (symbols) are placed according to double resonance theory [14]. . . . .	43
2-11	Lorentzian fits of the Raman spectra taken at several $E_{\text{laser}}$ values for the $M$ feature near $1750 \text{ cm}^{-1}$ and the highly dispersive iTOLA feature observed at $1950 \text{ cm}^{-1}$ in SWNT bundles [9]. Peak frequencies ( $\text{cm}^{-1}$ ) and $E_{\text{laser}}$ values (eV) are displayed. . . . .	47
2-12	(a) Two-dimensional plot for the $E_{\text{laser}}$ dependence for the Raman spectra of SWNT bundles in the intermediate frequency mode (IFM) range. The light areas indicate high intensity. Arrows point to five well-defined $\omega_{\text{IFM}}^-$ features. (b) Raman spectra with $E_{\text{laser}} = 2.05, 2.20, 2.34,$ and $2.54 \text{ eV}$ . [15] . . . . .	48
2-13	A Kataura plot that summarizes the calculated relative positions of $E_{ii}$ and $\omega_{\text{RBM}}$ (or $d_i$ ). The red circles denote the transition energies for metallic nanotubes, whereas the green and blue circles denotes different $(2n+m \text{ MOD } 3)$ types. The green circles denote those nanotubes with $(n, m)$ indices such that $(2n+m \text{ MOD } 3 = 1)$ . The blue circles denote the nanotubes whose $(n, m)$ values gives $(2n+m \text{ MOD } 3=2)$ . The more subtle distinction between these two types will be discussed in the later chapters . . . . .	50

2-14	(a) AFM image of SWNTs on a SiO <sub>2</sub> substrate. The inset shows the SWNT diameter distribution of the sample. (b) Raman spectra from three different spots on the Si/SiO <sub>2</sub> substrate. The RBM frequencies (widths) and the $(n, m)$ assignment for each resonant SWNT are displayed [10]. The 303 cm <sup>-1</sup> feature comes from the Si substrate and is used for calibration purposes. (c) Raman intensity <i>vs</i> laser excitation energy for the anti-Stokes RBM feature at the 173.6 cm <sup>-1</sup> assigned to an isolated (18, 0) SWNT on a Si/SiO <sub>2</sub> substrate [16]. The predicted resonant window is shown by the solid curve, while the vHS in the DOS at 1.655 eV is shown by the dashed curve. Circles and squares indicate two different runs taken over the laser energies. . . . .	51
2-15	A schematic diagram of an excitonic band for a chiral nanotube. The electron, hole and exciton states at the band edges are indicated by a solid circle and labeled according to their irreducible representation. Dark (thicker) lines correspond to the E <sub>μ</sub> 2D representation while the blue lines (thick) correspond the A <sub>1</sub> excitons while the cyan lines (thin) correspond to the A <sub>2</sub> excitonic states. The excitonic band structures shown here are only schematic illustrations. Group theory does not order the values for the eigenenergies or for the energy dispersions. . .	55
3-1	Transmission electron microscopy images of single-walled carbon nanotubes (SWNTs) synthesized by HiPco process [17] . . . . .	59
3-2	Transmission electron microscopy images of single-walled carbon nanotubes (SWNTs) synthesized by CoMoCAT process [17] . . . . .	61
3-3	A comparison of the photoluminescence (PL) spectra of a HiPco and CoMoCAT SWNT suspension that are dispersed in sodium dodecyl sulfate (SDS) solution [18]. The PL characterization shows that the SWNT samples made by the CoMoCAT process have smaller average diameters, and the diameter distribution is narrower, compared to SWNTs made with the HiPco process. . . . .	62

3-4	AFM images of three representative SEC fractions deposited onto alkyl silane-coated SiO <sub>2</sub> substrates [19]. . . . .	66
4-1	(a) A comparison of RBM spectra of CoMoCAT bundles and DNA-wrapped CoMoCAT SWNTs taken under different preparation conditions (see text). b) A comparison of the <i>G</i> -band spectra of different CoMoCAT-based DNA-SWNT samples taken with 2.19eV laser excitation (see text). After the bundles are broken up by DNA-wrapping, the different species within the bundle only interact weakly. A magnified trace for bulk CoMoCAT SWNT materials is shown in (c). The spectrum was fitted using Lorentzian functions, and the weak <i>E</i> <sub>2</sub> components that only occur in as-grown materials have been identified. . . . .	72
4-2	(a) shows a resonance window measured for a SDS-wrapped, HiPco SWNT sample dispersed in solution, reported in Fantini et al. [8]. (b) shows a resonance window of bundled HiPco SWNT sample, as previously reported in Fantini et al. [8]. (c) shows the resonance window measured for dried DNA-wrapped CoMoCAT SWNT. The average width of the resonance window for this sample is much smaller compared to that for SDS-wrapped SWNTs in solution or the bundled SWNTs sample. The solid lines here denote the Stokes profiles whereas the dotted lines denote the anti-Stokes profiles for samples in different environments. Since the SWNT here has a different ( <i>n, m</i> ) from the one shown in Fantini et al. [8], the transition energy is different. The general trends in the width of the window for the same SWNTs in different environment are the same. . . . .	77

- 4-3  $E_{22}^S$  determined from the temperature-normalized  $I_{AS}/I_S$  ratios of the RRS spectra, plotted against  $\omega_{RBM}$ , showing the  $(2n+m=\text{constant})$  family behavior. Colored data points denote the two DNA-wrapped samples with different S:M ratios (see text), measured with both the RRS and PL techniques. The  $E_{22}^S$  values are determined from RRS and PL measurements, whereas the values of  $E_{11}^S$  values are determined from the PL emission of encapsulated SWNTs. . . . . 78
- 4-4 A slice of the 2D contour plot of excitation vs. emission energies for a section of the PL data for the unfractionated DNA-SWNT sample where  $E_{22}^S \rightarrow E_{11}^S$  absorption-emission transitions are found. The  $(n, m)$  assignments for these transitions can be identified by comparing their energies with the assigned PL transitions for SDS-dispersed HiPco SWNTs [20]. Note that the  $(8, 6)$  transition is denoted by the white circle. The intensity of the transition is too weak to show up with the intensity scale of the present plot. . . . . 81
- 4-5 The upper Figure shows a 2D contour plot of excitation vs. emission energies for a section of the PL data for the fractionated  $(6, 5)$ -enriched DNA-SWNT sample. With the dominant emission profile arising from the  $(6, 5)$  SWNT, the experiment results corroborate the initial sample characterization that suggests  $(6, 5)$  enrichment for the fractionated sample. Furthermore, PL peaks were observed for  $(n, m)$  species in the lower figure that are not observed in the unfractionated sample. The experimental results shows that the fractionation and enrichment process is indeed a highly  $(n, m)$  specific method for separating a nanotube mixture. . . . . 83



- 5-1 (a) A 2D excitation vs. emission contour map for a dried (6, 5)-enriched DNA-SWNT sample on a sapphire substrate. The spectral intensity is plotted using the log scale shown on the right. (b) A schematic view of the observed PL transitions. The blue vertical band denotes emission at  $E_{11}^0$ . The horizontal gray bands, denote the nearly-continuous luminescence processes associated with the thermally excited processes in the different phonon branches. The cut-off energy at 1.06 eV is marked in green. Orange dotted lines denote PL emission from resonant Raman scattering processes for G-band, M-band, and G'-band phonons. Strong PL emission spots at  $E_{11}^0=1.255$  eV, denoted by the red circles, are associated with one-phonon (VI) and two-phonon (I to V) processes described in Fig. 5-2 (see text). . . . . 90
- 5-2 Schematic diagrams for the different phonon-assisted processes (see text). (a) The commonly reported [20–24] excitonic recombination mechanism for the (6, 5) nanotube. The process involves excitonic absorption at  $E_{22}^0$  (point b). The excited exciton can relax down to  $E_{11}^0$  (point c) via multiple channels, and can recombine at  $E_{11}^0$ . The red boxes labeled as “ex” and “em”, respectively, denote the range of excitation and emission energies in Fig. 5-1. Since the excitation range is lower than  $E_{22}^0$ , the process shown in (a) is not observed in the present report. (b) Corresponds to the two-phonon assisted processes responsible for transitions I to V shown in Fig. 5-1(b). (c) Corresponds to the one-phonon assisted processes responsible for transition VI shown in Fig. 5-1(b). (d) Corresponds to the nearly continuous vertical transitions at the band edge  $E_{em}=1.255$  eV. (e) Corresponds to the thermally-excited processes that are associated with the horizontal streaks shown across the PL map in Fig. 5-1(b). . . . . 92

5-3	A magnified portion of the a 2D excitation vs. emission contour map shown in Fig. 5-1(a), emphasizing the intersection between the non-resonant Raman series and the band edge transitions. The peak shown is associated with the two D-band phonon assisted process (or $G'$ ) is observed along the band edge emission axis at 1.255eV, as shown with the vertical line, excited at $E_{laser} = 1.58 \pm 0.005 \text{eV}$ , as shown with the horizontal brown dotted line. On the other hand, at the same excitation energy, the non-resonant Raman transition seems to occur between 1.257 and 1.258eV, which yields at slightly shifted phonon energy. In general, similar shift of $\sim 2\text{-}3 \text{meV}$ has been observed for the series of non-resonant Raman processes observed in PL maps. . . . .	95
5-4	A 2D excitation vs. emission contour map for an as-prepared CoMoCAT-based DNA-SWNT sample in solution. . . . .	99
5-5	A schematic of an additional channel of electron relaxation, in which the photon emitted from electron relaxation of a small diameter SWNT becomes a source of excitation energy for another larger diameter SWNT. . . . .	99
6-1	A transient spectrum monitoring the DT intensity vs. delay time, for $E_{probe} \sim E_{11}^{0A_2}(6,5)$ at 1.252eV, for a (6,5) enriched DNA-wrapped nanotube sample, pumped with $E_{pump} \sim 1.567 \text{eV}$ (pump fluence level fixed at $0.1 \text{J/m}^2$ ). The $\Delta T/T_o$ data are plotted on a natural log scale. The inset shows a magnified portion of the plot to show the range of the delay time pertinent to $\tau_{int}$ more clearly. . . . .	106

- 6-2 Fluence dependence of the different components in the relaxation dynamics for  $E_{\text{probe}} \sim 1.252\text{eV}$ . The dotted lines are guides to the eyes. The faster components were measured with higher time resolution (40fs), over 20ps. To determine  $\tau_{\text{slow}}$  more accurately, fluence-dependent experiments were carried out over 50ps with lower time resolution (120fs) and a higher pump fluence. Fluence dependence of the (a) two faster components corresponding to intraband processes and the (b) slower component corresponding to the dynamics of the interband recombination. (c) Shows that for the initial 20ps of the decay process, the relative weight for the intermediate process increases with the pump fluence. . . . . 108
- 6-3 The schematic diagram and the respective DT spectra for five different probe energies. (a) A schematic diagram of different values of  $E_{\text{probe}}$  relative to the band edge energies of different nanotubes. The values of  $E_{\text{probe}}$  from  $O_1$  to  $O_5$ , respectively, are 1.158eV, 1.198eV, 1.222eV, 1.252eV, and 1.272eV. (b)DT spectra for different values of  $E_{\text{probe}}$ . Notice that DT changes sign as  $E_{\text{probe}}$  moves in and out of resonance with the (6, 5) and (7, 5) nanotubes. We use the dotted lines as guides for the eyes to mark the zero DT line for the respective DT spectra. The positive DT intensities are normalized to the maximum DT intensity to aid with the lineshape comparison. . . . . 109
- 6-4 (a)A schematic diagram of relaxation from  $a$  to the  $0A_2$  excitonic state  $c$  by emitting two D-band phonons (see text). The black arrow denotes a fast phonon emission process originating from an exciton-bound phonon state, whereas the gray arrow denotes a slow process originating from a real excitonic state. (b)A schematic diagram of a scenario in which the band edge exciton population can be depleted via phonon-absorption. The pump-probe experiment was carried out for the case where  $E_{\text{probe}} = E_{11}^{0A_2}(6, 5)$ , corresponding to point  $c$ . . . . . 113

- 6-5 Schematic diagram of two possible scenarios for the photoinduced absorption process when  $E_{\text{probe}}$  does not correspond to excitonic band edge energies. (a) A band edge exciton at  $o$  is created by exciting an electron from the ground state  $z$  to a virtual state  $v$  and then combining with an optical phonon to reach state  $o$ . (b) A band edge exciton at  $o$  can combine with a photon and access a higher continuum mobile band state at  $E_{ii}^{0A_2}$ , denote by  $h$ . . . . . 119
- 7-1 a) A comparison of the resonance Raman spectra for an ensemble of an as-grown SWNT sample wrapped with DNA (not fractionated) and three SWNT samples with an average length of 50nm, 70nm, and 100nm, respectively, that had been fractionated using SEC [19]. The spectra were taken with an excitation energy 647nm(1.92eV), which is highly in resonance with the (7,5) SWNT species. The inset to the figure shows a magnified portion of the modes in the extended IFM region. All four spectra are normalized with respect to their G-band intensities. b) Shows the difference spectra between the finite-length sample and the as-grown sample in the extended IFM region between  $600 - 1500\text{cm}^{-1}$ . The spectra in (b) were obtained by subtracting the spectra of the DNA-wrapped, as-grown sample from the spectra from each of the three short samples. . . . . 126
- 7-2 (a) Evolution of the *increase* in the relative IFM intensity, with respect to the G-band intensity ( $I_{IFM}/I_G$ ), as the average length of the nanotubes decreases from 100nm to 50nm. The relative intensities are plotted as a function of inverse nanotube length for  $E_{\text{laser}} = 647\text{nm}$  (1.92eV) and  $E_{\text{laser}} = 640\text{nm}$  (1.93eV) (b) A comparison of RBM features excited by 640nm and 647nm. The dominant RBM feature at  $297\text{cm}^{-1}$  corresponds to the (7,5) SWNTs. The normalization of the spectra are to the G-band intensity in all cases. . . . . 127

7-3	Resonance Raman spectra in the RBM and IFM regions of DNA-wrapped SWNTs with different average lengths, taken at (a) $E_{laser} = 679\text{nm}$ (1.83eV), (b) $E_{laser} = 640\text{nm}$ (1.97eV), and (c) $E_{laser} = 620\text{nm}$ (2.00eV). The values of $E_{laser}$ , respectively, emphasize (a) (8, 3) (b) (7, 5), and (c)(7, 5) and (11, 1) semiconducting SWNT species. . . . .	132
7-4	(a)D-band intensities (normalized to that of the G-band) plotted as a function of inverse nanotube length, excited at different excitation energies (b) Normalized D-band to G-band intensity ratio, $I_D/I_G$ , for DNA-wrapped SWNTs of different lengths plotted as a function of laser excitation energy. . . . .	134
7-5	A comparison between the length dependence of the $I_D/I_G$ ratio for short nanotubes samples, excited at multiple laser excitation energies, and the universal relation for the crystalline size dependence of the $I_D/I_G$ ratio in graphite, empirically determined from nanographites. [25]	137
8-1	(a) Shows a comparison of the intensity of combination modes for different samples that have gone through different wrapping and fractionation procedure. The spectra were taken using $E_{laser} = 1.63\text{eV}$ . . . . .	142

# List of Tables

2.1	Properties of the various Raman features in graphite and SWNTs. <sup>1)</sup>	45
4.1	Transition Energies of DNA-SWNT Hybrids . . . . .	84
5.1	Assignments of the strong PL spots in Fig. 5-1 to the different optical phonon branches of the (6, 5) nanotubes . . . . .	93
6.1	Decay times and weights of the individual processes measured at different probe energies . . . . .	117
7.1	IFM frequencies and their assignments . . . . .	133

# Chapter 1

## Introduction

Carbon nanotubes have attracted a great deal of attention as a model 1D materials system since the inception of the research field. The interest in carbon nanotubes stems from their unique structure and properties that both mirror and contrast their bulk counterpart. The unique geometric structure renders the possibility for carbon nanotubes to be either metallic or semiconducting, depending on their structures. The strongly confined structure and the possibility of high structural perfection in carbon nanotubes also gives rise to their ballistic transport properties. Due to the simplicity of nanotube structures, consisting of one atomic species arranged in a hexagonal lattice, it is also possible to perform detailed calculations of the unique properties of single walled carbon nanotubes (SWNTs).

The advances in the carbon nanotube field has provided scientists a good understanding of their structure and of many of their basic properties. This knowledge is now in place, together with an appreciation of the interrelation between the structure and properties. Many unexpected phenomena that do not occur in the parent graphite material have been discovered in nanotubes, and these discoveries have energized not only nanotube research, but also nanoscience research more generally. On the other hand, major gaps in our basic knowledge remain. The photo-physics of nanotubes has received considerable attention as a means for studying electron, phonon, and optoelectronic phenomena in one dimensional systems, due to the sharp resonance enhancement effect. Since Raman scattering and optical absorption and emission in

SWNTs are resonant processes, depending on the singularities in the 1D density of electronic states, these techniques provide a convenient method for studying SWNTs in a bulk sample.

In this thesis, I will present the findings from a series of optical studies carried out on (6,5)-enriched single walled carbon nanotubes samples wrapped with single-stranded DNA sequence of alternating guanine (G) and thymine (T) units. The availability of such a sample, enriched in a specific  $(n, m)$  species, introduces the possibility to study subtle optical processes that are originally too weak or time consuming to experimentally measure at the single nanotube level. The study has shown that since SWNTs are a strongly confined 1D system, the individual phonon-assisted processes in SWNTs can be well resolved in PL spectra, with spectral features shown in great detail and over a wide energy range. This is a central finding of this thesis. The dynamics of such phonon-assisted relaxation process is further studied in the time domain. In addition, the effects of broken translational symmetry in nanotubes whose lengths are much shorter than the wavelength of light has been explored.

The first part (Chapters 2 – 3) of this thesis presents an introduction to the electronic and vibrational structure of carbon nanotubes. A brief review is presented on the important advances in nanotube growth and separation that have significantly shaped the research described in this thesis. In the second part (Chapters 4 – 5), the thesis describes a detailed study of DNA-wrapped SWNTs in the frequency domain. Chapter 4 describes the detailed Raman and PL characterization of the DNA-wrapped single walled carbon nanotube hybrids that were studied in this thesis. The study investigates the effects of DNA-wrapping on the electronic structure of the nanotubes by looking into the electronic transition energies and the resonance condition of the combination phonon features. Then, Chapter 5 presents a detailed study of phonon assisted processes in 1D systems observed in PL studies of a (6,5)-enriched DNA-SWNTs sample. By looking into excitation energy regions between the first and second resonant electronic transition of the (6,5) SWNTs, different channels of phonon-assisted relaxation processes were studied in detail in the



frequency domain. The detailed frequency domain study is followed by a detailed study of the dynamics of phonon-assisted processes in the time domain. Chapter 6 presents a series of systematic time-resolved experiments that extend the study of phonon-assisted processes in SWNTs into the time domain to study the dynamics of phonon-assisted processes. The study has clarified the possible roles of dark excitons in the relaxation of excited excitons. Evidence of multi-exciton excitation were also observed in the pump-fluence-dependent Auger rates. Then, Chapter 7 presents a survey of finite-length effects in DNA-wrapped SWNTs that are prepared using size-exclusion chromatography. The phonon features that are characteristic of short nanotubes are examined. Lastly, conclusions of this thesis are presented along with suggestions for future research in Chapter 8.

# Chapter 2

## Background

This chapter presents an introduction to the unique electronic and vibrational structure properties of single walled carbon nanotubes (SWNTs), as well as how optical spectroscopy can be used to investigate the unique confinement physics in such one dimensional (1D) systems. The chapter first introduces the notation used for describing the detailed nanotube geometry in relation to the structure of 2D graphite. The chapter then discuss the optical properties observed in SWNTs due to the one-dimensional (1D) confinement of electronic states [1, 26]. As a result of 1D confinement, the singularities in the electronic density of states (DOS), and correspondingly in the joint density of states (JDOS), are of great relevance for a variety of optical phenomena. When the energy of incident photons matches a singularity in JDOS of the valence and conduction bands, one expects to find resonant enhancement of the corresponding optical processes. From the unique 1D electronic structure, in addition to the strong electron-phonon coupling, one is able to obtain detailed information about vibrational properties of nanotubes using resonance Raman spectroscopy [10]. Lastly, in light of the recent advances in photoluminescence (PL) spectroscopy, the chapter present an extension of the theoretical framework that uses excitonic models to explain optical transitions observed in semiconducting SWNTs.

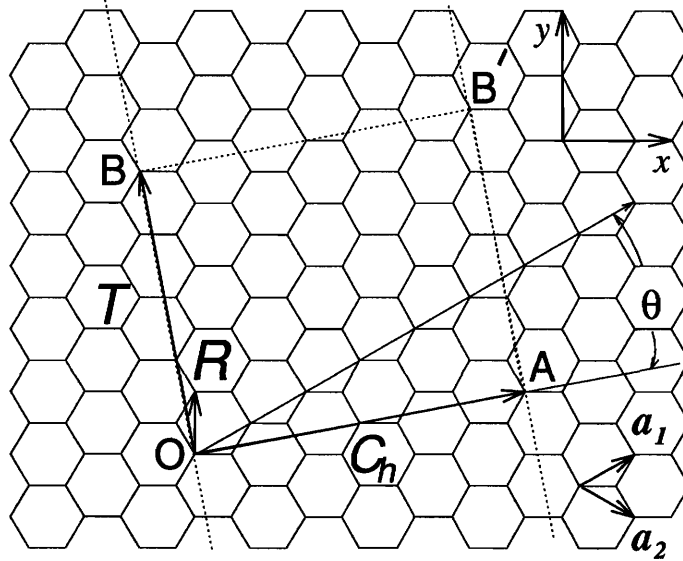


Figure 2-1: The unrolled honeycomb lattice of a nanotube. When we connect sites  $O$  and  $A$ , and sites  $B$  and  $B'$ , a nanotube can be constructed. The vectors  $OA$  and  $OB$  define the chiral vector  $\mathbf{C}_h$  and the translational vector  $\mathbf{T}$  of the nanotube, respectively. The rectangle  $OAB'B$  defines the unit cell for the nanotube. The figure is constructed for an  $(n, m) = (4, 2)$  nanotube [1].

## 2.1 Structure and Notation of SWNTs

In this section, an introduction is provided to the structural properties of SWNTs that emphasize the unique 1D attributes that set them apart from their bulk counterparts.

A single wall carbon nanotube (SWNT) can be conceptualized as a single graphene sheet, one atom thick, composed of a honeycomb arrangement of carbon atoms, that is rolled up into a seamless cylinder [27]. Figure 2-1 shows how a rectangular piece of graphene sheet defines the nanotube unit cell by the nanotube translational vector  $\mathbf{T}$  and the chiral vector  $\mathbf{C}_h$ . The detailed structure of a given SWNT can be specified by the chiral vector  $\mathbf{C}_h$

$$\mathbf{C}_h = n\mathbf{a}_1 + m\mathbf{a}_2 \equiv (n, m) \quad (2.1)$$

where unit vectors  $\mathbf{a}_1$  and  $\mathbf{a}_2$  are the unit vectors of the graphene lattice. As shown in Figure 2-1, the chiral vector  $\mathbf{C}_h$  makes a chiral angle  $\theta$  with the so-called zigzag (or  $\mathbf{a}_1$ ) edge. In addition,  $\mathbf{C}_h$  connects two crystallographically equivalent sites  $O$  and  $A$  on a two-dimensional (2D) graphene sheet where a carbon atom is located at each vertex of the honeycomb structure [28]. The axis of the zigzag nanotube corresponds to  $\theta = 0^\circ$ , while the so-called *armchair* nanotube axis corresponds to  $\theta = 30^\circ$ , and the nanotube axis for so-called *chiral* nanotubes corresponds to  $0 \leq \theta \leq 30^\circ$ . The seamless cylinder joint of the nanotube is made by joining the line  $AB'$  to the parallel line  $OB$  in Figure 2-1. For a given  $(n, m)$  SWNT, the nanotube diameter  $d_t$  can be determined as:

$$d_t = C_h/\pi = \sqrt{3}a_{C-C}(m^2 + mn + n^2)^{1/2}/\pi \quad (2.2)$$

where  $a_{C-C}$  is the nearest-neighbor C-C distance (1.421 Å in graphite),  $C_h$  is the length of the chiral vector  $\mathbf{C}_h$ . The chiral angle  $\theta$  is given by

$$\theta = \tan^{-1}[\sqrt{3}m/(m + 2n)]. \quad (2.3)$$

Thus, the geometric structure of a SWNT can be specified by its  $(n, m)$  indices, which can be used to calculate the values for  $d_t$  and  $\theta$ . The unit cell of the 1D nanotube  $OBB'A$  can be defined in terms of the unit cell of the 2D honeycomb lattice defined by the vectors  $\mathbf{a}_1$  and  $\mathbf{a}_2$ . Figure 2-2 shows the unit cell of a graphene lattice in (a) real space and (b) the Brillouin zone in reciprocal space of 2D graphite.

In Figure 2-2 (a), the real space basis vectors  $\mathbf{a}_1$  and  $\mathbf{a}_2$  of the hexagonal lattice are expressed as  $\mathbf{a}_1 = (\sqrt{3}a/2, a/2)$  and  $\mathbf{a}_2 = (\sqrt{3}a/2, a/2)$ , where  $a = |\mathbf{a}_1| = |\mathbf{a}_2| = 1.42 \times \sqrt{3} = 2.46 \text{ \AA}$  is the lattice constant of a graphene layer. Correspondingly, the basis vectors  $\mathbf{b}_1$  and  $\mathbf{b}_2$  of the reciprocal lattice are given by  $\mathbf{b}_1 = (2\pi/\sqrt{3}a, 2\pi/a)$  and  $\mathbf{b}_2 = (2\pi/\sqrt{3}a, -2\pi/a)$  corresponding to the graphene lattice constant of  $4\pi/\sqrt{3}a$  in reciprocal space. The high symmetry points,  $\Gamma$ ,  $K$ , and  $M$  point of the Brillouin zone are shown.

To define the unit cell for the 1D nanotube, the vector  $OB$  in Fig. 2-1 is defined as the shortest repeat distance along the nanotube axis, thereby defining the translation

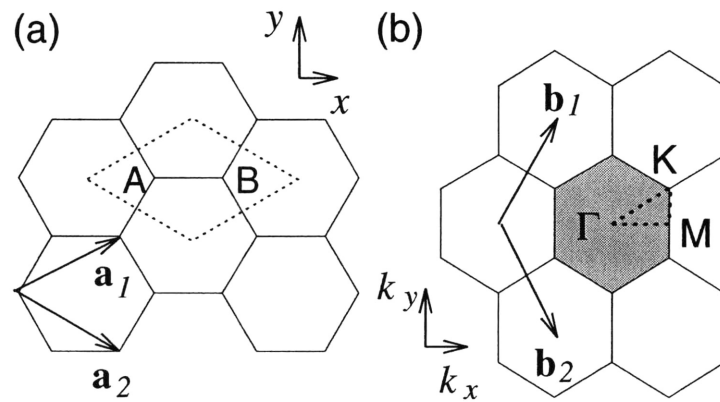


Figure 2-2: (a) The unit cell containing sites A and B where carbon atoms are located, and (b) the Brillouin zone of a graphene or two-dimensional graphite layer are shown as the dotted rhombus and the shaded hexagon, respectively. The vectors  $\mathbf{a}_i$ , and  $\mathbf{b}_i$ , ( $i = 1, 2$ ) are basis vectors and reciprocal lattice vectors, respectively. The high symmetry points,  $\Gamma$ ,  $K$  and  $M$  are indicated [2].

vector  $\mathbf{T}$

$$\mathbf{T} = t_1 \mathbf{a}_1 + t_2 \mathbf{a}_2 \equiv (t_1, t_2) \quad (2.4)$$

where the coefficients  $t_1$  and  $t_2$  are related to  $(n, m)$  by

$$\begin{aligned} t_1 &= (2m + n)/d_R \\ t_2 &= -(2n + m)/d_R \end{aligned} \quad (2.5)$$

where  $d_R$  is the greatest common divisor of  $(2n + m, 2m + n)$  and is given by

$$d_R = \begin{cases} d & \text{if } n - m \text{ is not a multiple of } 3d \\ 3d & \text{if } n - m \text{ is a multiple of } 3d, \end{cases} \quad (2.6)$$

in which  $d$  is the greatest common divisor of  $(n, m)$ . The magnitude of the translation vector  $T = |\mathbf{T}|$  is  $|\mathbf{T}| = \sqrt{3}L/d_R$  where  $L$  is the length of the chiral vector  $C_h = \pi d_t$  and  $d_t$  is the nanotube diameter. The unit cell of the nanotube is defined as the area delineated by the vectors  $\mathbf{T}$  and  $C_h$ .

Since the real space unit cell is much larger than that for a 2D graphene sheet, the 1D Brillouin zone (BZ) for the nanotube is much smaller than the BZ for a single 2-atom graphene 2D unit cell. Because the local crystal structure of the nanotube is so close to that of a graphene sheet, and because the Brillouin zone is small, the zone-folding techniques have been commonly used to obtain approximate electron and phonon dispersion relations for carbon nanotubes.

Whereas the lattice vector  $\mathbf{T}$ , given by Eq.2.4, and the chiral vector  $C_h$ , given by Eq.2.1, both determine the unit cell of the carbon nanotube in real space, the corresponding vectors in reciprocal space are the reciprocal lattice vectors  $\mathbf{K}_2$  along the nanotube axis and  $\mathbf{K}_1$  in the circumferential direction, which gives the discrete  $k$  values in the direction of the chiral vector  $C_h$ . The vectors  $\mathbf{K}_1$  and  $\mathbf{K}_2$  are obtained from the relation  $\mathbf{R}_i \cdot \mathbf{K}_j = 2\pi\delta_{ij}$ , where  $\mathbf{R}_i$  and  $\mathbf{K}_j$  are, respectively, the lattice vectors in real and reciprocal space, and  $\mathbf{K}_1$  and  $\mathbf{K}_2$  therefore satisfy the relations

$$\begin{aligned} \mathbf{C}_h \cdot \mathbf{K}_1 &= 2\pi, & \mathbf{T} \cdot \mathbf{K}_1 &= 0, \\ \mathbf{C}_h \cdot \mathbf{K}_2 &= 0, & \mathbf{T} \cdot \mathbf{K}_2 &= 2\pi. \end{aligned} \quad (2.7)$$

From Eqs. (2.7) it follows that  $\mathbf{K}_1$  and  $\mathbf{K}_2$  can be written as:

$$\mathbf{K}_1 = \frac{1}{N}(-t_2\mathbf{b}_1 + t_1\mathbf{b}_2), \quad \mathbf{K}_2 = \frac{1}{N}(m\mathbf{b}_1 - n\mathbf{b}_2), \quad (2.8)$$

where  $\mathbf{b}_1$  and  $\mathbf{b}_2$  are the reciprocal lattice vectors of a 2D graphene sheet given above (See Figure 2-2 (b)). The  $N$  wave vectors  $\mu\mathbf{K}_1$  ( $\mu = 0, \dots, N - 1$ ) give rise to  $N$  discrete  $k$  vectors in the circumferential direction. For each of the  $\mu$  discrete values of the circumferential wave vectors, a 1D electronic energy von Hove Singularity appears. Because of the translational symmetry of  $\mathbf{T}$ , the wave vectors in the direction of  $\mathbf{K}_2$  are quasi-continuous for a carbon nanotube of near-infinite length.

### 2.1.1 Electronic Structure

In the simplest model, the electronic structure of a SWNT can be obtained from its parent material graphite, with additional confinement constraints to account for the highly confined 1D geometry. While the in-plane  $\sigma$  bands form a strong covalent bonding network within the 2D graphene layer, the non-hybridized  $\pi$  bands are close to the Fermi level, so that electrons can be optically excited from the valence ( $\pi$ ) to the conduction ( $\pi^*$ ) band. Using the simple tight binding calculation, one can obtain dispersion for the  $\pi$  and  $\pi^*$  bands of 2D graphite as shown in Fig. 2-3(a) [1]. The optical transitions occur close to high symmetry  $K$  points, where the valence and conduction bands touch each other in graphite.

Due to the periodic boundary condition, the wave vectors along the circumferential direction become quantized, in which  $k_{\perp} = \ell K_1$ , where  $K_1 = 2/d_t$  and  $\ell = \text{integer}$ . The wave vectors  $k_{\parallel}$  along the tube axis direction  $K_2$  remain continuous ( $k_{\parallel} = \alpha K_2$ ,  $\alpha$  real,  $|\alpha| < 1/2$ ). The  $K_1$  and  $K_2$  are the basis vectors for the nanotube Brillouin zone. As a result, the allowed wave vectors in the carbon nanotube reciprocal space can be represented in the 2D graphene sheet Brillouin zone by cutting lines of allowed wave vectors, as shown in Fig. 2-3(a) [3]. The electronic structure of the nanotube can then be obtained by superimposing the 1D cutting lines on the 2D electronic constant energy surfaces, as shown in Fig. 2-3(b). For simplicity, Figs. 2-3(a) and (b) shows the the SWNT electronic structures for a (4, 2) SWNT obtained from the cutting

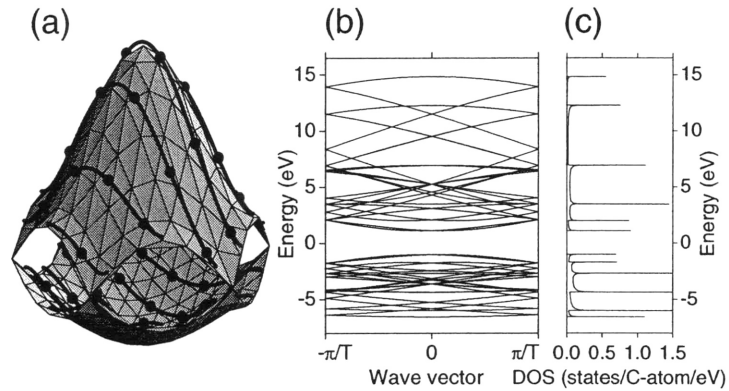


Figure 2-3: (a) The calculated constant energy contours for the conduction and valence bands of a graphene layer in the first Brillouin zone using the  $\pi$ -band nearest-neighbor tight-binding model [1]. Solid curves show the cutting lines for the (4,2) nanotube [3]. (b) Electronic energy band diagram,  $E(k)$  for the (4,2) nanotube obtained by zone-folding from (a). (c) Density of electronic states for the band diagram shown in (b).



line and zone folding approach [1, 3]. In reality, the large curvature in such a small diameter SWNT introduces re-hybridization of the  $sp^2$  bonding network, as well as a mixing of the  $\sigma$  and  $\pi$  bonds. More accurate methods will be required to describe the electronic structure of small diameter SWNTs.

Although the 1D electronic band structure of this small diameter tube, appears to be complex, the optical absorption or emission rate in nanotubes is related primarily to the electronic states at the vHSs, as shown in Fig. 2-3(c), thereby greatly simplifying the analysis of the optical experiments. These arguments also apply to the case of excitonic transitions discussed below.

In theory, the distance between two neighboring cutting lines in Fig. 2-3(a) is inversely proportional to the nanotube diameter ( $K_1 = 2/d_t$ ), and their direction relative to the hexagonal 2D Brillouin zone depends on  $\theta$ . It is, therefore, easy to imagine that each  $(n, m)$  SWNT exhibits a different set of vHSs in its valence and conduction bands, and a different set of electronic transition energies between its valence and conduction band vHSs. For this reason, optics experiments can be used for structural characterization of a given  $(n, m)$  carbon nanotube. By calling  $E_{ii}$  the electronic transition energies between electronic valence and conduction bands with the same index, with the subscript  $i = 1, 2, 3, \dots$  labeling the  $E_{ii}$  values for a given SWNT as their energy magnitude increases [1], the set of measured  $E_{ii}$  values will be specific to each individual  $(n, m)$  nanotube.

SWNTs can be classified according to whether  $\text{mod}(2n + m, 3) = 0, 1$  or  $2$ , where the integers  $0, 1, 2$  denote the remainders when  $(2n + m)$  is divided by 3. Here mod 1 and mod 2 SWNTs are semiconducting, while mod 0 SWNTs ( $n < m$ ) are metallic at room temperature. Frequently, superscripts  $S$  or  $M$  are used to denote the electronic transition energies  $E_{ii}^M$  for metallic SWNTs and  $E_{ii}^S$  for semiconducting SWNTs.

### 2.1.2 Phonon Structure

Phonons denote the quantized normal mode vibrations, and these crystal vibrations strongly influence many physical processes in condensed matter systems. The phonon dispersion relations in a SWNTs can be obtained from those of an isolated

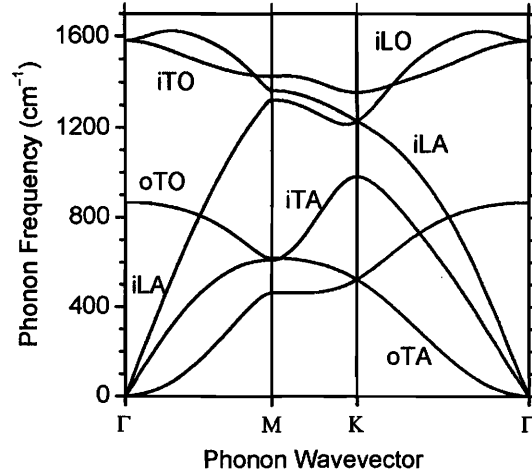


Figure 2-4: Phonon dispersion relation of graphite, calculated using the force constants determined by fitting of the experimental points obtained from electron energy loss spectroscopy, inelastic neutron scattering, velocity of sound, and X-ray diffraction techniques [4–6]

2D graphene sheet by using the similar zone folding approach [5, 29, 30] as was used to find the 1D electronic dispersion relations [1, 31]. In an ordinary graphene lattice, two atoms  $A$  and  $B$  in the unit cell of the graphene layer (see Fig. 2-1) give rise to six phonon modes, because of the three degrees of freedom per atom. By superimposing the  $N$  cutting lines in the  $\vec{K}_1$ -extended representation on the six phonon frequency surfaces in the reciprocal space of the graphene layer, according to the zone-folding scheme as described previously,  $6N$  phonon modes can be obtained for each carbon nanotube. The  $6(N/2 - 1)$  pairs of the phonon modes arising from the cutting lines of the indices  $\mu$  and  $-\mu$ , where  $\mu = 1, \dots, (N/2 - 1)$ , are expected to be doubly degenerate, similarly to the case of the electronic subbands discussed previously, whereas the 12 phonon modes arising from the cutting lines of the indices  $\mu = 0$  and  $\mu = N/2$  are non-degenerate, so that the total number of distinct phonon branches is  $3(N + 2)$ . The calculated phonon dispersion curves of Fig. 2-4 were calculated using force constants determined by fitting of the experimental points obtained from electron energy loss spectroscopy, inelastic neutron scattering, velocity of sound, and X-ray diffraction

techniques [4–6].

The strong 1D characteristics of nanotubes also give rise to sharp features in the phonon density of states for SWNTs from those of the 2D graphene sheet [1], as is illustrated, respectively, in Fig. 2-5(a) and (b) for a (10,10) SWNT. The large amount of sharp structure in the phonon density of states in Fig. 2-5(b) for the (10,10) SWNT reflects the many phonon branches and the 1D nature of SWNTs relative to 2D graphite. The phonon density of states for 2D graphite shown in Figure 2-5(c) is obtained by summing the 1D phonon density of states for many SWNTs [1, 7]. In addition to the longitudinal acoustic (LA) and transverse acoustic (TA) modes, some important modes for coupling electrons to the lattice are the low-lying optical modes at the center of the Brillouin zone  $q = 0$ . These modes include one with  $E_2$  symmetry expected at  $\sim 17 \text{ cm}^{-1}$  (the squash mode), one with  $E_1$  symmetry, expected at  $\sim 118 \text{ cm}^{-1}$ , and one with  $A$  symmetry (radial breathing mode) [1, 11]. Figure 2-7 shows the Raman-active modes of  $A$ ,  $E_1$ , and  $E_2$  symmetries and the corresponding cutting lines  $\mu = 0$ ,  $\mu = \pm 1$ , and  $\mu = \pm 2$  in the unfolded 2D Brillouin zone. The  $\Gamma$  points of the cutting lines are shown by solid dots. Of these three low energy phonon modes, it is only the radial breathing mode (RBM), where all the carbon atoms are vibrating in phase in the radial direction, that has been studied experimentally. The mode is unique to SWNTs and does not occur in other carbon systems, and the presence of the feature has been of great importance in identifying the presence of nanotubes in a given sample and in the characterization of nanotube-containing materials, as discussed in Sec. 2.3.

## 2.2 Resonance Raman Scattering Processes

A Raman scattering event usually consists of either (1) photon absorption to excite an exciton (an electron-hole bound state created by the photon), (2) phonon emission from an exciton, and (3) finally photon emission by the exciton. The scattered light is measured as a Raman spectrum. In light scattering, the photon absorption process generally occurs even though the energy separation between the ground and the

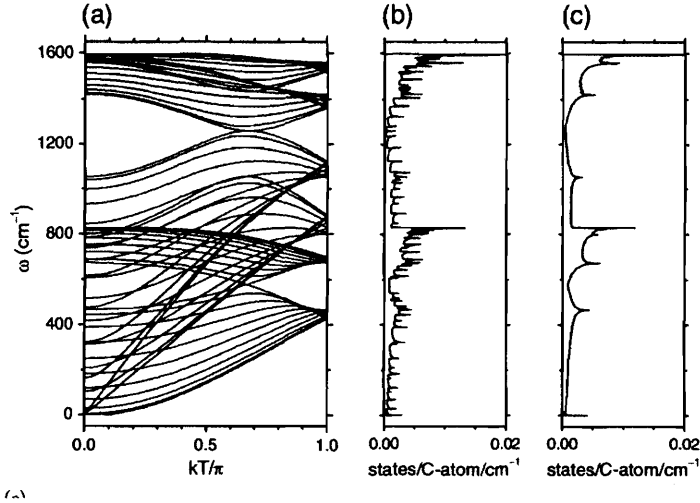


Figure 2-5: (a) The calculated phonon dispersion relations of an armchair carbon nanotube with  $(n, m) = (10, 10)$ . The number of degrees of freedom is 120 and the number of distinct phonon branches is only 66 because of the degeneracy of these modes due to symmetry arguments [1]. (b) The corresponding phonon density of states for a (10,10) nanotube [7]. (c) The corresponding phonon density of states for a 2D graphene sheet [1].

excited states is not equal to the energy of the photon, in which case we call the transition a *virtual* or *non-resonant* transition.

On the other hand, when the vibrational frequency is close to an eigen frequency of the system, the vibrational amplitude becomes singularly large. This enhancement in intensity is identified with the resonance phenomenon. Similar resonance effects occur in Raman scattering process, where the scattered amplitude becomes very large when  $E_{\text{laser}}$  is close to the transition energy for light absorption or emission ( $E_{ii}$ ). If the resonance Raman effect occurs for photon absorption, that is the incident light resonance condition,

$$E_{\text{laser}} = E_{ii} \quad (\text{incident light resonance}), \quad (2.9)$$

all Raman features will be resonantly enhanced. For the scattered light resonance condition, a phonon with frequency  $\omega_i$  is created,

$$E_{\text{laser}} = E_{ii} + \hbar\omega_i \quad (\text{Stokes scattered light resonance}), \quad (2.10)$$

and the resonance condition depends on the phonon energy  $\hbar\omega_i$ .

Inelastic scattering of light can also occur in phonon absorption events (anti-Stokes Raman scattering). In order to absorb a phonon, the phonon should be present in the Bose-Einstein distribution at thermal equilibrium. The resonance condition for the anti-Stokes Raman spectra for the incident light resonance condition is the same as that of the Stokes spectra, whereas the scattered light resonance condition of the anti-Stokes spectra is given by

$$E_{\text{laser}} = E_{ii} - \hbar\omega_i \quad (\text{anti - Stokes scattered light resonance}), \quad (2.11)$$

Thus, by comparing the Stokes with the anti-Stokes spectra, we can determine whether the resonance condition is for incident resonance or scattered resonance. The number of emitted phonons before relaxation of the lattice can be one or more, and the order of a scattering event is defined as its number in the sequence of all the scattering events, including both phonon inelastic scattering and elastic scattering by a defect of the crystal. The lowest order process is the first-order Raman scattering process which gives Raman spectra involving one-phonon emission, such as the RBM or the *G*-band feature shown in Fig. 2-6(a) for SWNTs.

## 2.3 Resonance Raman Spectroscopy of SWNTs

### 2.3.1 First order Raman Spectra

As described earlier, resonance Raman spectroscopy has proven to be a very effective tool in the study of not only the vibrational properties of the carbon nanotubes, but also the 1D electronic DOS through the resonant Raman effect, which increases the Raman signal by over six orders of magnitudes. Due to the very sharp van Hove singularities in the 1D DOS, optical absorption cross section becomes very high under resonant conditions. In this thesis, a sample of SWNTs produced using Co and Mo catalysts with a narrow Gaussian diameter distributions is studied in detail, and we have been able to probe the predicted 1D behaviors in the resonance

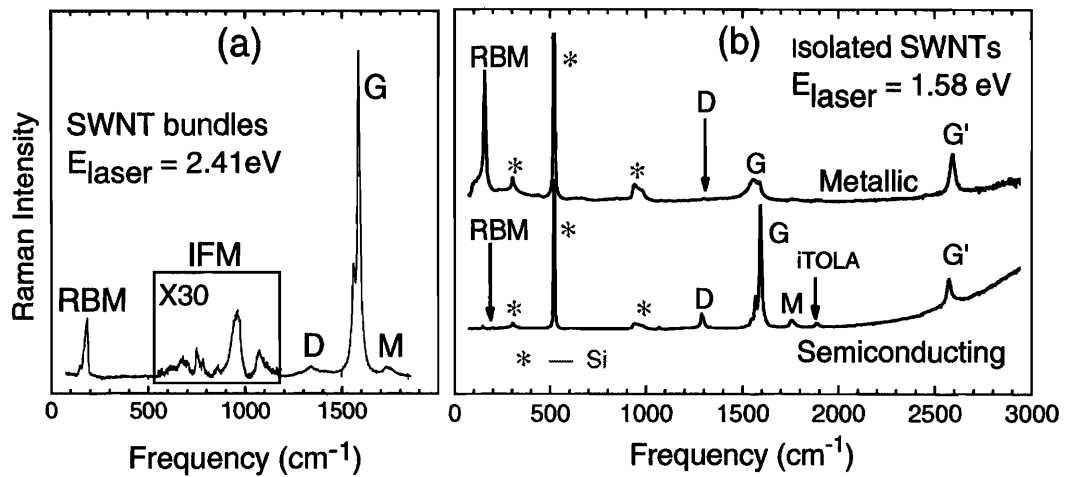


Figure 2-6: (a) Raman spectra from HiPco SWNT bundles (see text) [8]. (b) Raman spectra from a metallic (top) and a semiconducting (bottom) SWNT at the single nanotube level. The spectra show the radial breathing modes (RBM),  $D$ -band,  $G$ -band and  $G'$  band features, in addition to weak double resonance features associated with the  $M$ -band and the  $i$ TOLA second-order modes [9]. The isolated carbon nanotubes are sitting on an oxidized silicon substrate which provides contributions to the Raman spectra denoted by “\*”, and these Si features are used for calibration purposes [10].

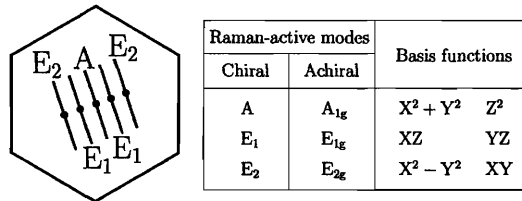


Figure 2-7: The Raman-active modes of A,  $E_1$ , and  $E_2$  symmetries and the corresponding cutting lines  $\mu = 0$ ,  $\mu = \pm 1$ , and  $\mu = \pm 2$  in the unfolded 2D Brillouin zone. The  $\Gamma$  points of the cutting lines are shown by solid dots. The table gives irreducible representations and basis functions for the Raman-active modes according to group theory. The Z axis is parallel and the XY plane is perpendicular to the nanotube axis. [1, 11]

Raman spectra. The first-order Raman spectra of SWNTs are dominated by three features. The RBM feature is located at a range with very low frequency shifts ( $200\text{ cm}^{-1}$ ) and involves a radially symmetric vibration of the carbon atoms about the axis of the nanotubes. This feature yields structural information about the nanotubes, since the RBM frequency is inversely proportional to the nanotube diameter. In the intermediate frequency region is a feature of low intensity located at approximately  $1300\text{ cm}^{-1}$  (D-band), which has a completely different and highly dispersive resonant behavior, i.e., it shifts to higher frequencies as the laser excitation energy is increased. This feature is associated with a 2D resonant behavior of the carbon nanotubes. The high frequency tangential mode (G-band) region involves motion of the carbon along the nanotube axis, about the circumference, and all tangential directions in between. However, the modes along the axis and along the circumference are the directions most commonly used for characterization purposes. Study of this mode has yielded a lot of information about the electronic density of states and the nature of the electron-phonon coupling.

### Radial Breathing Modes

Since the RBM is a nanotube-specific feature that does not appear in other carbon materials, the presence of the RBM has become an important signature to identify the presence of SWNTs in carbon materials. The RBM frequency  $\omega_{\text{RBM}}$  gives the nanotube diameter through the relation  $\omega_{\text{RBM}} = \alpha/d_t + \beta$ , where  $\alpha = 248\text{ cm}^{-1}\text{nm}$  and  $\beta = 0$  has been found to apply to isolated SWNTs on a Si/SiO<sub>2</sub> substrate [7, 10, 32]. In the case of nanotube bundles or bulk samples dispersed in solution using wrapping agents,  $\beta$  accounts for the intertube interactions and environmental effects. The values of unique  $\alpha$  and  $\beta$  combinations have been determined empirically for different samples prepared using different methods. Considering the  $d_t$  values obtained from the  $\omega_{\text{RBM}}$ , and  $E_{ii} \sim E_{\text{laser}}$  from the resonance condition, the RBM feature can be used for making  $(n, m)$  assignments of individual SWNTs [10]. Figure. 2-6(b) shows the spectra for isolated nanotubes grown on a SiO<sub>2</sub> substrate. The spectra were taken with a laser excitation of  $E_{\text{laser}} = 1.58\text{ eV}$  (785 nm). The observed RBM and G-band

spectral features for the upper spectrum are related to a SWNT with  $d_t = 1.59$  nm.  $E_{\text{laser}}$  is now in resonance with  $E_{11}^M$ , and can be assigned as a metallic (13, 10) SWNT. The lower spectra comes from a semiconducting (23, 1) SWNT, where  $E_{\text{laser}}$  is in resonance with  $E_{33}^S$ .

### Tangential G-band feature

The SWNT  $G$  band is composed of six components due to the phonon wave vector confinement along the SWNT circumferential direction, but most of these peaks have small intensity. Most  $G$ -band spectra for SWNTs shows two dominant features, one peaked at  $1593\text{ cm}^{-1}$  ( $G^+$ ) and the other peaked at  $1567\text{ cm}^{-1}$  ( $G^-$ ) (for nanotubes of diameter  $\sim 1.4$  nm). The  $G^+$  feature is associated with carbon atom vibrations along the nanotube axis and its frequency  $\omega_{G^+}$  is sensitive to charge transfer from dopant additions to SWNTs. The  $G^-$  feature, in contrast, is associated with vibrations of carbon atoms along the circumferential direction of the nanotube, and its line-shape and peak frequency is highly sensitive to whether the SWNT is metallic (Breit–Wigner–Fano line-shape) or semiconducting (Lorentzian line-shape) [33, 34]. While the most intense peaks at  $1593\text{ cm}^{-1}$  and  $1567\text{ cm}^{-1}$  arise from phonons with  $A$  and  $E_1$  symmetries, the smaller intensity features at  $1526\text{ cm}^{-1}$  and  $1606\text{ cm}^{-1}$  are associated with  $E_2$  symmetry phonons. Phonons with  $A$ ,  $E_1$  and  $E_2$  symmetries can be distinguished from one another by their behavior in polarization-sensitive Raman experiments [12, 35]. These are the only phonon symmetries giving rise to Raman active modes [3].

Polarization analysis of Raman spectra and a comparison with *ab initio* calculations is consistent with the observation of  $A$ ,  $E_1$  and  $E_2$  symmetry modes in the  $G$ -band for SWNTs. Figure 2-8(a) shows three different  $G$ -band Raman spectra from a semiconducting SWNT, but with different directions for the incident light polarization, i.e.  $\theta'_S$ ,  $\theta'_S + 40^\circ$  and  $\theta'_S + 80^\circ$ . Well-defined peaks associated with the  $G$ -band features are clearly observed, with different relative intensities for the different polarization geometries, and they are assigned as follows:  $1565$  and  $1591\text{ cm}^{-1} \rightarrow A$ ;  $1572$  and  $1593\text{ cm}^{-1} \rightarrow E_1$ ;  $1554$  and  $1601\text{ cm}^{-1} \rightarrow E_2$ . The SWNT giving rise to the



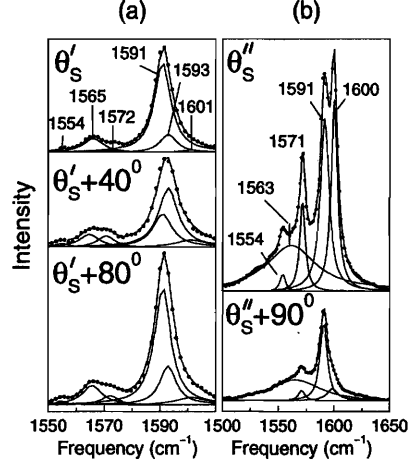


Figure 2-8: Polarization scattering geometry dependence for the  $G$ -band from two (a) and (b) isolated SWNTs in resonance with  $E_{\text{laser}} = 2.41$  eV. The Lorentzian peak frequencies are in  $\text{cm}^{-1}$ .  $\theta'_S$  and  $\theta''_S$  are the initial angles between the light polarization and the SWNT axis directions, not known a priori. From the relative intensities, and the polarization behavior of the  $G$ -band modes, we assign  $\theta'_S \sim 0^\circ$  and  $\theta''_S \sim 90^\circ$  [12].

$G$ -band spectra exhibits  $\omega_{\text{RBM}} = 180 \text{ cm}^{-1}$  ( $d_t = 1.38 \text{ nm}$ ) [10].

Figure 2-8(b) shows two  $G$ -band Raman spectra obtained from another semiconducting SWNT ( $\omega_{\text{RBM}} = 132 \text{ cm}^{-1}$ ), with  $\theta''_S$  and  $\theta''_S + 90^\circ$ . The spectra can be fit using four sharp Lorentzians, and a broad feature at about  $1563 \text{ cm}^{-1}$ . This broad feature (FWHM  $\sim 50 \text{ cm}^{-1}$ ) is sometimes observed in weakly resonant  $G$ -band spectra from semiconducting SWNTs. A broad feature is also observed at  $\sim 1610 \text{ cm}^{-1}$  for spectra from other SWNTs. Both broad features may be associated with a double resonance process [36]. From previous polarization Raman studies [35], the sharp peaks at  $1554$  and  $1600 \text{ cm}^{-1}$  are assigned as  $E_2$  modes, while the  $1571$  and  $1591 \text{ cm}^{-1}$  peaks are assigned as unresolved ( $A + E_1$ ) modes, their relative intensities depending on the incident light polarization direction [35].

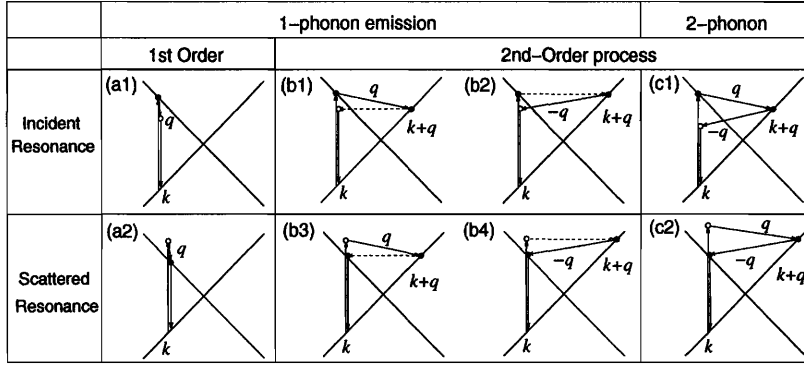


Figure 2-9: (a) First-order and (b) one-phonon second-order, (c) two-phonon second-order, resonance Raman spectral processes: (top) incident photon resonance and (bottom) scattered photon resonance conditions. For one-phonon, second-order transitions, one of the two scattering events is an elastic scattering event (dashed lines). Resonance points are shown as solid circles[13]. See text for details.

### 2.3.2 Overtones and Second Order Features

#### Double Resonance Scattering Processes

Figure 2-9 shows the schematic diagram of one and two phonon scattering processes occurring in most Raman scattering events for SWNTs. In second-order Raman scattering events, as shown in Fig. 2-9(b) and (c), the  $\mathbf{q}$  and  $-\mathbf{q}$  scattering wavevectors are involved, so that an electron can return to its original  $\mathbf{k}$  position after scattering. Second-order Raman scattering consists of either (b) one-phonon and one-elastic scattering event, or (c) two-phonon scattering events. In the case of two-phonon scattering events, we can have involvement of either the same phonon modes (overtone mode) or different phonon modes (combination modes).

In second-order double resonance (DR) processes for carbon materials [see Fig. 2-9(b) and (c)], the electron (1) absorbs a photon at a  $\mathbf{k}$  state, (2) scatters to  $\mathbf{k} + \mathbf{q}$  states, (3) scatters back to a  $\mathbf{k}$  state, and (4) emits a photon by recombining with a hole at a  $\mathbf{k}$  state. The two scattering processes consist of either elastic scattering by the defects of the crystal or inelastic scattering by emitting a phonon, as shown in Fig. 2-9. Thus (1) one-elastic and one-inelastic scattering event [Fig. 2-9(b)] and (2) two-inelastic scattering events [Fig. 2-9(c)] are relevant to 2nd order Raman spec-

troscopy. In a DR Raman process, two resonance conditions for three intermediate states should be satisfied, in which the intermediate  $\mathbf{k} + \mathbf{q}$  state is always a real electronic state (solid circles in Fig. 2-9) and either the initial or the final  $\mathbf{k}$  states is a real electronic state. The Raman intensity of a double resonance process is, in principle, comparable to that of a first order process obeying a single resonance condition. In order to satisfy energy-momentum conservation in one-phonon DR Raman spectroscopy [see Figs. 2-9 (b1) and (b2)], the inelastic scattering process gives a shorter phonon  $\mathbf{q}$  vector from the initial  $\mathbf{k}$  state than the elastic scattering process.

The electronic structure of 2D graphite near the Fermi energy  $E_F$  is linear in wave vector  $k$ , which is expressed by the crossed solid lines in Fig. 2-9. The crossing point corresponds to  $E_F$  located at the  $K$  point. When the laser energy  $E_{\text{laser}}$  increases, the resonance  $k$  vector for the electron moves away from the  $K$  point. In the DR process, the corresponding  $q$  vector for the phonon increases with increasing  $k$ , measured from the  $K$  point. Thus by changing  $E_{\text{laser}}$ , we can observe the phonon energy  $\hbar\omega(q)$  along the phonon dispersion relations (Fig. 2-10). This effect is observed experimentally as a dispersion of the phonon energy as a function of  $E_{\text{laser}}$  [37]. A tunable laser system can directly show this dispersive behavior for a dispersive feature such as the  $D$ -band or the  $G'$ -band in the Raman spectrum.

When we consider the energy and momentum conservation for  $k$  and  $q$ , we need to introduce two other concepts to describe the scattering processes: intravalley and intervalley scattering, respectively, associated with  $q = 0$  and  $q = 2k$  phonons where the value of  $k$  is measured from the  $K$  (or  $K'$ ) point [14, 38]. Since  $E_F$  is located at two inequivalent  $K$  and  $K'$  points in the 2D Brillouin zone, we can consider the scattering not only in the vicinity of the  $K$  (or  $K'$ ) points, as shown in Fig. 2-9, but also in scattering from  $K$  to  $K'$  (or from  $K'$  to  $K$ ). The corresponding  $q$  vector for intravalley and intervalley scattering is, respectively, near the  $\Gamma$  and  $K$  points, as measured from the  $\Gamma$  point. Only  $q = 2k$  modes will show a large dispersive behavior for the Raman frequency as a function of  $E_{\text{laser}}$ .

Both in graphite and in SWNTs, the  $D$ -band at  $1350\text{ cm}^{-1}$  and the  $G'$ -band at  $2700\text{ cm}^{-1}$  (for  $E_{\text{laser}} = 2.41\text{ eV}$ ) are, respectively, due to one-phonon and two-phonon,

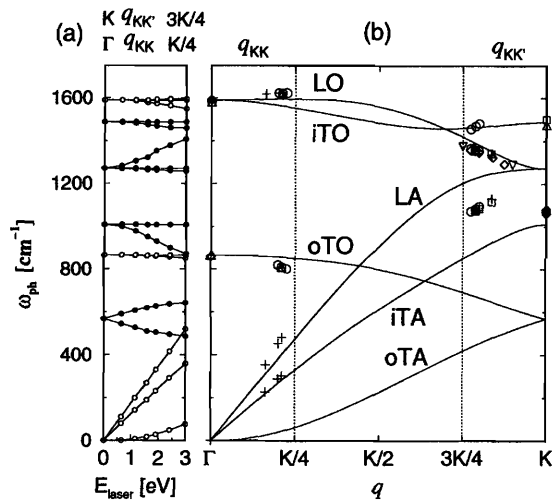


Figure 2-10: (a) Calculated Raman frequencies for the double resonance condition as a function of  $E_{laser}$  (bottom axis) and the  $q$  vector along  $\Gamma$ -K (top axis). Solid and open circles correspond to phonon modes near the  $K$  and  $\Gamma$  points, respectively. (b) The 6 graphite phonon dispersion curves (lines) and experimental Raman observations (symbols) are placed according to double resonance theory [14].

2nd order Raman intervalley scattering processes. Thus for graphite, the  $D$ -band spectra appearing at  $1350\text{ cm}^{-1}$  (one-phonon DR) can be fitted to two Lorentzians, while the  $G'$ -band feature at  $2700\text{ cm}^{-1}$  (two-phonon DR) can be fitted to one Lorentzian [38]. The disorder-induced  $D$  band is observed in disordered graphite-like materials, including carbon nanotubes, while its second-order harmonic, the  $G'$  band is observed even in the absence of defects. Typically  $\omega_D$  and  $\omega_{G'}$  would be measured for  $E_{\text{laser}} = 2.41\text{ eV}$  and their dispersion would be  $53\text{ cm}^{-1}/\text{eV}$  and  $106\text{ cm}^{-1}/\text{eV}$ , respectively, for SWNTs. Although the  $\omega_D$  and  $\omega_{G'}$  dependences on  $E_{\text{laser}}$  are linear for most disordered graphite-like materials,  $\omega_D$  and  $\omega_{G'}$  in SWNTs exhibit an anomalous oscillatory dispersive effect, since the resonance condition for SWNTs occur at their 1D vHSs [39–41]. Many weak features in the Raman spectra for SWNTs can be assigned to one-phonon or two-phonon, 2nd order double resonance processes, and these are listed in Table 2.1 together with their frequencies and dispersion  $d\omega/dE_{\text{laser}}^3$ . Also of importance is the variation of their mode frequencies with tube diameter  $d_t$  [42].

### $D$ and $G'$ bands

Also commonly found in the resonance Raman spectra in SWNT is the  $D$ -band feature with  $\omega_D$  at  $1200\text{--}1347\text{ cm}^{-1}$  in Fig. 2-6(a) and (b), stemming from the disorder-induced mode in graphite, and its second harmonic, the  $G'$  band (not shown) occurring at  $\sim 2\omega_D$ , both associated with a double resonance process [43]. Both the  $D$ -band and the  $G'$ -band are sensitive to the nanotube diameter and chirality, and therefore have been very important in revealing much new physics about carbon nanotubes from single nanotube studies, as discussed below.

Single nanotube measurements of the  $D$ -band and  $G'$ -band features show these features to be connected to a double resonance process [44], with special properties associated with the van Hove singularities of the SWNTs [45–48]. Measurements of the  $D$ -band and the  $G'$ -band frequencies at the single nanotube level provide unique information on the chirality and diameter dependence of  $\omega_D$  and  $\omega_{G'}$ , and can be used to measure the trigonal warping effect in the electron and phonon dispersion

Table 2.1: Properties of the various Raman features in graphite and SWNTs.<sup>1)</sup>

Name	$\omega[\text{cm}^{-1}]$	Res. <sup>2)</sup>	$d\omega/dE$ <sup>3)</sup>	Notes
iTA	288	DR1-AV	129	iTA mode, $q = 2k$
LA	453	DR1-AV	216	LA mode, $q = 2k$
RBM	$248/d_t$	SR	0	Nanotube only, vibration of radius
oTO	860	DR1-AV	0	IR-active mode in graphite
D	1350	DR1-EV	53	LO or iTO mode, $q = 2k$
LO	1450	DR1-EV	0	LO mode, $q = 0$
$G$	1582	SR	0	Raman active mode of graphite
$M^-$	1732	DR2-AV	-26	overtone of oTO mode, $q = 2k$
$M^+$	1755	DR2-AV	0	overtone of oTO mode, $q = 0$
iTOLA	1950	DR2-AV	230	combinational mode of iTO and LA
$G'$	2700	DR2-EV	106	overtone of D mode
2LO	2900	DR2-AV	0	overtone of LO mode
2G	3180	DR2-AV	0	overtone of $G$ mode

<sup>1)</sup> Dispersive mode frequencies  $\omega$  are given at  $E_{\text{laser}} = 2.41$  eV.

<sup>2)</sup> The notation used here to classify resonance (Res.) Raman scattering processes is:

SR: 1st order, single resonance; DR1: 1 phonon, double resonance; DR2: 2 phonon, double resonance. AV: intravalley scattering; EV: intervalley scattering;

<sup>3)</sup>  $d\omega/dE$  denotes the change  $\omega$  in  $\text{cm}^{-1}$  produced by changing  $E = E_{\text{laser}}$  by 1 eV.

relations of SWNTs, providing information not readily available using other experimental techniques [49].

Measurements of  $\omega_D$  and  $\omega_{G'}$  for special semiconducting SWNTs, where the *incident* photon is in resonance with one vHS (e.g.,  $E_{44}^S$ ) and the *scattered* photon is in resonance with another vHS (e.g.,  $E_{33}^S$ ) is a special Raman effect that can be observed for very special SWNTs. These observations, are particularly useful for corroborating specific  $(n, m)$  assignments made by the RBM mode, as well as for corroborating the  $(n, m)$  assignment procedure itself [49]. The corresponding measurements for metallic SWNTs provide definitive information about the magnitude of the trigonal warping effect in the electronic structure of SWNTs because of the strong coupling of electrons and phonons under strong coupling conditions [47].

### Other Double resonance features

To help with the identification of the origin of the many Raman features, analysis of the dependence of the spectra on  $E_{\text{laser}}$  is usually carried out to determine the dispersion of these spectral features as  $E_{\text{laser}}$  is varied. Such information can be seen from the spectra in Ref. [50] on SWNT bundles. Figure 2-11 shows that the  $M$  feature near  $1750 \text{ cm}^{-1}$  can be analyzed in terms of two components with frequencies  $\omega_M^-$  and  $\omega_M^+$ . A Lorentzian fit was therefore made of the several Raman features observed from  $1650$  to  $2100 \text{ cm}^{-1}$  from SWNT bundles, using different  $E_{\text{laser}}$  excitation lines. This figure shows that the lower frequency mode  $\omega_M^-$  exhibits a weakly dispersive behavior (frequency  $\omega_M^-$  shifting down by  $\sim 30 \text{ cm}^{-1}$  as  $E_{\text{laser}}$  is varied from  $1.58 \text{ eV}$  to  $2.71 \text{ eV}$ ), while the upper feature frequency  $\omega_M^+$  is basically independent of  $E_{\text{laser}}$ . [51] The higher frequency iTOLA mode is highly dispersive and upshifts from  $1864 \text{ cm}^{-1}$  to  $2000 \text{ cm}^{-1}$  as  $E_{\text{laser}}$  varies from  $1.58 \text{ eV}$  to  $2.71 \text{ eV}$ .

The features observed between  $1650$  and  $2100 \text{ cm}^{-1}$  are, therefore, assigned as overtones and combination modes related to graphite, as predicted by double resonance theory [14]. More specifically, the two features near  $1750 \text{ cm}^{-1}$  ( $M$  band) are attributed to overtones of the out-of-plane (oTO), infrared-active mode at  $867 \text{ cm}^{-1}$  in graphite, with  $M^+$  identified with an intravally overtone of oTO phonon and  $M^-$

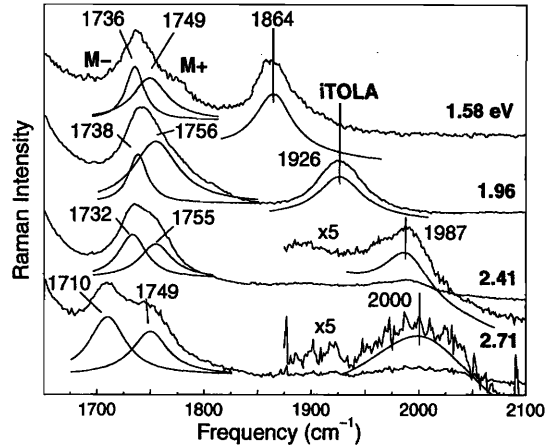


Figure 2-11: Lorentzian fits of the Raman spectra taken at several  $E_{\text{laser}}$  values for the  $M$  feature near  $1750 \text{ cm}^{-1}$  and the highly dispersive iTOLA feature observed at  $1950 \text{ cm}^{-1}$  in SWNT bundles [9]. Peak frequencies ( $\text{cm}^{-1}$ ) and  $E_{\text{laser}}$  values (eV) are displayed.

with an intervalley overtone (see Table 2.1). The feature at  $\sim 1950 \text{ cm}^{-1}$  (iTOLA band) is attributed to a combination of one phonon from the in-plane transverse optical branch (iTTO) plus one phonon from the longitudinal acoustic (LA) branch, iTTO+LA.

Resonance Raman spectroscopy with an energy tunable system is also used to analyze Raman features appearing in the spectral region between  $600\text{--}1100 \text{ cm}^{-1}$ , in single-wall carbon nanotubes. Figure 2-12(a) plots the  $E_{\text{laser}}$  dependence of the IFM features. This figure was constructed by taking IFM spectra obtained with 22 different  $E_{\text{laser}}$  values between 1.92 eV and 2.71 eV, and represents results that would be seen by a continuously tunable laser. The light areas in Fig. 2-12(a) indicate strong Raman intensities. The IFM Raman spectra obtained with  $E_{\text{laser}} = 2.05 \text{ eV}$ ,  $2.20 \text{ eV}$ ,  $2.34 \text{ eV}$ , and  $2.54 \text{ eV}$  are shown in Fig. 2-12(b) as examples. The spectra taken at various  $E_{\text{laser}}$ , as shown in Fig. 2-12, exhibit features with a dispersive behavior, i.e., the phonon frequencies change with changing  $E_{\text{laser}}$ . Figure 2-12(a) shows the  $E_{\text{laser}}$  dependence of Raman spectra as a (quasi)continuous development, whereas Raman spectra taken



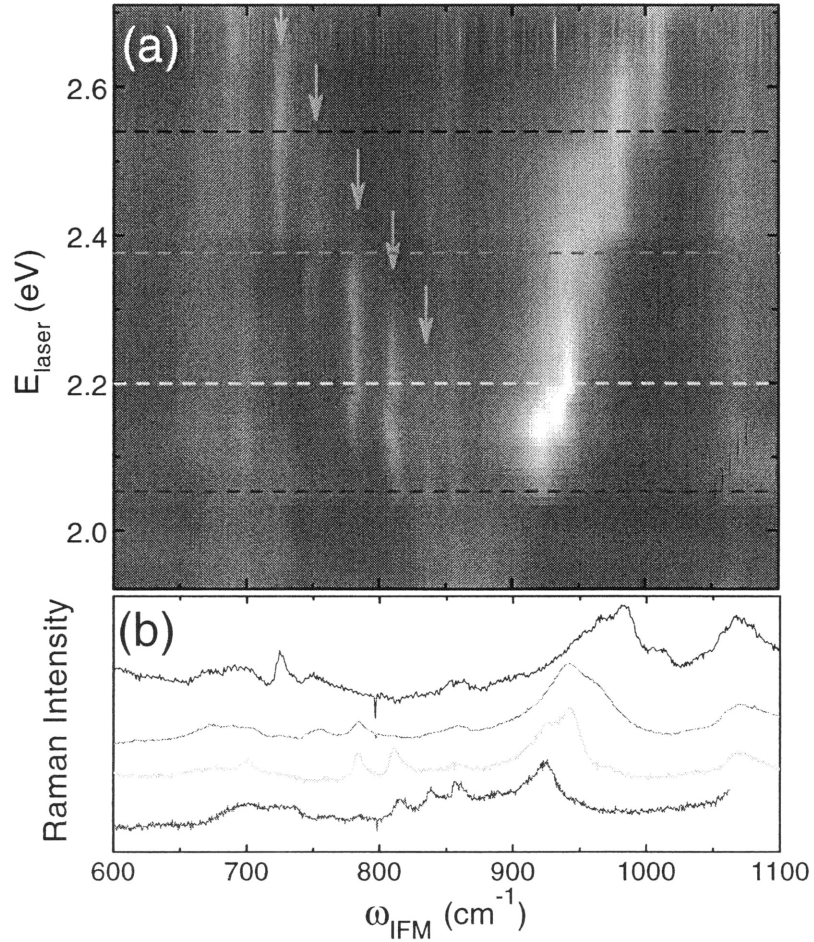


Figure 2-12: (a) Two-dimensional plot for the  $E_{\text{laser}}$  dependence for the Raman spectra of SWNT bundles in the intermediate frequency mode (IFM) range. The light areas indicate high intensity. Arrows point to five well-defined  $\omega_{\text{IFM}}^-$  features. (b) Raman spectra with  $E_{\text{laser}} = 2.05, 2.20, 2.34,$  and  $2.54$  eV. [15]

with discrete lines well spaced in energy do not make clear that the dispersion of the peaks exhibits a step-like behavior, rather than a continuous frequency change [52].

For bulk SWNT samples synthesized using the laser ablation method, the intermediate frequency features are observed as sharp peaks associated with the combination of optic and acoustic-like modes, exhibiting a step-like dispersive frequency behavior with changing excitation laser energy. Only  $\text{mod}(2n+m, 3)=1$  carbon nanotubes with low chiral angles are observed to contribute to these IFM features. The specificity of the transition has been considered a result of both electron and phonon confinement. However, IFM features associated with  $\text{mod}(2n+m, 3)=2$  SWNTs have also been observed in a previous report on isolated SWNT samples grown on a poly-silicon substrate [53]. Further studies will be needed to further understand the nature of these IFM transitions.

### **Stokes and Anti-Stokes Studies and Interband Transition Energy Determination**

In this subsection we show how measurements at the single nanotube level allow a determination to be made of the diameter and chirality of a nanotube, which is usually denoted in terms of the  $(n, m)$  indices of the SWNT [1]. In addition, single nanotube spectroscopy allows measurements to be made of the resonant window of an individual SWNT, if a suitable “tunable” laser source is available.

In the process of measuring the Raman spectra from isolated SWNTs on a Si/SiO<sub>2</sub> substrate using a fixed laser energy  $E_{\text{laser}}$ , the laser spot is focused on the substrate surface (micro Raman spectroscopy) and is scanned over the sample until the Raman signal from an isolated SWNT is observed. The Raman intensity from SWNTs is usually buried under the noise, except for a few  $(n, m)$  SWNTs, which have  $E_{ii}$  values within the resonance window of a given  $E_{\text{laser}}$ . Figure 2-14(b) shows the Raman spectra from three isolated SWNTs in resonance with an excitation laser  $E_{\text{laser}} = 1.58$  eV, taken from different spots on the Si/SiO<sub>2</sub> substrate shown in Fig. 2-14(a). From knowledge of both the breathing mode frequency  $\omega_{\text{RBM}}$  and  $E_{ii} \sim E_{\text{laser}}$ , the  $(n, m)$  geometrical structure can be defined, by comparing the calculated relative

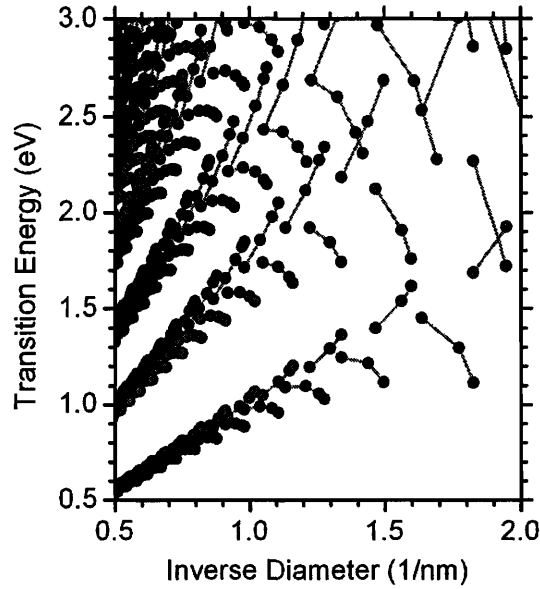


Figure 2-13: A Kataura plot that summarizes the calculated relative positions of  $E_{ii}$  and  $\omega_{\text{RBM}}$  (or  $d_t$ ). The red circles denote the transition energies for metallic nanotubes, whereas the green and blue circles denotes different  $(2n+m \text{ MOD } 3)$  types. The green circles denote those nanotubes with  $(n, m)$  indices such that  $(2n+m \text{ MOD } 3 = 1)$ . The blue circles denote the nanotubes whose  $(n, m)$  values gives  $(2n+m \text{ MOD } 3=2)$ . The more subtle distinction between these two types will be discussed in the later chapters

positions of  $E_{ii}$  and  $\omega_{\text{RBM}}$  (or  $d_t$ ), summarized into a Kataura plot, as shown in Fig. 2-13. The  $\omega_{\text{RBM}}$  is known to depend linearly on the number of carbon atoms around the tube circumference, and therefore  $\omega_{\text{RBM}}$  depends on  $1/d_t$ . In this work, the relation used to relate  $\omega_{\text{RBM}}$  to  $d_t$  for SWNTs in the diameter range  $1.2 < d_t < 1.8$  nm was found to be  $\omega_{\text{RBM}} = 2.48/d_t$  [10]. This assignment with  $\omega_{\text{RBM}} = 248/d_t \text{ cm}^{-1}$  works well for  $d_t > 1$  nm. However, for small diameter SWNTs  $d_t < 1$  nm, we need to consider in detail the curvature effect of the cylindrical surface of a SWNT on  $E_{ii}$  and  $\omega_{\text{RBM}}$ .

By using a tunable laser, it is also possible to study the resonance window of **one** isolated SWNT, giving the  $E_{11}^M$  value with a precision better than 5 meV, as shown

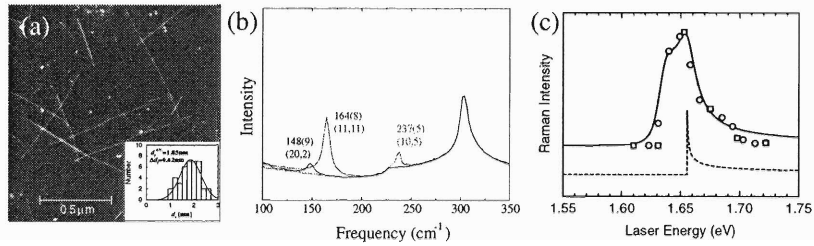


Figure 2-14: (a) AFM image of SWNTs on a SiO<sub>2</sub> substrate. The inset shows the SWNT diameter distribution of the sample. (b) Raman spectra from three different spots on the Si/SiO<sub>2</sub> substrate. The RBM frequencies (widths) and the  $(n, m)$  assignment for each resonant SWNT are displayed [10]. The 303 cm<sup>-1</sup> feature comes from the Si substrate and is used for calibration purposes. (c) Raman intensity *vs* laser excitation energy for the anti-Stokes RBM feature at the 173.6 cm<sup>-1</sup> assigned to an isolated (18,0) SWNT on a Si/SiO<sub>2</sub> substrate [16]. The predicted resonant window is shown by the solid curve, while the vHS in the DOS at 1.655 eV is shown by the dashed curve. Circles and squares indicate two different runs taken over the laser energies.

in Fig. 2-14(c) [16]. Here the resonance window for the anti-Stokes process is shown to have a full width at half maximum intensity of only 8 meV and to be asymmetric in lineshape, reflecting the asymmetric lineshape of the van Hove singularity [dotted curve in Fig. 2-14(c)]. To observe the asymmetry in the resonance window, its linewidth must be small. The appearance of spiky vHS peaks in the DOS is a general effect of quantum confined 1D energy bands, but this effect is enhanced in SWNTs because of their small  $d_t$  values.

## 2.4 PL Spectroscopy and beyond

In addition to the RRS technique, optical absorption and photoluminescence spectroscopy (PL) have become an increasingly important technique for the characterization of single-wall carbon nanotubes (SWNT) [20–24]. Resonance Raman spectroscopy, optical absorption and PL spectroscopy have all been used to determine the  $E_{ii}$  energy values. The ability to probe the electronic structures of a large number of semiconducting SWNTs has made these alternative optical measurements powerful and complementary methods to resonance Raman spectroscopy (RRS) for the characterization of SWNTs. The observation of the  $E_{11}^S$  energy gap for semiconducting SWNTs is possible by measuring PL, and interesting 3D plots can be constructed, showing the spectral interdependence of the absorption and emission energies. The intense peaks, indicating strong optical absorption at a given  $E_{ii}$  and emission at  $E_{11}$ , are related to one specific  $(n, m)$  SWNT. Since the PL measurements are usually carried out with a lamp source that covers a large spectrum of light, a large number of different tubes are measured at the same time. The  $(n, m)$  identification can then be established by comparing the  $(2n + m = \text{constant})$  family pattern with theoretical prediction.

Similar sample characterization can also be carried out using RRS [8, 54], and the  $E_{ii}$  values can be obtained by carefully constructing resonance windows for the Stokes and anti-Stokes processes using a large number of closely spaced excitation energies. Since one or more nearly tunable laser excitation sources are required for such RRS

measurements, the corresponding characterization process is generally slower. However, the  $E_{ii}$  values measured from RRS and PL have been found to be the same [8].

The limitation for PL is related to systems where non-radiative electron-hole recombination readily occurs. Therefore, light emission from metallic SWNTs or from SWNTs in bundles cannot be observed. For such samples, resonance Raman experiments could be a complementary method used for  $E_{ii}$  determinations. Near-infrared spectroscopy can be used for a quantitative evaluation of the carbonaceous purity of bulk quantities of as-prepared SWNTs in a solution-phase [55], which is important for practical applications. Far-infrared spectroscopy has been used to study electrons in SWNTs, giving information about plasmons and about the unusual tiny gaps occurring in quasi-metallic SWNTs due to curvature effects [56]. With recent advances in laser technology, it is also possible to do nanotube characterization using Rayleigh scattering spectroscopy [57], using a super-continuum white light source generated from a ultra short-pulsed femtosecond laser. With an isolated SWNT grown across a long trench, it is possible to directly measure the  $E_{ii}$  transition at the single nanotube level, for both metallic and semiconducting nanotubes. When the method is used in conjunction with electron diffraction experiments, one can establish the direct relationship between the exact nanotube geometric structure and the electronic structure (as observed using optical methods) without any empirical extrapolation from theoretical calculations. Such a direct experimental observation is very powerful, and it can clear up many long-standing questions related to the detailed interpretation of optical spectra based on different theoretical calculations. On the other hand, the technique has not been widely explored in the nanotube community because the experiment could only be used for SWNTs suspended over a longer trench over  $10\mu m$  and, thus, not suited for SWNTs produced by bulk synthesis methods. Also, since Rayleigh scattering measurements require an unconventional continuous white light source, working in conjunction with signal collection apparatus tailored to the experiment, only a few groups were able to carry out the experiment [57].

## 2.5 Exciton Formalism and Optical Selection Rules

The advances in optical techniques and the curious  $E_{22}^S/E_{11}^S$  ratio problem have led to developments in the theoretical description of strongly bound state of electron-hole pairs in carbon nanotubes. In particular, the symmetry-based selection rules within the approach of the group of the wavevector has provided important guidelines to understand the theoretical and experimental optical spectra of SWNTs. In this section, a brief description is presented on the notation used for describing the symmetry of exciton states in a chiral SWNT, developed within the formalism of the group of the wavevector [58]. The factor groups for the wavevector  $k$  at the center ( $k = 0$ ) and edge of the Brillouin zone ( $k = \pi/T$ ) are isomorphic to the  $D_N$  ( $D_{2nh}$ ) point group for chiral (achiral) nanotubes, while the factor group for a general wavevector  $k$  is isomorphic to the group  $C_N$  ( $C_{2nv}$ ). Here  $N$  ( $2n$ ) denotes the number of hexagons in the unit cell for chiral (achiral) nanotubes and  $T$  is the length of the real space unit cell. The irreducible representations of the factor groups of nanotubes are labeled by the quasi-angular momentum quantum number  $\mu$  which varies between  $1 - N/2$  and  $N/2$ . This quantum number  $\mu$  is related to the projection of the compound symmetry operation ( $R|\tau$ ) in the circumferential direction of the nanotube, and can be associated with the concept of cutting lines. Another quantum number involved is the wavevector  $k$ , which is related to translational symmetry. There are also parity quantum numbers related to a  $C_2$  rotation (a  $\pi$  rotation perpendicular to the tube axis, bringing  $z$  to  $-z$ ), reflections, and inversion operations.

To summarize the excitonic notation derived from group theory in nanotubes, Fig. 2-15 shows a schematic diagram of the band edge excitonic state with a given index  $|\mu|$ . Since the exciton wave function for the one-dimensional (1D) SWNTs consists of a linear combination of products of conduction (electron) and valence (hole) eigenstates, it is necessary to solve a Bethe-Salpeter equation in an *ab initio* determination of the coefficients to incorporate many-body effects and to describe the coupling between electrons and holes. In general, the electron-hole interaction will mix states with all wavevectors and all bands, but for moderately small-diameter nan-

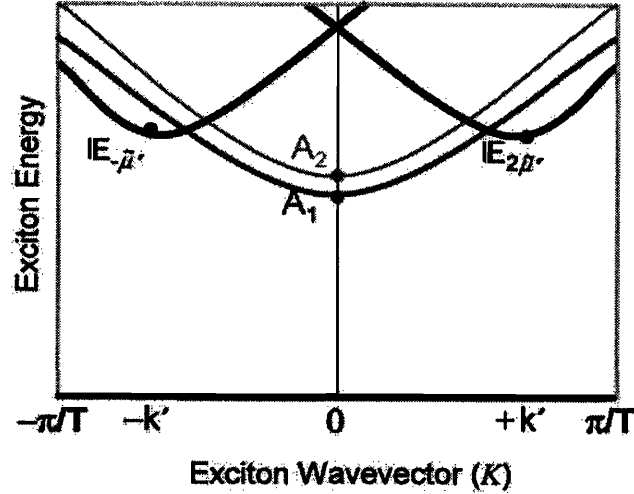


Figure 2-15: A schematic diagram of an excitonic band for a chiral nanotube. The electron, hole and exciton states at the band edges are indicated by a solid circle and labeled according to their irreducible representation. Dark (thicker) lines correspond to the  $E_\mu$  2D representation while the blue lines (thick) correspond the  $A_1$  excitons while the cyan lines (thin) correspond to the  $A_2$  excitonic states. The excitonic band structures shown here are only schematic illustrations. Group theory does not order the values for the eigenenergies or for the energy dispersions.

otubes ( $d_t < 1.5$  nm), the energy separation between singularities in the single-particle 1D JDOS is fairly large. Thus, it is reasonable to consider, as a first approximation, that only the electronic bands contributing to a given 1D singularity will mix to form the excitonic states, and the usual effective-mass and envelope-function can be used.

In Fig. 2-15, the band edge state is labeled by  $0E_\mu$  symmetry [58–60], where 0 denotes the  $n = 0$  envelope function state and  $E_\mu$  refers to its symmetry type for chiral SWNTs. To obtain the selection rules for the optical absorption of the excitonic states, it is necessary to consider that the ground state of the nanotube transforms as a totally symmetric representation ( $A_1$ ) and that only  $K = 0$  excitons can be created due to linear momentum conservation. For light polarized parallel to the nanotube axis, the interaction between the electric field and the electric dipole moment in the nanotube transforms as the  $A_2$  representation for chiral nanotubes [58]. Therefore, from the



4 excitons obtained for each envelope function, only the  $A_2$  symmetry excitons are optically active for parallel polarized light, the remaining three being dark states. Thus, an experimental Kataura plot can be interpreted as the plot of the energy of the bright exciton state with  $\mu = 0$  as a function of tube diameter.

# Chapter 3

## Nanotube Growth and Separation

### 3.1 Introduction

In this chapter, a brief review is presented on some of the important developments in nanotube growth and separation that have significantly shaped the research described in this thesis. The chapter will begin with a discussion on some of the challenges and progresses that have been made on the research of nanotube synthesis. A brief introduction will be presented on two widely used CO-CVD based SWNT synthesis methods, the HiPco process and the CoMoCAT process. Then, Sec. 3.3 will discuss how different purification and sorting techniques can be used, in conjunction with better nanotube synthesis methods, to achieve control over the length, diameter, chirality, and metallic/semiconducting properties of the SWNT materials for commercial applications.

### 3.2 Controlled Growth of SWNTs

Recent developments in carbon nanotube research have been able to provide physical scientists with a good understanding of the one dimensional structure-property relations in carbon systems. On the other hand, the lack of a detailed understanding of the nanotube growth mechanism remains the biggest obstacle in making commercialized nanotube devices. Because of the unusually close connection between nanotube

optical and electronic properties (such as their metallicity) and their geometric structure, it is crucial to have precise control over nanotube growth and assembly before device fabrication can be achieved.

Numerous research efforts have been made to improve controlled nanotube synthesis, and these methods have given rise to different degrees of success. Arc-discharge [61, 62] and laser ablation [63] were the first methods that enabled bulk production of SWNTs at the gram level. Both methods produce tangled SWNT bundles by condensing hot gaseous carbon atoms generated from the evaporation of solid carbon. On the other hand, the large amount of energy consumed in decomposing solid carbon materials, as well as the large amount of amorphous soot by-products involved make these two methods less desirable candidates for many commercial applications that require cheap and high quality SWNT samples. In comparison, the developments in chemical vapor deposition (CVD) based nanotube growth has made CVD one of the most important commercial methods for SWNT production because it provides a cheaper and more straight forward way to scale up the production of high quality SWNTs to industrial levels. CVD is generally used to describe heterogeneous reactions in which both solid and volatile products are formed from a volatile precursor through chemical reactions, and the solid products are deposited onto a substrate [64–66]. CVD has been successfully used for industrial-scaled production of carbon materials for more than 20 years, and carbon fibers and multi-walled carbon nanotube (MWNT) materials [67, 68] produced using CVD has been widely used in various carbon films and composite products. Only recently has the growth of SWNTs using CVD become possible [69–73]. Since it is possible to use the CVD method to produce well-separated individual nanotube samples that can be used in conjunction with photolithography processing, these nanotubes can be directly used to fabricate nano-scaled devices. In the following sections, I will go into a more detailed discussion of CVD growth of SWNTs using CO as a stock gas. The section will discuss how diameter control can be achieved by careful controlling the growth conditions. The HiPco and the CoMoCAT processes, two of the most important CO-CVD synthesis methods will also be introduced. Both methods are known to create high quality

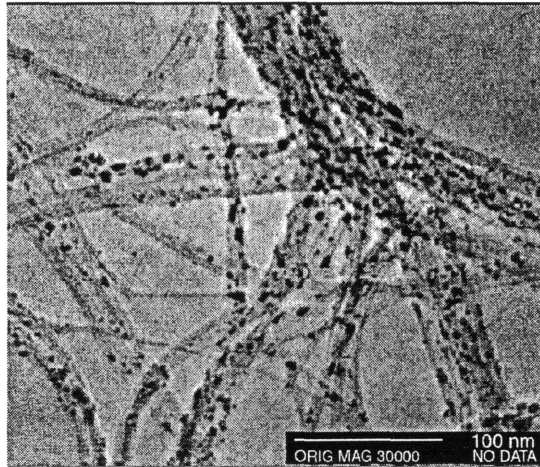


Figure 3-1: Transmission electron microscopy images of single-walled carbon nanotubes (SWNTs) synthesized by HiPco process [17]

SWNT bundles with relatively a small average diameter.

### 3.2.1 CO Chemical Vapor Deposition

Carbon monoxide (CO) was one of the very first feed gases used in 1996 in the growth of SWNTs using chemical vapor deposition (CVD) in 1996 [71]. It was reported that most of the resulting SWNTs had catalytic particles attached to the ends, indicating that the growth of SWNTs was catalyzed by preformed nanoparticles. Due to safety reasons, the use of CO as stock gas in the growth of SWNTs is not as prevalent as the use of methane, ethylene, or alcohol, which are relatively cheaper and safer alternatives. However, the use of CO as a feed gas does offer certain advantages over hydrocarbons in reducing the amount of amorphous carbon present in the sample.

#### The HiPco Process

An important development in the CO CVD-based SWNT synthesis is the HiPco process. HiPco stands for high-pressure catalytic decomposition of carbon monoxide.

This process makes use of high-pressure CO as the carbon source, and the catalysts are formed in the gas phase from a volatile organometallic catalyst precursor introduced into the reactor. The organometallic species decompose at high temperature and form metal clusters on which SWNTs nucleate and grow. The HiPco process was originally developed at Rice University. [74, 75] In this procedure, high-pressure (30100 atm) and high temperature (1050°C) CO with  $\text{Fe}(\text{CO})_5$  as a catalyst precursor produced high-quality SWNTs at a rate of approximately 450 mg/h. The product consists of entangled SWNT bundles interspersed with Fe nanoparticles and amorphous carbon, as shown in Fig. 3-1. The production rate for the HiPco process was found to increase with increasing pressure up to 50 atm [75], indicating that this is a surface-reaction-limited process. The CVD methods that use such volatile organometallic precursors catalysts are normally called floating catalyst CVD methods. To support the floating catalyst synthesis, the furnace used in these new CVD systems are in a vertical configuration instead of the more commonly used horizontal configuration. In conjunction with using CO stock gas, it was also found that the addition of hydrogen can greatly enhance SWNT synthesis by CO disproportionation [76, 77]. The effect of hydrogen can be explained in two possible ways. The hydrogen molecules can directly reacts with CO, producing carbon and  $\text{H}_2\text{O}$ . The hydrogen molecules can also interact with catalyst nanoparticles, so that the activity of the catalyst toward CO disproportionation is enhanced.

### **Diameter Control and the CoMoCAT Process**

Another important advance in the CO-based CVD method is the CoMoCAT process [78, 79] developed at Oklahoma State University. The process has been gaining popularity because it produces bulk SWNTs sample with very narrow and well defined diameter and chirality distribution. Diameter control of SWNTs has become a very important subject for both basic research and for industrial applications. In general, the diameter of SWNTs is believed to be determined by the size of the catalyst nanoparticles. Since catalyzing metal/metal oxide nanoparticles tend to aggregate during the growth process, the resulting SWNT samples usually have a broad distribution of

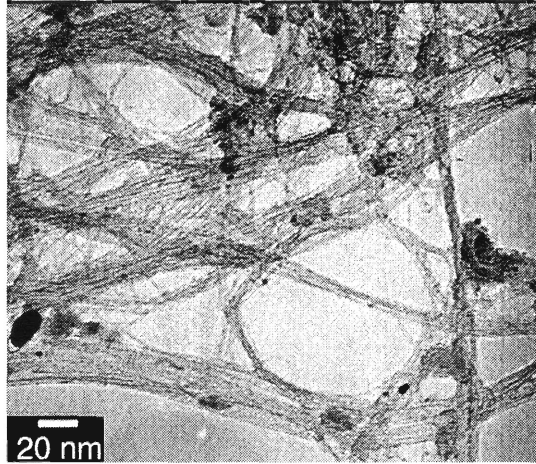


Figure 3-2: Transmission electron microscopy images of single-walled carbon nanotubes (SWNTs) synthesized by CoMoCAT process [17]

diameters. A popular approach to control the nanotube diameter distribution is to allow the catalyzing nanoparticles to be mono-dispersed in a variety of host materials to prevent aggregation. Metallo-proteins, zeolite molecules, and dendrimers of different sizes have been used as templates to control the sizes of the metallic catalyst particles [80–83]. It is also possible to control the sizes of metallic nanoparticles by tailoring the synthesis to form clusters with well-defined stoichiometry in the metallic nanoparticles. The different methods have been able to achieve fairly good control over the diameter range between 1.1 – 1.4nm. In the case of zeolite-derived SWNTs, the average diameter can be as small as 0.4nm. On the other hand, since the size control of host materials or the tailored synthesis of metal catalysts requires either fairly expensive precursors or sophisticated multi-step synthesis, it is more difficult to scale up the nanotube production to industrial levels.

In comparison, the CoMoCAT process provides a simpler alternative to produce bulk SWNT samples with a narrow diameter distribution. In this process, a silica-supported bimetallic Co-Mo catalyst and a fluidized bed CVD reactor were used to produce a large quantity of SWNTs [78, 79]. It has been found that the product

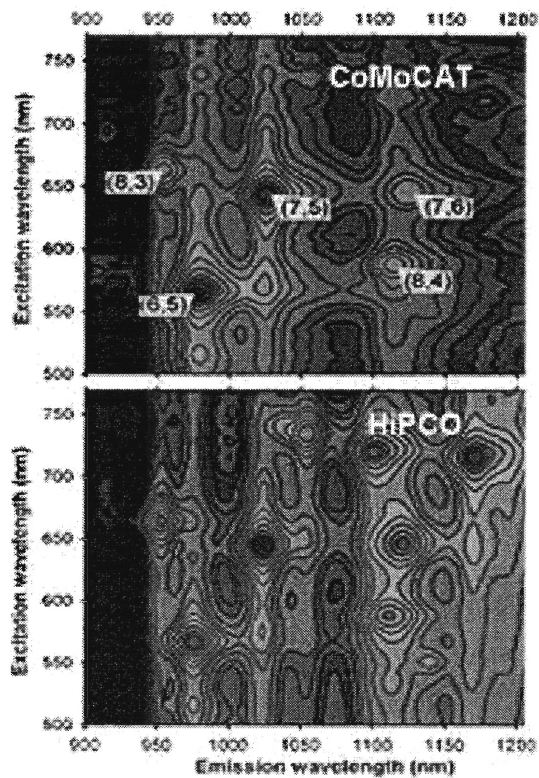


Figure 3-3: A comparison of the photoluminescence (PL) spectra of a HiPco and CoMoCAT SWNT suspension that are dispersed in sodium dodecyl sulfate (SDS) solution [18]. The PL characterization shows that the SWNT samples made by the CoMoCAT process have smaller average diameters, and the diameter distribution is narrower, compared to SWNTs made with the HiPco process.

composition produced by this method depends on the Co:Mo ratio and on catalyst treatments that precede nanotube growth. When the total metallic loading of the catalyst was at 2 weight percent and a Co:Mo molar ratio of 1:3 was used, the SWNTs produced by this process have very narrow diameter and chirality distributions [18], around  $1.05 \pm 0.05$  nm. The final product is also in the form of entangled SWNT bundles, as shown in Fig. 3-2. However, relatively few catalyst particles are observed in the sample. Fig. 3-3 shows the contour plots of the normalized fluorescence intensities for the SWNTs produced using the CoMoCAT method and the HiPco method. One can see that the CoMoCAT-produced SWNTs not only have a narrower diameter distribution, but the as-produced SWNT materials have a large concentration of (7, 5) and (6, 5) nanotubes.

### 3.3 Nanotube Separation

As rapid progress is being made in nanotube synthesis, different chemical and biochemical research strategies used in nanotube separation have also been rapidly developing in parallel. Since diameter control in nanotube synthesis does not strongly discriminate between metallic nanotubes and semiconducting nanotubes, the separation of bulk SWNT samples based on metallicity and chirality has been a field of enormous interest. In this section, we briefly review the developments in nanotube dispersion, assisted by different wrapping agents, as well as how these agents facilitate the different nanotube separation processes.

#### 3.3.1 Polymer and DNA-assisted Dispersion and Separation

Since most of the separation strategies aim to address the different physicochemical characteristics of individual nanotube, it is crucial for bulk SWNTs samples to be dispersed into small bundles containing only a few nanotubes or individually dispersed nanotubes. The choice of the dispersion medium is particularly important, and a variety of surfactants have been used to obtain highly dispersed SWNT solutions. [84–88]



By exploring the complex physicochemical interactions of carbon nanotubes, it is found that surfactant amines in particular seem to have different chemical affinity for metallic (M) and semiconducting (S) SWNTs. Researchers at the University of Connecticut reported a purification approach for the bulk separation of M and S SWNTs using the enhanced chemical affinity of semiconducting SWNTs to octadecylamine [ODA,  $\text{CH}_3(\text{CH}_2)_{17}\text{NH}_2$ ] [88]. Since weak donor/acceptor interactions occur between the amine group of ODA and semiconducting SWNTs and since these interactions appear to act together with the previously reported SWNTCOO/ $\text{NH}_3-(\text{CH}_2)_{17}\text{CH}_3$  zwitterions, separation is promoted. [89] Unlike zwitterions, which are held together by the low dielectric constant of the solvent, the surfactant-amine-nanotube donor/acceptor complexes are further stabilized by means of self-organization of the long aliphatic tail of ODA along the graphitic surface. [88] Resonance Raman spectra show that the precipitated and supernatant fractions that precipitate are significantly enriched in metallic nanotubes and the supernatant is enriched in semiconducting tubes [90]. Further enrichment is expected by repeating this separation process sequentially.

In terms of physical separation, one of the most promising reports involves an dielectrophoretic separation of metallic SWNTs from semiconducting SWNTs. [91] HiPco SWNTs solubilized with sodium dodecyl sulfate (SDS) in  $\text{D}_2\text{O}$  at concentrations of  $10\text{mg}/L$  were subjected to dielectrophoresis at a frequency of 10 MHz and a field of about  $2L$  and  $103V/cm$ . Based on the differences in the relative dielectric constants of metallic versus semiconducting SWNTs with respect to the solvent, the metallic nanotubes were attracted toward the microelectrode array, leaving the semiconducting nanotubes in the solvent, which was subsequently removed. More recent work indicates that metallic SWNTs undergo preferential electron transfer with diazonium salts in aqueous solution, in contrast to semiconducting SWNTs [92]. This apparent selectivity appears to be driven by the larger availability of electrons (for metallic SWNTs) near the Fermi level, which can provide greater stabilization of a charge-transfer intermediate preceding bond formation. This selective functionalization of the metallic SWNTs, followed by a high-temperature elimination step to remove these functionalities and restore the original electronic structure of the

nanotubes, might open a new venue for the bulk separation of metallic from semiconducting SWNTs [92].

In addition to the use of polymeric surfactants, single-stranded DNA has also been shown to be an effective wrapping agent that helps to disperse nanotube bundles in water. It was shown that single-stranded DNA (ss-DNA) strongly binds to HiPco and CoMoCAT SWNTs through  $\pi$ -stacking and thus provides bundle exfoliation and SWNT solubilization in water. Moreover, since the phosphate groups on a DNA-SWNT hybrid provide a negative charge density on the surface of the carbon nanotube, the distribution of which should be a function of the DNA sequence and the electronic properties of the tube. Based on this, the DNA-metallic SWNT complex is predicted to have less surface charge than the DNA-semiconducting SWNT complex, due to the opposite image charge created in the metallic tube. Using custom-synthesized 60-base ss-DNA oligonucleotides composed of periodic guanine and thymine nucleosides, the dispersed SWNTs were injected into a strong anion exchange column and eluted with a linear salt gradient to give the DNA-SWNTs as a single broad peak. By collecting a number of different fractions within this peak, by using the diameter selective CoMoCAT starting materials, it is possible to selectively fractionate out a fraction that is strongly enriched in specific  $(n, m)$  species [86, 93, 94]. These strongly enriched samples hold promise for advancing device development. By taking advantage of a SWNT sample highly enriched in a single  $(n, m)$  species, one can also probe several different phonon-assisted processes not usually separately identified in 3D solid state systems. The detailed optical study of this effect will be discussed in Chapter 5 and refch6 in this thesis.

### 3.3.2 Length Sorting

In addition to separation by diameter and metallicity, the sorting of the SWNTs according to their length has also been an area of on-going investigation, since a precisely controlled aspect ratio is particularly desirable for industrial applications such as field emission devices. Different techniques have been employed for length sorting, and in most cases, the sorting is achieved by chromatographic techniques [19,

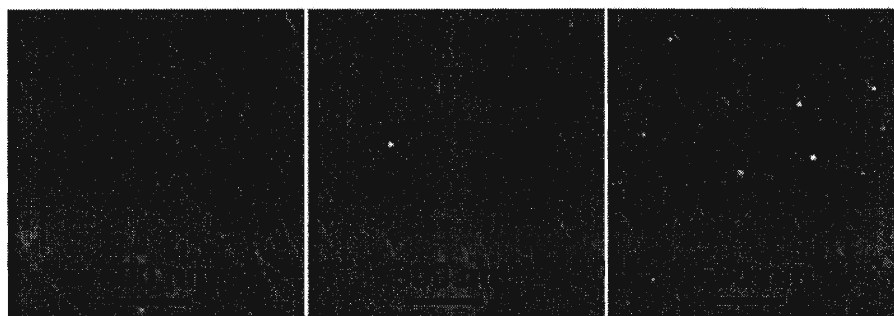


Figure 3-4: AFM images of three representative SEC fractions deposited onto alkyl silane-coated  $\text{SiO}_2$  substrates [19].

84, 95, 96], which are expected to be particularly important for the length fractionation of shortened SWNTs with sizes of less than 300 nm [19, 84, 95, 96]. Even though capillary electrophoresis [87] and field-flow fractionation [97] have also been employed, these techniques appear to be more effective for longer nanotubes.

A particularly interesting separation method has been reported using the size exclusion chromatographic sorting of DNA-wrapped CoMoCAT sample, as mentioned before [19]. The DNA-SWNT materials can be eluted through a series different columns with different pore sizes to achieve the desired separation. The Sepax CNT-SEC columns, designed specifically for DNA-coated materials have near 100% recovery of the loaded DNA-SWNT materials. Since ion exchanged chromatography was able to produce a fraction that is highly enriched in the (6, 5) SWNT, the subsequent length sorting potentially can yield complete control over the nanotube structure. Figure 3-4 shows an AFM characterization of three representative SEC fractions deposited onto alkyl silane-coated  $\text{SiO}_2$  substrates. The AFM characterization has shown that the separation yields a fairly uniform length distribution, with about 10% variation in length. The availability of SWNT samples with such precisely controlled geometry with average lengths much shorter than the wavelength of light not only facilitates device engineering, but it will also allow one to study the effects of the end cap structure, as well as finite-length effects associated with the broken translational symmetry in the axial direction of SWNTs. The implications of such finite-length

effects will be discussed in Chapter 7 of this thesis.

### 3.4 Summary

The challenges surrounding the growth and separation of SWNTs have attracted a great deal of attention since these materials were first identified. Significant progress has been made in understanding the growth mechanism and the separation methods. Even though extensions of these processes to the bulk scale requires further work in optimization, steps have been taken toward a precise control over the nanotube geometry. Such control not only holds promise for future device applications, but the availability of SWNT samples with precisely controlled geometry has also facilitated our understanding of physical phenomena associated one dimensional systems. Some of the interesting 1D phenomenon observed in a DNA-SWNT sample enriched with the (6, 5) species will be discussed in the following chapters.

# Chapter 4

## Optical Characterization of DNA-wrapped SWNTs

### 4.1 Introduction

As the nature of materials research becomes increasingly interdisciplinary, numerous long-standing research problems have been revisited in recent years using biological methods for materials modification. One of the most exciting applications of such biological approaches is the dispersion and fractionation of single wall nanotubes (SWNTs) using the single stranded deoxyribonucleic acid(ss-DNA) polymer [86, 94].

Previous studies [86, 94] have shown that ss-DNA of the poly-d(GT) sequence forms a stable complex with individual SWNTs via the aromatic interactions between the guanine (G) and thymine (T) bases and the nanotube sidewall. Furthermore, by passing such DNA-nanotube (DNT-SWNT) hybrids through an ion exchange chromatography (IEC) column, fractions strongly enriched with SWNTs of specific metallicities and with a modified diameter distribution can be obtained [94, 98].

Such enrichment achieved by IEC fractionation allows one to obtain SWNT samples with highly selective  $(n, m)$  chirality and diameter distributions that circumvent the problems in nanotube synthesis that lack chirality control. However, to further apply these processed SWNTs to either device applications or to fundamental studies, it is necessary to understand the effects of the electronic structure of SWNTs,

introduced by DNA-wrapping and by fractionation.

To study the effects of DNA-SWNT interactions, resonant Raman spectroscopy (RRS) and photoluminescence (PL) studies were carried out on bundled DNA-SWNT hybrid samples. A DNA-SWNT hybrid sample enriched with the (6, 5) species obtained from IEC separation was also studied to understand the effect of the (6, 5)-enrichment. The Raman measurements show that the DNA wrapping is a diameter selective process for the CoMoCAT nanotubes, and the fractionation and (6, 5) enrichment procedures further decrease the metallic components of the sample, as shown previously for the case of HiPco SWNTs. Photoluminescence (PL) mapping was carried out to study the PL process in the DNA-SWNT hybrid system. The  $i^{th}$  excitonic transitions,  $E_{ii}$ , were measured over a wide range of excitation energies,  $E_{laser}$ , for both samples. The values of the radial breathing mode (RBM) frequency,  $\omega_{RBM}$ , and the  $E_{ii}$  of the DNA-SWNT hybrids measured by RRS and PL experiments can be well-correlated with the previously established ( $2n+m=\text{constant}$ ) family patterns for SDS-encapsulated HiPco nanotubes [20].

By isolating individual nanotubes from inter-tube interactions and by removing most of the metallic nanotubes to create a more homogeneous nanotube environment, thereby increasing the excited state lifetimes for PL, DNA-wrapping and fractionation provide a new means for probing the nanotube 1D electronic structure. The good isolation achieved by DNA-wrapping and by the removal of metallic nanotubes through fractionation brings out well-defined components of the G-band features and suppresses the  $E_2$ -type phonon transitions. The RBM frequencies are found to be relatively insensitive to the nanotube environment. Through monitoring the shifts in the interband transition energies for DNA-SWNTs, relative to SDS-encapsulated nanotubes and fractionated, (6, 5)-enriched DNA-SWNT samples using RRS and PL, the environmental effects are found to play a small but non-negligible role regarding the  $E_{ii}$  determination. The electronic structure of nanotubes can be perturbed differently when the tubes are situated in different environments, and the  $E_{ii}$  can change by different amounts.

## 4.2 Experimental

Thirteen laser excitation energies,  $E_{laser}$ , were used in the RRS measurements, including the 2.71 eV (458 nm), 2.60 eV (477 nm), 2.54 eV (488 nm), 2.50 eV (497 nm), 2.47 eV (502 nm), 2.41 eV (514 nm), 2.18 eV (568 nm), and 1.92 eV (647 nm) lines from an Ar/Kr laser; 1.97 eV (633 nm), 1.94 eV (640 nm), and 1.88 eV (658 nm) from a dye laser (using DCM dye), pumped by an Ar<sup>+</sup> ion laser; 1.97 eV (633 nm) from a HeNe laser; and 2.33 eV (532 nm) from a crystal laser. Most of the resonance Raman experiments were carried out at the micro-Raman laboratory at Universidade Federal de Minas Gerais in Belo Horizonte, Brazil, using a Dilor XY triple monochromator spectrometer was used in conjunction with the Ar/Kr and the dye laser. On the other hand, an air-cooled CCD detector attached to a Renishaw 1000B micro-Raman system at the Boston University Photonic Center was used in conjunction with 1.96 eV and 2.33 eV excitation. All scattered light was collected through a 50× microscope objective in the backscattering geometry. The laser power level was kept below 0.5 mW to prevent overheating the sample. By systematically monitoring the changes in the normalized Stokes to anti-Stokes intensity ratios at different power levels between 0.05mW and 0.488mW, the average temperature (T) of the DNA-SWNTs samples was extrapolated to be ~350K. Although a small degree of heating (~50 K), was observed, the changes in spectral intensities do not shift the  $E_{22}^S$  value by more than 2 meV, which is smaller than the uncertainty in the experimental  $E_{ii}$  determination (5 meV) [8].

SWNTs produced using CoMoCAT catalysts [99, 100], which yield SWNTs with a narrow diameter ( $d_t$ ) and chiral angle ( $\theta$ ) distribution, were used as the starting material, following previously described procedures [86, 94]. CoMoCAT-based DNA-SWNT samples were analyzed by RRS (on dried SWNT bundles and DNA-SWNT hybrids) and by PL (on DNA-SWNT hybrids in solution) experiments.

The dried DNA-SWNT samples were prepared by dropping 30 $\mu$ L of the stock solution onto a sapphire substrate 1 $\mu$ L at a time. The drops were allowed to dry into a thick layer of nanotubes. An as-produced, CoMoCAT-based, non-fractionated

DNA-SWNT sample and a (6,5)-enriched DNA-SWNT sample obtained from the IEC fractionation process [94] were all studied. Preliminary optical absorption characterization [93] have shown that the fractionated sample is strongly enriched in (6, 5) SWNTs.

The PL experiments were carried out in a DNA-SWNT hybrid solution diluted 20 times from a stock solution at the semiconductor optics laboratory at the Universidade Federal de Minas Gerais, Brazil. The samples were then placed in a glass cuvette with an optical beam path of 1mm. The sample was excited using a tunable Ti:Sapphire laser, which is pumped by a high power Ar<sup>+</sup> ion laser. The emitted light was collected in a back scattering geometry and was focused onto a North Coast Ge detection system and a Spex 750M Spectrometer.

## 4.3 Resonance Raman Characterization Based on First Order Raman Features

### 4.3.1 RBM

Figure 4-1 (a) shows the changes in the RBM spectra of different samples at  $E_{laser} = 2.19\text{eV}$ . The differences between the RBM spectra between the as-grown, unwrapped nanotubes and the DNA-wrapped nanotubes indicate that the wrapping mechanism is  $d_t$ -selective, selecting nanotubes within a specified  $d_t$  range that fits the specific dimensions of the GT-DNA. As shown in Fig. 4-1(a), the intensity of the RBM for smaller and larger diameter nanotubes outside of the range of  $240 - 320 \text{ cm}^{-1}$  are largely reduced or eliminated as the GT-DNA strands wrap around the nanotubes. The mechanism for DNA-assisted separation of HiPco SWNTs using IEC has been discussed in detail in previous works [86, 94]. The mechanism of DNA-wrapping for HiPco and CoMoCAT SWNT is the same. However, the  $d_t$  selectivity is more clear in the case of DNA-wrapped CoMoCAT nanotubes. This is probably a result of the smaller and narrower diameter distribution of the CoMoCAT nanotubes that matches better with the pitch angle for the GT DNA polymer. The separation of nanotubes by



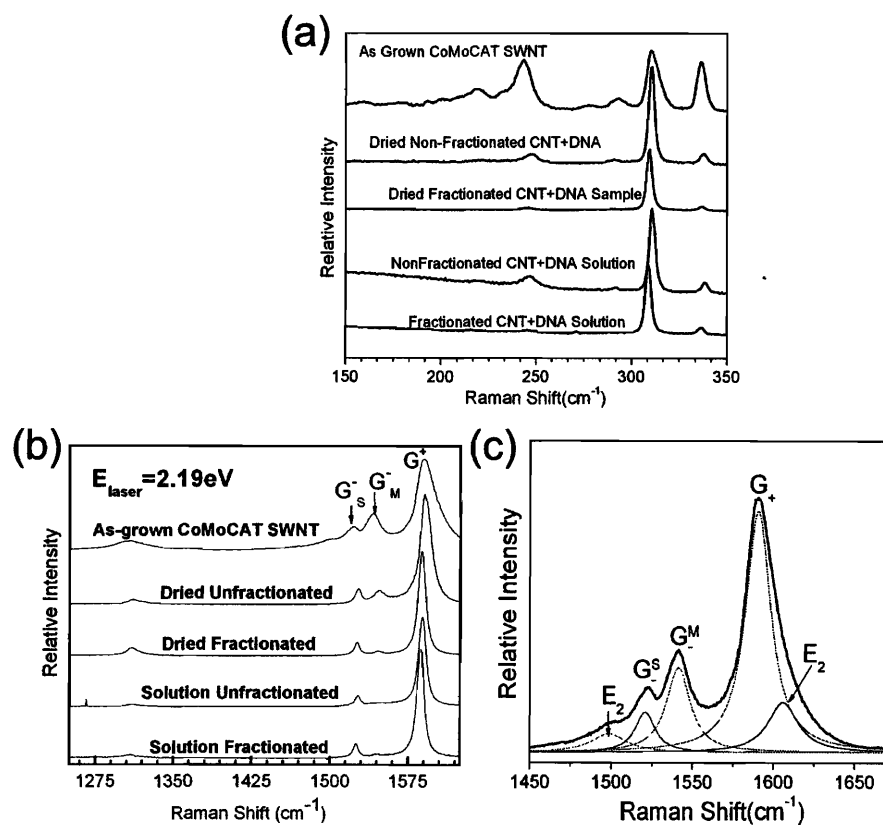


Figure 4-1: (a) A comparison of RBM spectra of CoMoCAT bundles and DNA-wrapped CoMoCAT SWNTs taken under different preparation conditions (see text). b) A comparison of the  $G$ -band spectra of different CoMoCAT-based DNA-SWNT samples taken with 2.19eV laser excitation (see text). After the bundles are broken up by DNA-wrapping, the different species within the bundle only interact weakly. A magnified trace for bulk CoMoCAT SWNT materials is shown in (c). The spectrum was fitted using Lorentzian functions, and the weak  $E_2$  components that only occur in as-grown materials have been identified.

$d_t$  and metallicity can be further achieved by IEC fractionation. A similar separation mechanism is observed in IEC-based separation using DNA-wrapping HiPco starting materials. However, because the center of the diameter distribution for the HiPco SWNT starting materials is slightly larger, and with a larger spread in diameter distribution, the degree of  $(n, m)$  enrichment achieved using the HiPco SWNTs is as high as for the case of using the CoMoCAT SWNT as starting materials, as discussed in the previous chapter. Compared to the *as-grown* CoMoCAT SWNT and the non-fractionated DNA-SWNT samples, the  $\omega_{RBM}$  for the (6,5)-enriched, fractionated sample seems to be slightly up-shifted by about  $1\text{-}2\text{cm}^{-1}$ . Since the IEC fractionation is a separation method that separates different species in a mixture based on the surface charge carried by the individual constituent, the very small up-shift observed in the fractionated sample is probably a result of the altered charge transfer property between DNA molecules and SWNTs during the fractionation process.

### 4.3.2 G-band

The environmental effects of DNA-wrapping and the different S to M nanotubes ratios within the sample are shown in the G-band spectra of Fig. 4-1 (b). Figure 4-1 (b) shows a comparison of the G-band spectra of different environments taken at  $E_{laser} = 2.19$  eV. Since previous PL experiments [22, 99] showed that 2.19 eV excitation is strongly in resonance with the  $E_{22}^S$  transition of the (6,5) nanotube, the G-band Raman spectra in Fig. 4-1 (b) are dominated by the resonant transitions of the (6,5) nanotubes, as indicated by the dominant RBM peak at  $310\text{ cm}^{-1}$ . Progressively narrower linewidths of the various G-band components are seen in Fig. 4-1 as the intertube interactions are first reduced by DNA-isolation, then as the DNA-SWNT sample become (6,5)-enriched, and finally as the DNA-hybrids are separated from one another by solvation, reflecting the progressively more homogeneous environment of the (6,5) SWNTs. This observation is consistent with the decreasing linewidth as the SWNTs are wrapped with ss-DNA strands, and as the sample becomes (6,5)-enriched.

DNA-wrapping and fractionation also affect the intensity and frequencies of the

various  $G$ -band components, as introduced in Section 2.3. Five components were observed in the  $G$ -band spectra of the CoMoCAT starting material in Fig. 4-1. The peak at  $1590\text{ cm}^{-1}$  can be associated with the  $d_t$ -independent  $G^+$  feature composed of components with  $A/E_1$  symmetry, whereas the peaks at  $1541\text{ cm}^{-1}$  and  $1526\text{ cm}^{-1}$  can, respectively, be associated with the  $d_t$ -dependent  $G^-$  feature for the larger  $d_t$  M SWNTs ( $G_M^-$ ) and the smaller  $d_t$  S SWNTs ( $G_S^-$ ) with components of  $A$  and  $E_1$  symmetry.  $G_M^-$  is generally associated with a broad, asymmetric spectral profile due to phonon-plasmon interactions. However, since there were relatively fewer M CNTs in resonance with the excitation energy in the sample, the plasmon interactions were suppressed, and the  $G_M^-$  could be fitted with a Lorentzian. In addition, two smaller intensity peaks identified with  $E_2$  symmetry were observed at  $1498\text{ cm}^{-1}$  and  $1604\text{ cm}^{-1}$ , as labeled in Fig. 4-1 (b) and (c)(also see Section 2.3).

The relative  $G_M^-$  intensity was observed to decrease as more small  $d_t$  (S) SWNTs are selected by DNA-wrapping, as shown in Fig. 4-1 (b). The intensity of the  $G_M^-$  further decreases as the number of M SWNTs decreases in the fractionated sample. As the samples were wrapped by DNA, the  $E_2$  modes disappeared, suggesting that the isolation achieved by DNA-wrapping quenches such  $E_2$ -type transitions in nanotubes.

For an excitation energy at  $2.19\text{ eV}$  shown in Fig. 4-1(b), a consistent upshift in all the  $G^-$  peak frequencies of about  $6\text{ cm}^{-1}$ , as well as a small downshift of  $2\text{ cm}^{-1}$  in the  $G^+$  peak frequency, relative to the CoMoCAT starting material, were observed for all DNA-wrapped samples. The  $G^-$  upshift could be identified with the changes in the in-plane vibrational force constant, resulting from the DNA-SWNT interactions. An average downshift of the  $G^+$  feature for dried and solution DNA-wrapped SWNTs samples is found to be about  $2\text{ cm}^{-1}$ . This can be attributed to the combination of a small degree of perturbed in-plane vibrations and the charge transfer between electron donating species of DNA molecules and the electron receiving SWNTs. For most laser excitation energies, the experimental results show that the magnitude of this charge transfer effect is slightly larger when the samples are in solution.

## 4.4 $E_{ii}$ Determination

In addition to changes in the vibrational structure, the DNA-wrapping and isolation also provides additional perturbation to the electronic structure of the SWNT. In this section, I will discuss how the environmental perturbation to the electronic structure of a SWNT can be monitored through the changes in the excitonic transition, measured from the Stokes and anti-Stokes Raman spectroscopy, as well as photoluminescence measurements. In sec. 4.4.1, I will review the concept of the resonance profile introduced previously and discuss how  $E_{ii}$  transitions can be determined from the relative Stokes and anti-Stokes intensities of a specific SWNT, excited at several nearly-continuous laser excitation energies. In Sec. 4.4.2, the  $E_{ii}^S$  values determined from PL measurements are discussed, and the results of the resonance profiles as well as the shift in energies relevant to different wrapping agents are discussed in Sec. 4.4.3.

### 4.4.1 $E_{22}^S$ Determined from RRS anti-Stokes to Stokes Intensity Ratio

Stokes (S) and anti-Stokes (AS) RRS measurements were carried out on DNA-SWNT hybrid samples. In most non-resonant Raman scattering events, the relative spectral intensities for the Stokes and anti-Stokes processes reflect the temperature dependence of the relative phonon populations. In 1D systems where the joint density of states (JDOS) have sharp van Hove singularities, the anti-Stokes/Stokes intensity ratio ( $I_{AS}/I_S$ ) is dominated by the resonance process. Values of  $E_{ii}$  were determined from the intersection of the resonance windows for the AS and S scattering processes [101]. Since it is difficult to resolve the exact resonance window profile, the experimental points were fit to a symmetric Lorentzian lineshape. The notation  $\Gamma_r$ , is used to approximate the full width half maximum of the resonance window profiles, and the parameter gives qualitative information about the excited state relaxation rate and the inhomogeneous broadening of the resonance window. The  $\Gamma_r$  for each sample was empirically determined for each RBM feature by plotting the Raman

peak intensities versus  $E_{laser}$  for a few closely spaced  $E_{laser}$  values, and then using a least squares fit routine to determine the widths and peak values of each intensity profile. The values of  $\Gamma_r$  for dried DNA-wrapped nanotubes and for as-produced CoMoCAT SWNT bundles were experimentally determined, respectively, by averaging over Stokes data acquired for five dried S DNA-wrapped nanotubes and for three S as-produced CoMoCAT nanotubes in a bundle. Given the limited number of  $E_{laser}$  values used in this experiment and the weak signal observed for the anti-Stokes Raman process, the widths of the resonance windows for the Stokes and anti-Stokes processes are assumed to be the same. The intensity ratios of the resonance window profiles, constructed using the average  $\Gamma_r$  values for each type of sample with similar wrapping agents were compared to the ratios of the temperature-normalized  $I_{AS}/I_S$  ratios at  $E_{laser}$  to obtain an experimental determination of  $E_{ii}$ , following previously established procedures reported in Fantini et al. [8].

As shown in Fig. 4-2, the width of the resonance window for DNA-wrapped SWNTs is much more narrow compared to SDS-wrapped HiPco SWNTs and bundled SWNTs [8]. The resonance windows for the dried, unfractionated DNA-SWNT hybrids have an average  $\Gamma_r$  value of 15 meV, which is narrow compared to the  $\Gamma_r$  for pristine, as-grown (not wrapped) CoMoCAT nanotubes in bundles ( $\sim 100 \pm 30$  meV) and the  $\Gamma_r$  for SDS-dispersed HiPco nanotubes in solution ( $\sim 60$  meV) [8]. Since the optical signal for DNA-wrapped SWNTs in solution is generally weak, and not enough reliable data was obtained to establish the widths for the resonance profile, it is expected that the width of the resonance window for solution samples are larger, as shown in Fig. 4-2(a). The relatively narrow resonance window for dried DNA-SWNT CoMoCAT hybrids determined here suggests that although a large number of nanotubes were measured under the laser light spot, the individual SWNTs in the dried DNA-SWNT hybrid bundles were well isolated from one another. With a smaller proportion of metallic(M) SWNTs present, the fractionated, (6,5)-enriched DNA-SWNT sample had a slightly smaller  $\Gamma_r$  ( $\sim 13 - 14$  meV) compared to the non-fractionated DNA-SWNT sample.

To facilitate comparison with the work of others, the RRS-determined  $E_{22}^S$  values

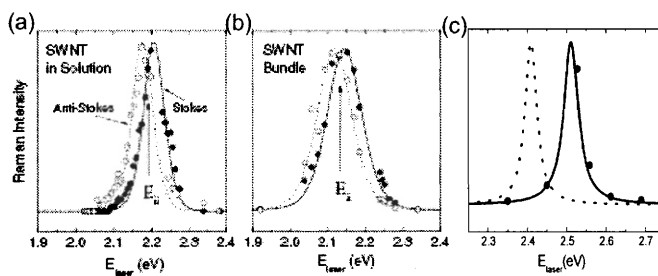


Figure 4-2: (a) shows a resonance window measured for a SDS-wrapped, HiPco SWNT sample dispersed in solution, reported in Fantini et al. [8]. (b) shows a resonance window of bundled HiPco SWNT sample, as previously reported in Fantini et al. [8]. (c) shows the resonance window measured for dried DNA-wrapped CoMoCAT SWNT. The average width of the resonance window for this sample is much smaller compared to that for SDS-wrapped SWNTs in solution or the bundled SWNTs sample. The solid lines here denote the Stokes profiles whereas the dotted lines denote the anti-Stokes profiles for samples in different environments. Since the SWNT here has a different  $(n, m)$  from the one shown in Fantini et al. [8], the transition energy is different. The general trends in the width of the window for the same SWNTs in different environment are the same.

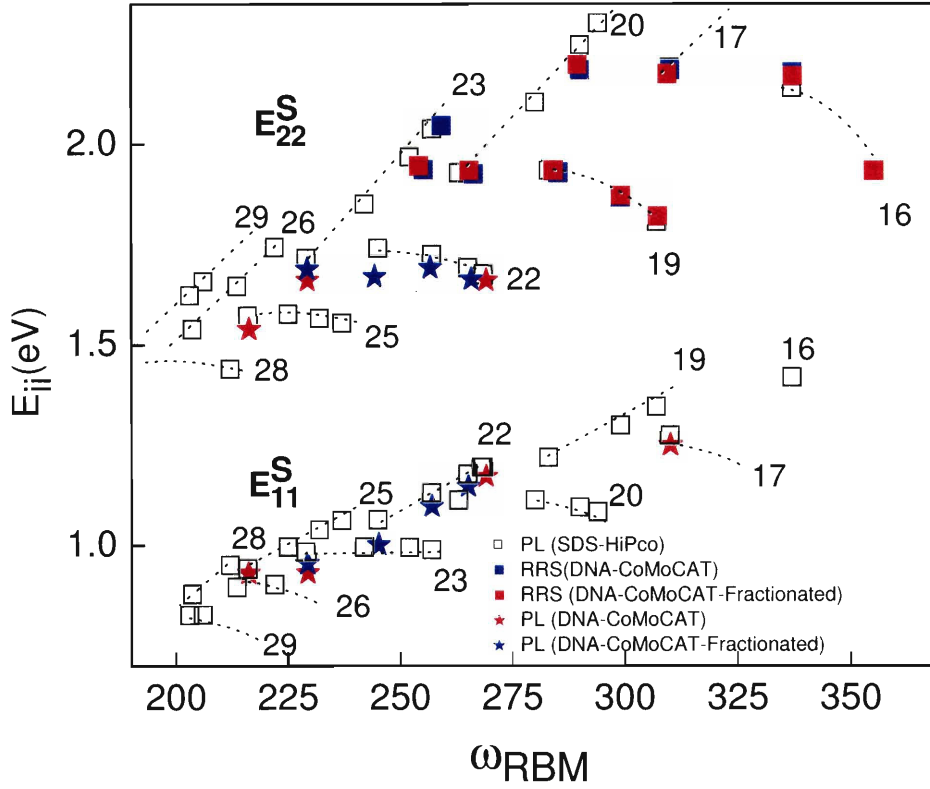


Figure 4-3:  $E_{22}^S$  determined from the temperature-normalized  $I_{AS}/I_S$  ratios of the RRS spectra, plotted against  $\omega_{RBM}$ , showing the  $(2n+m=\text{constant})$  family behavior. Colored data points denote the two DNA-wrapped samples with different S:M ratios (see text), measured with both the RRS and PL techniques. The  $E_{22}^S$  values are determined from RRS and PL measurements, whereas the values of  $E_{11}^S$  values are determined from the PL emission of encapsulated SWNTs.

for S SWNTs were plotted against the radial breathing mode frequencies,  $\omega_{RBM}$ , in Fig. 4-3. The colored square data points denote the two DNA-wrapped SWNT samples with different S to M ratios. To help with the interpretation of the RRS data, the RRS-measured  $E_{22}^S$  values for the DNA-SWNT hybrids are compared to the  $E_{22}^S$  values measured using the PL technique for an SDS dispersed HiPco nanotube sample in solution, for which a previously determined fitting formula

$$\omega_{RBM} = 223.5/d_t + 12.5cm^{-1} \quad (4.1)$$

was employed to extract the corresponding  $\omega_{RBM}$  values [20, 23]. As shown in Fig. 4-3, the RRS measured  $\omega_{RBM}$  values for the DNA-SWNT hybrids in the present work correspond very well with the formula-extracted  $\omega_{RBM}$  for the SDS nanotubes with the same  $(n, m)$  assignment [20]. From the comparison of the  $E_{22}^S$  vs.  $\omega_{RBM}$  values, the DNA-SWNT hybrids were found to follow the  $(2n+m=\text{constant})$  family patterns previously determined from PL measurements of SDS-encapsulated samples [8, 20]. SWNTs in the same  $(2n+m)=\text{constant}$  family are connected by the dotted lines in Fig. 4-3, and the family numbers are shown. The wrapping of SWNTs by DNA was found to shift the second excitonic transition,  $E_{22}^S$ , by 10-80 meV, relative to SDS-isolated HiPco nanotubes with the same  $(n, m)$  assignment. Fractionated and non-fractionated DNA-wrapped samples were found to be shifted by different amounts, in the same direction, either blue or red shifted relative to SDS-encapsulated nanotubes. The average shift over all of the nanotubes measured comes out to be about 30meV to the red. Since the SDS-encapsulated HiPco nanotubes were in solution, whereas the DNA-wrapped nanotubes are dried, the difference in environment could possibly contribute to the difference in the  $E_{22}$  transition energies.

Even though good agreement can be obtained between the  $\omega_{RBM}$  and  $E_{22}^S$  values of SWNTs wrapped by different agents, preliminary analysis of second order phonon features shows that DNA wrapping and the IEC fractionation process decreases the linewidth and the amplitude for many of the second order Raman features, such as the D-band, the M-band, and the combination iTOLA modes. A detailed study of the second order features for DNA-wrapped SWNTs will be presented in later chapters.



#### 4.4.2 Photoluminescence (PL) Measurements

PL measurements were carried out to further investigate the effect of fractionation and DNA-wrapping at the  $E_{11}^S$  band edge. From PL measurements over a wide range of excitation energies, the  $E_{11}^S$  and  $E_{22}^S$  transitions of the DNA-SWNT hybrids were determined. Figure 4-4 shows a section of the two-dimensional contour plot of the excitation vs. emission energies for the unfractionated sample in solution in the near-IR region. PL signals were observed from both fractionated and non-fractionated samples.

The energy positions for all of the  $E_{22}$  and  $E_{11}$  transitions measured for the two samples using Raman and PL are listed in Table 4.1. The excitation and emission energies for these peaks can be correlated with the  $E_{22}^S$  and  $E_{11}^S$  energies previously measured for SDS-encapsulated HiPco nanotubes in solution. For nanotubes whose excitonic transition energies were determined from PL measurements, the values of  $\omega_{RBM}$  can also be determined using Eq. 4.1. Together, the energy pattern for nanotubes of different  $(n, m)$  indices is plotted in Fig. 4-3. The average width of these absorption bands is  $\sim 30$ meV for both the SDS/HiPco and DNA/CoMoCAT tubes.

Figure 4-3 shows the energies of the  $E_{22}^S$  and  $E_{11}^S$  emission peaks for the DNA-SWNT hybrids, together with previously reported values for SDS-dispersed nanotubes [20, 23] and the  $E_{22}^S$  values were measured with RRS. Even though most of the  $E_{ii}^S$  values captured in our PL experiments appear to be red-shifted from the values previously reported for SDS-encapsulated SWNTs with the same  $(n, m)$  assignments (see Table 4.1), these previously reported values can be used as a guide for us to draw similar  $(2n+m=\text{constant})$  family patterns for the PL peaks of DNA-SWNT samples. Even though absorption could occur over a relatively broad range of  $E_{22}^S$  excitation energies, the  $E_{11}^S$  emission energy is clearly associated with the transition occurring at the band edge. Since the emission profile is relatively sharper, the uncertainties in the measured  $E_{11}^S$  values are expected to be smaller [22].

Compared to the values of  $E_{ii}$  obtained for SDS-isolated HiPco nanotubes with the same  $(n, m)$  assignment, most of the PL-determined shifts in the  $E_{22}^S$  and  $E_{11}^S$  values

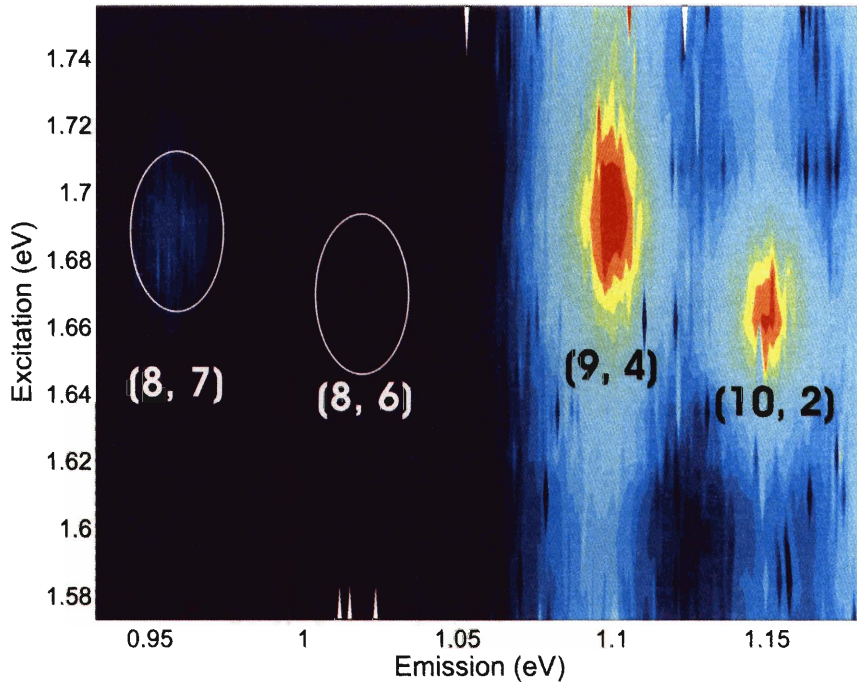


Figure 4-4: A slice of the 2D contour plot of excitation vs. emission energies for a section of the PL data for the unfractionated DNA-SWNT sample where  $E_{22}^S \rightarrow E_{11}^S$  absorption-emission transitions are found. The  $(n, m)$  assignments for these transitions can be identified by comparing their energies with the assigned PL transitions for SDS-dispersed HiPco SWNTs [20]. Note that the  $(8, 6)$  transition is denoted by the white circle. The intensity of the transition is too weak to show up with the intensity scale of the present plot.

for DNA-SWNTs in comparison to the corresponding values for the SDS-wrapped SWNTs are found to be less than 30meV, which is consistent with the shifts observed in the  $E_{22}^S$  values measured using RRS, as mentioned above (see Table 4.1). The shifts in  $E_{ii}$  values between the SDS and DNA wrapped nanotubes measured both in RRS and PL suggest that the amount of perturbation in the nanotube electronic structure is highly dependent on the wrapping agent and nanotube environment. In addition, the difference in  $E_{ii}$  between the fractionated and unfractionated sample suggests that even though the DNA wrapping effectively isolates the nanotube from its environment, the nanotube still interacts with other nanotubes in the same sample, which are also wrapped in DNA. As a result, a slight shift in the excitonic transition energy can be measured for the same  $(n, m)$  nanotubes in a (6,5)-enriched DNA-SWNT sample, relative to the non-fractionated sample.

Figure 4-5 shows a PL 2D contour plot for the fractionated DNA-SWNT sample over a large excitation and emission energy range. The PL emission pattern is concentrated within the range 1.15eV-1.3eV. The brightest emission peak occurs around 1.255eV, which corresponds to the (6, 5) SWNT. Even though the excitation energy does not correspond to  $E_{22}^S$ , the emission peak is observed at an energy close to the previously  $E_{11}^S$  for the (6, 5) SWNT over a wide excitation energy range. The localization of the emission pattern indicates that the fractionation process selects nanotubes within a specific diameter range. The PL peaks for the (9, 7) and (11, 0) SWNTs are observed in the contour plot for the fractionated sample, while the transitions for the corresponding nanotubes do not appear in the PL spectra for the non-fractionated DNA-SWNT hybrids, as shown in Fig. 4-5. This also suggests that the fractionation process eliminated some of the brightly luminescing species and brought out the transitions associated with species that were present in the original sample in small quantities and were too weak to be seen before. A 30meV red shift was observed for the (8, 7) nanotube in the fractionated sample, relative to its non-fractionated counterpart, as shown in Fig. 4-3. This suggests that even though the DNA-wrapping has increased the physical distance between different nanotubes, the interactions between different species in the non-fractionated sample reduce the homogeneity of the

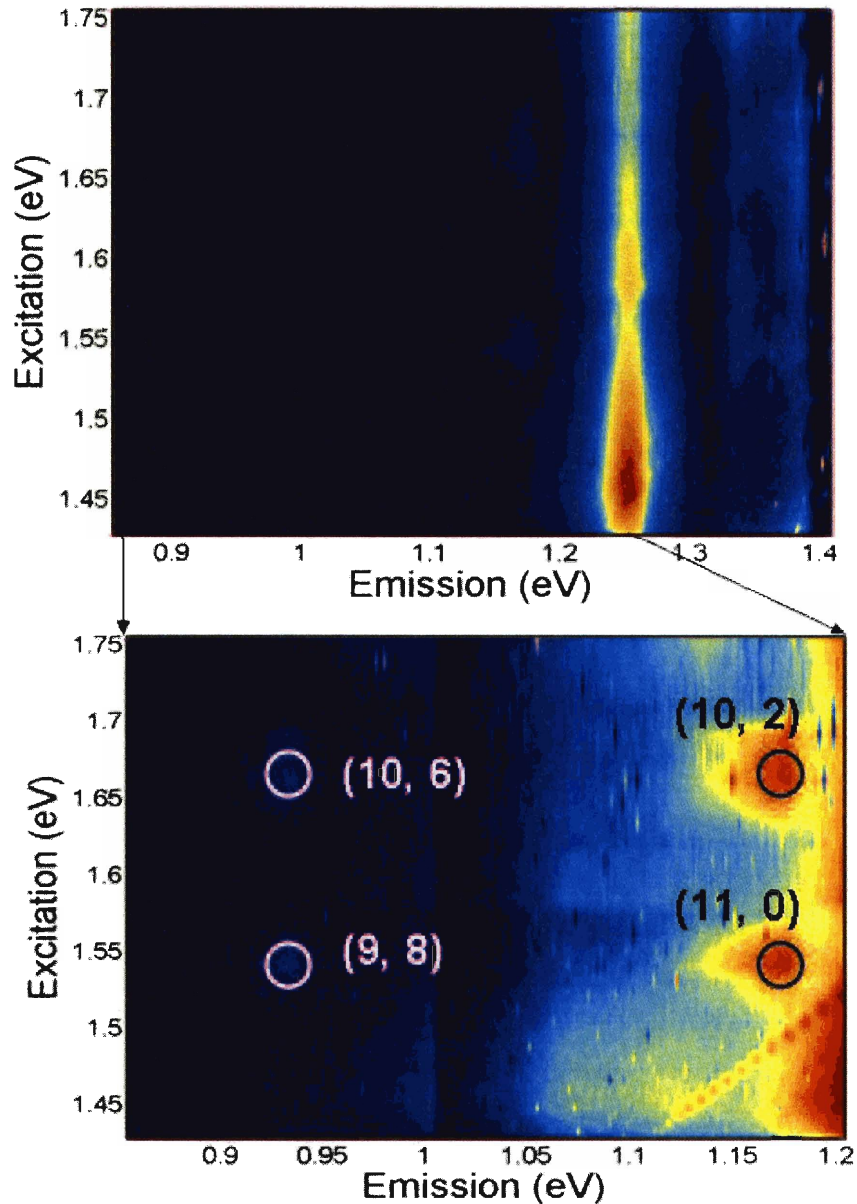


Figure 4-5: The upper Figure shows a 2D contour plot of excitation vs. emission energies for a section of the PL data for the fractionated (6,5)-enriched DNA-SWNT sample. With the dominant emission profile arising from the (6,5) SWNT, the experiment results corroborate the initial sample characterization that suggests (6,5) enrichment for the fractionated sample. Furthermore, PL peaks were observed for  $(n, m)$  species in the lower figure that are not observed in the unfractionated sample. The experimental results shows that the fractionation and enrichment process is indeed a highly  $(n, m)$  specific method for separating a nanotube mixture.

Table 4.1: Transition Energies of DNA-SWNT Hybrids

$(n, m)$	DNA-SWNTs hybrids		Fractionated DNA-SWNTs		SDS-SWNTs [20]	
	$E_{22}^S$ (eV)	$E_{11}^S$ (eV)	$E_{22}^S$ (eV)	$E_{11}^S$ (eV)	$E_{22}^S$ (eV)	$E_{11}^S$ (eV)
(9, 7)			1.541(PL)	0.933(PL)	1.572	0.942
(8, 7)	1.689(PL)	0.956(PL)	1.663(PL)	0.934(PL)	1.714	0.983
(8, 6)	1.671(PL)	1.003(PL)			1.740	1.064
(10, 3)	1.938(RRS)		2.046(RRS)		1.959	
(9, 4)	1.692(PL)	1.102(PL)			1.724	1.130
(11, 1)	2.046(RRS)				2.029	
(7, 6)	1.927(RRS)		1.936(RRS)		1.916	
(10, 2)	1.665(PL)	1.190(PL)			1.691	1.177
(11, 0)			1.663(PL)	1.176(PL)	1.675	1.194
(7, 5)	1.930(RRS)		1.935(RRS)		1.925	
(9, 2)	2.188(RRS)		2.201(RRS)		2.251	
(8, 3)	1.869(RRS)		1.873(RRS)		1.870	
(6, 5)	2.186(RRS)	1.257(PL)	2.186(RRS)	1.252(PL)	2.191	1.274
(9, 1)			1.822(RRS)		1.789	
(6, 4)			2.181(RRS)		2.140	
(7, 2)			1.934(RRS)		1.981	
(5, 4)			2.502(RRS)		2.567	

environment, perturb the nanotube electronic structure, and change the  $E_{ii}$  values by a small amount, as shown in Fig. 4-3. Similar shifts in the  $E_{ii}$  values for nanotubes with the same (n,m) assignments between the dried fractionated and dried non-fractionated samples were also observed in the RRS  $E_{ii}$  determination, as shown in Fig. 4-3.

#### 4.4.3 Learning From Excitonic Transition Energies

The detailed optical studies of excitonic transitions summarized in Fig. 4-3 show that even though the different wrapping agents introduce a small shift both in the exci-

tonic transition energies and RBM frequencies, the shift is not large enough to alter the ( $2n+m=\text{constant}$ ) family pattern nor to interfere with the  $(n, m)$  identifications. Based on the pattern of the specified wrapping agents, one can identify the detailed geometry and  $(n, m)$  assignment of a large number of nanotubes prepared using similar processes. Both RRS and PL studies have confirmed the diameter selective and the  $(n, m)$  enrichment aspect of the DNA-wrapping and the IEC fractionation process. The optical study confirms that one can control the diameter distribution and the fractionation process to produce a sample that is highly enriched in a specific  $(n, m)$  species. The PL study of such an enriched sample has also shown that by having a highly enriched sample, it is possible to see subtle features related to vibrational transitions in the PL spectra for a bulk sample. By taking advantage of the enriched sample, it is possible to study subtle processes that are difficult to investigate at the single nanotube level.

## 4.5 Concluding Remarks: New Opportunities

In this chapter, the environmental effects on the electronic structure of DNA-wrapped carbon nanotubes were investigated in detail using RRS and PL measurements. The detailed optical study shows that DNA-wrapping and IEC fractionation provide a new means for making a sample enriched in a single  $(n, m)$  SWNT that can be used for probing the detailed nanotube 1D electronic structure by isolating the individual nanotubes from inter-tube interactions and through use of the fractionation and  $(6, 5)$  enrichment process. By monitoring the changes in the vibrational spectra using the RRS technique, the DNA-wrapping of CoMoCAT samples were found to be the  $d_t$ -selective. The good isolation achieved by DNA-wrapping and the removal of metallic nanotubes through fractionation also brings out well-defined components of the G-band features, and suppresses the  $E_2$ -symmetry phonon transitions. In general, the RBM frequencies are found to be relatively insensitive to the nanotube environment, even though small variations introduced by fractionation are observed. On the other hand, the electronic structures for carbon nanotubes were found to be very sensitive

to the environment surrounding the nanotube. By comparing the  $(2n+m=\text{constant})$  family pattern for the different DNA-SWNTs and SDS-encapsulated SWNTs samples, it is possible to identify the shift in the excitonic transition energies introduced by the wrapping agents and fractionation process. Even though the different wrapping agents and the fractionation process perturb the electronic structure of the nanotubes and shift the excitonic transition energies, this perturbation does not alter the optical properties of the nanotubes enough to affect the  $(n, m)$  identification based on the  $(2n+m=\text{constant})$  family patterns. In addition, the chromatographic fractionation allows one to produce a sample that is highly enriched in one species. The availability of such an enriched sample introduces the possibility to study subtle optical processes that are originally too weak or time consuming to experimentally measure at the single nanotube level.

# Chapter 5

## Phonon-assisted Excitonic Recombination Channels Observed in the Frequency Domain

### 5.1 Introduction

Photoluminescence spectroscopy (PL) has become an increasingly important technique for the characterization of single-wall carbon nanotubes (SWNT) [20–24]. The ability to probe the electronic structures of a large number of semiconducting SWNTs has made PL a powerful and complementary method to resonance Raman spectroscopy (RRS) for the characterization of SWNTs. In most prior PL studies [20–24], the SWNT samples were dispersed in a surfactant solution, excited with a lamp source, and the PL spectra were recorded over the near and far IR spectral regions. In these studies, the strongly luminescent peaks, associated with the  $i^{\text{th}}$  electronic interband transition,  $E_{ii}$ , for different semiconducting SWNTs are compared using excitation/emission contour maps. Besides the optical characterization of nanotube interband transitions, these PL studies show evidence of phonon-assisted PL processes [102–105], especially when the sample is irradiated by an intense light source. Although evidence for such processes has been mentioned in previous reports, only a



few phonon-assisted processes have been observed, with no clear identification given for their physical origins.

In this chapter, PL measurements were carried out on a (6,5)-enriched DNA-wrapped SWNT sample using laser excitation. PL emission peaks associated with the (6,5) nanotube, photo-excited in an intermediate energy range between the reported  $E_{22}$  and  $E_{11}$  transitions of the (6,5) nanotubes, are analyzed and assigned to a number of phonon-assisted optical absorption and energy relaxation mechanisms. Multiple emission peaks associated with the first and second order phonon scattering processes were observed, and continuous PL emissions associated with thermally excited excitonic processes were also observed. Phonon-assisted processes along the elongated absorption profile, associated with phonons both at the  $\Gamma$  point and near the K point have been identified and studied in detail. A previous theoretical study [106] of the electron-phonon interaction and relaxation rate has interpreted the observed PL features in the (6,5)-enriched sample within the framework of a free carrier band-to-band model, and the interpretation of our results has been influenced by this work. Here, we elaborate on the interpretation of our experimental observations and examine the phonon-assisted processes in terms of excitonic states, using the simplest possible model that considers only the optically active bright excitonic state.

## 5.2 Experimental

To obtain detailed information about phonon-assisted PL processes, it is highly desirable to have one dominant  $(n, m)$  SWNT species in the sample. Since the starting SWNT sample produced from the CoMoCAT process [99] has a narrow diameter distribution as described in chapter 2.3, a (6,5) enriched DNA-wrapped hybrid (DNA-SWNT) sample can be then prepared using ion exchange chromatography [86]. 30  $\mu\text{L}$  of this fractionated stock solution was dropped onto a sapphire substrate one  $\mu\text{L}$  at a time and dried into a thick layer. The sample was excited with nearly continuous excitation energies using a Ti: Sapphire laser, pumped by an  $\text{Ar}^+$  ion laser. The PL emission was collected in a back scattering geometry and was focused onto an InGaAs

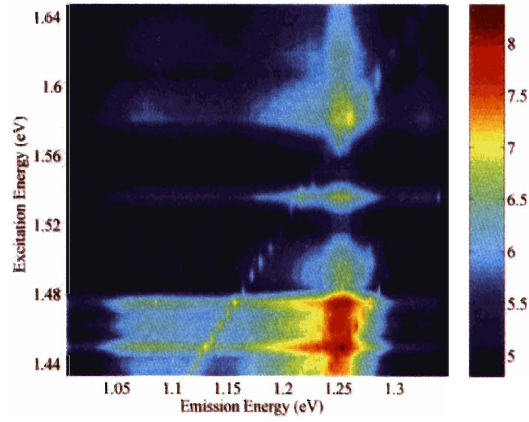
diode array detection system and a Spex 750M Spectrometer through a microscope objective. A linear interpolation routine [107] in MatLab was used to construct the contour plot shown in Fig. 5-1(a).

### 5.3 Phonon-Assisted Processes

Figure 5-1(a) shows a two-dimensional (2D) plot of the excitation vs. emission energies of the (6, 5) enriched, DNA-SWNT sample, where  $E_{ii}^n$  denotes the  $i^{th}$  resonant excitonic subbands of the corresponding bound electron and hole levels, in the  $n^{th}$  exciton state, in which  $n=0$  and  $n=1,2,\dots$  denotes the quantum number for the envelope function of the exciton. In this simplified model, we consider only one excitonic state associated with each quantum number,  $n$ , labeling the excitonic envelope function. The actual exciton symmetry is omitted in this chapter for simplicity. In later chapters, we employ a more detailed formulation of exciton theory that assigns four exciton states to each quantum number  $n$ , one being a bright exciton and optically active, while 3 are dark states and not optically active. Since the experiments carried out in the frequency domain does not give information on the dark state, the simplified model interprets the data in terms of the bright excitonic state only. The PL emission spectra are excited at a series of excitation energies,  $E_{ex}$ , between 1.43 eV-1.64 eV, such that  $E_{11}^0 < E_{ex} < E_{22}^0$  ( $E_{11}^0=1.255$  eV and  $E_{22}^0=2.19$  eV [20, 54]), and the spectra are recorded in Fig. 5-1(a) and are labeled in the schematic diagram as shown in Fig. 5-1(b). The spectral features observed in Fig. 5-1 can be explained by the different phonon-assisted absorption and recombination processes shown in Fig. 5-2(b).

Figure 5-2 describes the different phonon-assisted processes using the diagrams of the exciton center of mass dispersion relation,  $E_{ii}^n(K)$ , where  $K$  denotes the exciton crystal momentum. The solid and open circles denote *real* and *virtual* states, respectively. Optical absorption (excitonic excitation) and emission (radiative recombination) processes occur at  $K=0$  as a result of momentum conservation (with negligible photon momentum). These processes are shown by vertical arrows con-

(a)



(b)

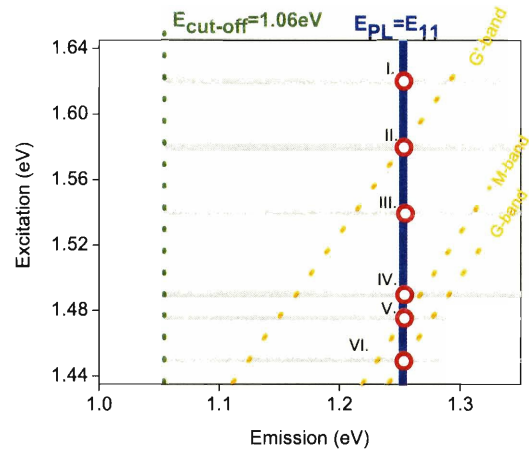


Figure 5-1: (a) A 2D excitation vs. emission contour map for a dried (6,5)-enriched DNA-SWNT sample on a sapphire substrate. The spectral intensity is plotted using the log scale shown on the right. (b) A schematic view of the observed PL transitions. The blue vertical band denotes emission at  $E_{11}^0$ . The horizontal gray bands, denote the nearly-continuous luminescence processes associated with the thermally excited processes in the different phonon branches. The cut-off energy at 1.06 eV is marked in green. Orange dotted lines denote PL emission from resonant Raman scattering processes for G-band, M-band, and G'-band phonons. Strong PL emission spots at  $E_{11}^0 = 1.255$  eV, denoted by the red circles, are associated with one-phonon (VI) and two-phonon (I to V) processes described in Fig. 5-2 (see text).

necting the excited and ground states. All other arrows, not involving the ground state, denote excitons scattered by phonons.

Previous structurally-assigned PL studies [20–24] focused on the SWNT resonant electronic processes described in Fig. 5-2(a), where absorption of the incident photon occurs at the  $E_{22}^0$  band edge, where the photon takes the excited electron to an excitonic state denoted by the transition  $a \rightarrow b$ . The exciton non-radiatively decays to the  $E_{11}^0$  band edge through multiple channels of relaxation ( $b \rightarrow c$ ) and recombines by emitting a photon ( $c \rightarrow a$ ). The red rectangles labeled with “*ex*” and “*em*” correspond, respectively, to the range of PL excitation and emission energy used in the present experiment. With a strongly enriched SWNT sample and an intense light source, we are able to separately identify the different PL emission peaks associated with specific phonon-assisted processes, as shown in Figs. 5-2(b)-(e).

The observed broad range of excitation energies,  $E_{\text{ex}}$ , accompanied by a narrow PL emission window, corresponds to our general understanding of the PL mechanism, in which an exciton can be excited into a number of excited states before the bound electron-hole pair eventually relaxes to the  $E_{11}^0$  band edge and recombines. Along the  $E_{\text{ex}}$  scale for the same band edge emission at 1.255 eV in Fig. 5-1(a), intense PL peaks at several special  $E_{\text{ex}}$  values were observed. These peaks are shown as red circles in Fig. 5-1(b). From previous PL studies [20, 54], these peaks with the same emission energies can all be correlated with the (6, 5) SWNTs, emitting from  $E_{11}^0$ .

### 5.3.1 Multi-Phonon Processes

The PL emission for these special  $E_{\text{ex}}$  values indicated by red open circles in Fig. 5-1(b) is the most intense at the excitonic band edge  $E_{\text{em}} = 1.255$  eV for the (6, 5) SWNT, but nearly continuous emission over the range 1.06 to 1.35 eV is observed for each special  $E_{\text{ex}}$ . These features are labeled by thick, gray horizontal lines numbered from I to VI going across the schematic diagram in Fig. 5-1(b). Each of the special  $E_{\text{ex}}$  values is associated with red circles I through V in Fig. 5-1(b) and can be identified with the two-phonon processes in Fig. 5-2(b).

In the process shown in Fig. 5-1(b), the phonon-assisted absorption can involve

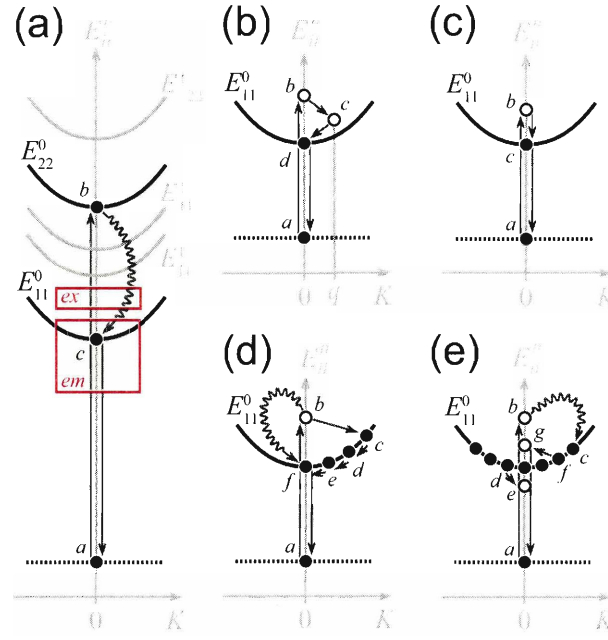


Figure 5-2: Schematic diagrams for the different phonon-assisted processes (see text). (a) The commonly reported [20–24] excitonic recombination mechanism for the (6, 5) nanotube. The process involves excitonic absorption at  $E_{22}^0$  (point b). The excited exciton can relax down to  $E_{11}^0$  (point c) via multiple channels, and can recombine at  $E_{11}^0$ . The red boxes labeled as “ex” and “em”, respectively, denote the range of excitation and emission energies in Fig. 5-1. Since the excitation range is lower than  $E_{22}^0$ , the process shown in (a) is not observed in the present report. (b) Corresponds to the two-phonon assisted processes responsible for transitions I to V shown in Fig. 5-1(b). (c) Corresponds to the one-phonon assisted processes responsible for transition VI shown in Fig. 5-1(b). (d) Corresponds to the nearly continuous vertical transitions at the band edge  $E_{em}^0=1.255$  eV. (e) Corresponds to the thermally-excited processes that are associated with the horizontal streaks shown across the PL map in Fig. 5-1(b).

Table 5.1: Assignments of the strong PL spots in Fig. 5-1 to the different optical phonon branches of the (6, 5) nanotubes

$E_{\text{ex}}(\pm 0.005\text{eV})$ (eV)	Peak Label	Symmetry Point	Phonon Quantity <sup>(a)</sup>	Phonon Branch
1.62	I	$\Gamma$	2	iLO and iTO
1.58	II	K	2	iTO
1.54	III	K	2	iLO and iLA
1.49	IV <sup>(b)</sup>	K	2	iTO and iLA
1.48	V	$\Gamma$	2	oTO
1.45	VI	$\Gamma$	1	iLO and iTO

<sup>(a)</sup>Numbers 1 and 2 refer, respectively, to one and two-phonon processes.

<sup>(b)</sup>Although a contribution from the combination mode iTO+iLA is also expected around IV, the excitation profile is too broad to distinguish the different processes.

the emission of two phonons with opposite momenta,  $-q$  ( $b \rightarrow c$ ) and  $+q$  ( $c \rightarrow d$ ) [see Fig. 5-2(b)]. The two-phonon process brings the exciton to the  $E_{11}^0$  band edge, where recombination occurs. The cross section for this process becomes especially large when the  $E_{\text{ex}}$  values correspond to energies of optical phonon modes that are strongly coupled to the electrons and have a high density of phonon states near the  $\Gamma$  and K points. As a result, the PL emission for the band edge recombination at  $E_{11}^0$  becomes very intense at these special  $E_{\text{ex}}$  values (such that  $E_{\text{ex}} = E_{11}^0 + 2\hbar\omega_q$ ). This two-phonon process gives rise to the intense transitions that are marked by red circles I through V in Fig. 5-1(b) for different combinations of the  $\Gamma$ -point ( $q=0$ ) and K-point ( $q=\Gamma K$ ) optical phonon modes. The specific energies and assignments of these optical phonon branches associated with spots I-V in Fig 5-1(b) are listed in Table 5.1. Furthermore, at  $E_{\text{ex}} = E_{11}^0 + 0.07\text{ eV} = 1.33\text{ eV}$ , a two-RBM phonon process feature in the PL spectra was observed for a similar (6, 5) enriched DNA-SWNT sample in solution, in a different experiment.

The two phonon-assisted processes can also occur in a non-resonant fashion. The series of emissions crossing the map diagonally through spots II and V in Fig. 5-1(b)

arise from similar two-phonon  $M$ -band and  $G'$ -band Raman scattering processes, and the Raman shifts for the two can be roughly calculated to be  $1702 \pm 40\text{cm}^{-1}$  and  $2560 \pm 40\text{cm}^{-1}$ , respectively. Although all SWNTs in the sample contribute to these Raman peaks [orange lines in Fig. 5-1(b)], especially bright PL peaks are found where these phonon series cross the emission profile of a specific  $(n, m)$  SWNT or when the phonon series crosses one of the special  $E_{\text{ex}}$  values. These Raman scattering peaks mostly occur from non-resonant processes when the phonon series do not cross the  $E_{11}^0$  band edge for the specific  $(n, m)$  SWNT in the sample. In the present experiment, with a (6, 5) enriched sample, the  $\sim 45^\circ$  series become especially intense when the series of Raman peaks intersect the strong PL peaks II and V at  $E_{\text{em}} = 1.255\text{eV}$  in Fig. 5-1(b).

A detailed examination of the intersection between the  $\sim 45^\circ$  series and the  $E_{\text{em}} = 1.255\text{eV}$  profile (as shown in Fig. 5-3) shows that these non-resonant Raman series do not intersect the vertical  $E_{\text{em}} = 1.255\text{eV}$  emission profile at the special  $E_{\text{ex}}$  value associated with phonon-assisted transitions. The two dotted lines shown in Fig. 5-3 serve as guides for the eyes to help identifying the offset between the two. The phonon-assisted transition shown is associated with the two D-band phonon-assisted process (or the  $G'$  band). The peak is observed along the band edge emission shown in the vertical dotted line, excited at  $E_{\text{laser}} = 1.58 \pm 0.005\text{eV}$  (See table 5.1). At the same value of  $E_{\text{ex}}$ , the non-resonant Raman transition seems to occur between 1.257 and 1.258eV, which yields a slightly shifted phonon energy. Compared to the phonon energies obtained from the bright one and two phonon-assisted transitions occurring along the band edge emission energy, a similar shift of  $\sim 2\text{-}3\text{meV}$  has been observed for the series of non-resonant Raman processes observed in PL maps, including the Raman transitions for the G-band, M-band, and  $G'$  band. Even though these shifts are much smaller than the experimental resolution of  $\sim 5\text{meV}$ , the consistent shifts are in agreement with the strongly interacting exciton-phonon bound state predicted by theory [108], as discussed in the next section. The calculation of the exciton-phonon bound state have been applied in previous theoretical studies [108] for an one phonon process, and the energy for the exciton-phonon bound state obtained from the

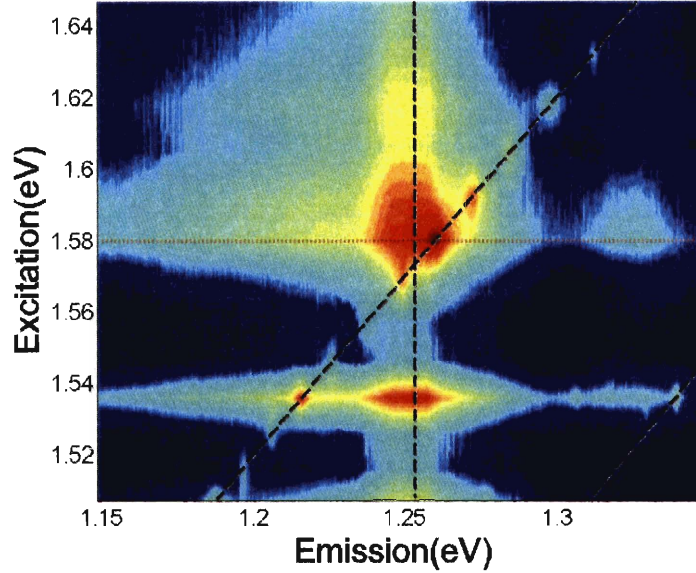


Figure 5-3: A magnified portion of the a 2D excitation vs. emission contour map shown in Fig. 5-1(a), emphasizing the intersection between the non-resonant Raman series and the band edge transitions. The peak shown is associated with the two D-band phonon assisted process (or  $G'$ ) is observed along the band edge emission axis at 1.255eV, as shown with the vertical line, excited at  $E_{laser} = 1.58 \pm 0.005$ eV, as shown with the horizontal brown dotted line. On the other hand, at the same excitation energy, the non-resonant Raman transition seems to occur between 1.257 and 1.258eV, which yields at slightly shifted phonon energy. In general, similar shift of  $\sim 2$ -3meV has been observed for the series of non-resonant Raman processes observed in PL maps.

calculation has been consistent with the energies observed in multiple experimental studies [109,110]. On the other hand, it is not clear whether the similar strongly interacting exciton-phonon bound states can also form for transitions observed in multi-phonon processes such as the  $G'$  (2D), the M-band (2oTO), or the iTOLA (iT0+iLA) mode discussed in this chapter. Further theoretical studies will need to be carried out to understand this process better.

For these phonon series, discrete transitions are observed in Fig. 5-1(a), instead of the expected continuous transitions diagonally crossing the map, because of an



experimental artifact. Since only 24  $E_{\text{ex}}$  laser lines were used and the experimental linewidths of the Raman transitions are small, the Raman transitions only appear on the map where  $E_{\text{ex}}$  is equal to one of the 24  $E_{\text{ex}}$  values. Since the energy spacings between the successive  $E_{\text{ex}}$  are large, the linear extrapolation [107] algorithm yields discrete dots rather than a continuous line in Fig. 5-1(a).

### 5.3.2 One Phonon Process and Phonon Sideband

On the other hand, the mechanism associated with peak VI in Fig. 5-1(b) appearing  $\sim 0.2\text{eV}$  above  $E_{11}^0$  can be explained by a one-phonon process shown in Fig. 5-2(c). In this process, phonon-assisted light absorption ( $a \rightarrow b$ ) excites the exciton to an excited state. The excitation, along with a simultaneous zone-center ( $q=0$ ) phonon emission ( $b \rightarrow c$ ) creates an exciton at the  $E_{11}^0$  band edge, where the ground state exciton radiatively recombines ( $c \rightarrow a$ ). This process gives rise to spot VI in Fig. 5-1 when the  $G$ -band (the  $\Gamma$ -point in-plane optical mode) phonon is emitted. The analogous first-order Raman process that corresponds to the diagonal lines crossing through VI in Fig. 5-1(a) corresponds to the  $G$ -band Raman scattering peak at  $1585 \pm 40\text{cm}^{-1}$ . Along the diagonal emission series, the Raman process is only resonant when  $E_{\text{ex}}$  and  $E_{\text{em}}$  correspond to spot VI and when state “ $c$ ” is resonant with the  $E_{11}^0$  band edge.

In addition to the one or two-phonon mediated processes described above, the position for the  $G$ -band phonon mediated process corresponds to the excitonic phonon sideband predicted by previous *ab initio* calculations [108]. Such phonon sidebands are exciton-phonon bound states resulting from a strong exciton-phonon interaction. In optical processes, a significant fraction of the spectral weight in the optical spectra is predicted to be transferred to a distinct exciton-phonon sideband. The presence of such strong phonon sidebands in optical spectra also confirms the excitonic nature of the resonant optical transitions in SWNTs. The bright  $G$ -band phonon-sideband features ( $0.2\text{eV}$  above the  $E_{11}^0$  band edge) have recently been identified from PL experiments carried out with both HiPco SWNTs [110] and SWNT samples isotopically labeled with  $\text{C}_{13}$  [109]. The width of the so-called phonon sidebands observed

in these PL experiments are usually broad, on the order of 50-80meV. The same transition occurring at roughly 0.19eV has also been identified in photoconductivity spectra [111]. On the other hand, for a highly enriched sample as was used in the present case, it is possible that the strong exciton-phonon interaction is also responsible for the other features associated with the multi-phonon processes observed in our experiment. This strong exciton-phonon interaction might give rise to the small, yet not negligible, upshift in phonon energy for the different phonon-assisted processes described above, but additional calculations will be needed to understand the nature of the exciton-phonon bound state for multi-phonon processes.

Aside from the special optical phonon states, PL emission is observed at the  $E_{11}^0$  band edge when excited with all  $E_{\text{ex}}$  values within the range of this experiment, as denoted by the blue vertical stripe in Fig. 5-1(b). The process is consistent with the general PL mechanism, and the detailed mechanism is depicted by the diagram shown in Fig. 5-2(d). In this case, light absorption ( $a \rightarrow b$ ) is followed by exciton relaxation to the  $E_{11}^0$  band edge through multiple recombination channels ( $b \rightarrow f$ , wavy arrow). The exciton, then radiatively recombines at the  $E_{11}^0$  band edge ( $f \rightarrow a$ ). A possible recombination channel, involving the emission of one optical phonon ( $b \rightarrow c$ ) and several acoustic phonons ( $c \rightarrow d \rightarrow e \rightarrow f$ ), is shown in Fig. 5-2(d). Since there are many possible combinations of the initial excited and intermediate states, the excited emission can be continuous with respect to  $E_{\text{ex}}$ . However, since the phonons involved in such a process do not couple to the electrons as strongly as the optical phonons involved in the processes mentioned in Figs. 5-2(b) and (c), the intensity for such PL emission is weaker.

### 5.3.3 Hot Phonons

In connection with the discrete strong PL peaks I through VI mentioned above, the horizontal streaks of continuous emission can be explained by the mechanism shown in Fig. 5-2(e). In this process, the thermal population of excitons with  $K \neq 0$  near the  $E_{11}^0$  band edge is generated by light absorption ( $a \rightarrow b$ ) and exciton relaxation through multiple recombination channels ( $b \rightarrow c$ , wavy arrow). These  $K \neq 0$  excitons

can radiatively recombine by either emitting a  $q=K$  phonon ( $d \rightarrow e \rightarrow a$ ) or absorbing a  $q=-K$  phonon ( $f \rightarrow g \rightarrow a$ ) to satisfy the momentum conservation constraint. Such processes contribute to the gray horizontal streaks associated with peaks I to VI shown in Fig. 5-1(b). The lower energy ( $E_{em} < E_{11}^0$ ) and higher energy ( $E_{em} > E_{11}^0$ ) sides of these horizontal streaks correspond to phonon emission ( $d \rightarrow e$ ) and phonon absorption ( $f \rightarrow g$ ) processes, respectively. The horizontal streaks only appear for the PL excitation energies near spots I to VI in Fig. 5-1(b). At these special  $E_{ex}$  values, the exciton formation is enhanced by the phonon-assisted absorption processes shown in Figs. 5-2(b) and (c), which increase the  $K \neq 0$  exciton population. The assignment of this relaxation mechanism is supported by the observation that the horizontal emission streaks [I through VI in Fig. 5-1(b)] drop drastically in intensity on the lower energy side of the horizontal streaks at a cut-off energy  $E_{em} = E_{11}^0 - \hbar\omega_{max} = 1.06$  eV, where  $\hbar\omega_{max} = 0.2$  eV is the largest possible first-order phonon energy for SWNTs and graphite [4]. As the series of non-resonant Raman transitions cross these horizontal streaks, the overlapping intensity causes the intersecting point on the PL map to "light up." This enhanced intensity is observed for all of the non-resonant Raman series as they cross all of the horizontal streaks. In this model, low temperature is expected to quench the PL intensity on the higher energy sides of the horizontal streaks, since they are related to the phonon absorption process ( $f \rightarrow g$ ).

### 5.3.4 Fluorescence Resonance Energy Transferring

In a sample containing more than one SWNT species, further insights into the electron relaxation process can be obtained by a careful examination of the PL map, shown in Fig. 5-4. Even though the PL map for the as-prepared DNA-SWNT hybrids in solution also shows nearly-continuous transitions going horizontally across the emission map, the PL intensity breaks up into a set of isolated, individual islands of high PL intensity corresponding to the  $E_{11}^S$  vertical lines for the different  $(n, m)$  SWNT species found in the map. These island streaks resemble the horizontal streaks observed for the (6, 5) enriched sample, insofar as these seemingly isolated transitions are aligned horizontally with the highly absorbing phonon states of the

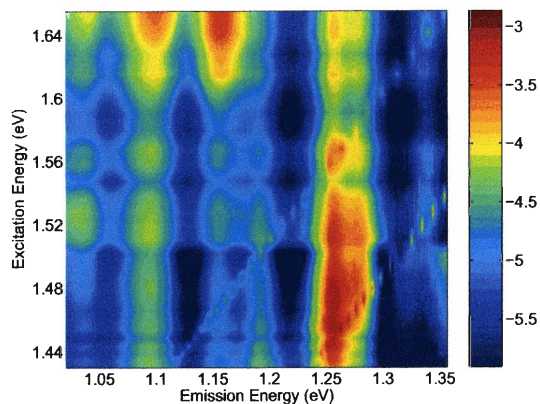


Figure 5-4: A 2D excitation vs. emission contour map for an as-prepared CoMoCAT-based DNA-SWNT sample in solution.

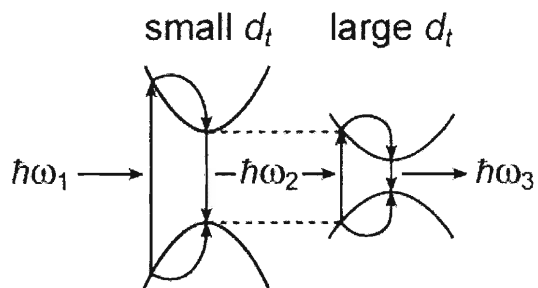


Figure 5-5: A schematic of an additional channel of electron relaxation, in which the photon emitted from electron relaxation of a small diameter SWNT becomes a source of excitation energy for another larger diameter SWNT.

(6, 5) nanotube. These island streaks, however, suggest an energy transferring mechanism between the strongly emitting (6, 5) photons and their subsequent absorption by other nearby nanotube species in the sample, in accordance with the mechanism depicted in Fig. 5-5 [106]. In such a process, the  $E_{PL}$  signal coming from either a band edge emission or a hot luminescence process can be used as a source of excitation for another nearby larger diameter SWNT with a smaller bandgap. In this case, the emission would reach maximal intensity at the band edge of this neighboring tube, forming an “island” in the elongated absorption-emission PL profile of Fig. 5-4. It is possible that a fraction of this energy transfer can be accomplished through the well known fluorescence resonance energy transferring (FRET) mechanism [112], which is a distance-dependent, non-radiative energy transfer process between polar molecules whose dipole orientations are approximately parallel. However, since it is not clear what is the orientation of SWNTs in the DNA-SWNT sample both in solution and on a sapphire substrate, it is not clear whether FRET contributes significantly to the inter-nanotube energy transfer for these types of samples. Further studies on aligned SWNTs could clarify the roles that FRET processes might play.

## 5.4 Summary - Phonon Assisted Processes in 1D Systems

In general, the optical processes discussed in this chapter are difficult to identify separately in solid state systems. For most optical measurements in 3D semiconductors, the phonon and electronic spectra are broad in energy. Moreover, since exciton binding energies of 3D materials are small, detailed phonon-assisted optical processes are not easily observed [113]. On the other hand, by taking advantage of the confinement conditions in low dimensional systems, it is possible to separately identify the different non-radiative processes from optical spectra. Similar phonon-assisted processes have been widely investigated for 0D [114–117] and 2D [117–119] systems, but no systematic studies of such processes have been reported for 1D systems. In this

chapter, a strong phonon-sideband feature is observed somewhat upshifted from the ordinary G-band mode. The observed shift of about 2-3meV is in accordance with the observations by others [109, 110]. The presence of such exciton-phonon bound state can be well-correlated with previous theoretical prediction and confirms the excitonic nature of the optical transitions observed in semiconducting SWNTs. It is possible that such strongly bound state also exists for multi-phonon processes. However, additional calculations and experimental measurements with higher resolution will be needed to understand the nature of the exciton-phonon bound state for multi-phonon processes. Furthermore, we have shown that since SWNT is a strongly confined 1D system, the individual phonon-assisted processes in SWNTs can be well resolved. The PL features can be shown in great detail and over a wide energy range. This is a central finding of this thesis. We have identified and assigned these phonon-assisted excitonic absorption and recombination PL processes observed in the PL spectra for a dried, (6, 5) enriched DNA-SWNT hybrid sample, irradiated by an intense excitation source. Strong-two-phonon transitions associated with phonons near the  $\Gamma$  point or the K point were observed at  $E_{em} = E_{11}^0$  for selected values of  $E_{ex}$ . Intense resonance Raman features were observed at  $E_{em} = E_{11}^0$ , while first- and second-order, resonance Raman transitions were also observed over a wide range of emission energies. We have shown that, by using a SWNT sample highly enriched in a single  $(n, m)$  species, one can probe several different phonon-assisted processes not usually separately identified in 3D solid state systems.

# Chapter 6

## Time Domain Study of Phonon-Assisted Processes in DNA-wrapped SWNTs

### 6.1 Introduction

Understanding the different channels of relaxation for optically excited electrons in one-dimensional systems has played a crucial role in developing potential applications for optoelectronic devices in nanoscale systems. As a prototype 1D material, single walled carbon nanotubes (SWNTs) and their optical properties have been a subject of intense study. Despite recent advances in nanotube photoluminescence spectroscopy [120], the radiative and nonradiative relaxation pathways in SWNTs remain not well understood. In particular, the origin for the reported low photoluminescence(PL) quantum efficiency ( $< 10^{-3}$ ) has been a subject of interest [120, 121].

Most prior time-resolved studies [122–127] have attributed the low PL efficiency to fast nonradiative relaxation processes. Previous pump-probe experiments have also investigated the non-resonant PL dynamics [128], as well as the effects of charge transfer and different nanotube environments [129, 130]. The numerous time-resolved studies have provided important information for understanding the dominant ex-

citonic relaxation mechanisms. However, the detailed mechanism for the roles of phonon-mediated relaxation channels, as well as the role of dark excitonic states remain less well understood. In most prior studies, the relaxation dynamics for optically excited SWNTs has often been found to be dominated by a single exponential or biexponential decay, consisting of a fast, sub-picosecond decay associated with intraband relaxation processes, followed by a slow, 10-180ps decay process associated with a resonantly enhanced recombination process originating from the excitonic band edge [124–126, 129–133]. On some occasions, an intermediate decay time of 2-5ps can be observed in non-degenerate pump-probe studies when the pump energy,  $E_{\text{pump}}$ , is off-set from the probe energy,  $E_{\text{probe}}$ , by an energy of two or more optical phonons [134]. Preliminary explanations have been suggested to account for this observation [134], but no systematic study has yet been carried out to understand such a process in detail.

To further understand this intermediate decay process, a series of pump-probe measurements were carried out on a (6,5) enriched SWNT sample, in which the SWNTs are partially wrapped with single stranded DNA. Since two phonon assisted absorption and relaxation processes have been found to be prominent excitonic processes in DNA-wrapped SWNTs [135], the value of the  $E_{\text{pump}}$  was selected to be very close to  $E_{11}^{0A_2}(6,5) + 2\hbar\omega_D$ , where  $2\hbar\omega_D$  corresponds to the energy for two D-band phonons and  $E_{11}^{0A_2}(6,5)$  denotes the energy for the band edge excitonic state with an envelope function symmetry  $n = 0$  and exciton symmetry  $A_2$  as described in Sec. 4.4 (also called the 1s excitonic state [136]). The pump excitation was especially chosen to enhance the electron-phonon coupling and double resonance process associated with D-band phonons [43].

The optical response is measured in terms of the differential transmission (DT) of the probe beam,  $\Delta T/T_o$ , which corresponds to the fractional difference in transmission intensity between the pump-induced transmission,  $T$ , and the transmission of the reference beam (with no pump fluence),  $T_o$ , where  $\Delta T = T - T_o$ . The DT intensity is negative for photoinduced absorption and is positive for photo-bleaching. From the exponential decay of the DT spectra, multiple processes associated with different



decay timescales can be resolved [137].

With a (6, 5) enriched sample [93] and a carefully selected energy for  $E_{\text{pump}}$ , we examine the physical process governing this well-resolved intermediate decay component in detail. By systematically varying the values of  $E_{\text{probe}}$  to be in and out of resonance with the majority (6, 5) and minority ( $n, m$ ) SWNT species in the sample at different pump fluence levels, we were able to link the intermediate decay time component associated with the (6, 5) SWNT directly to the depletion of the band edge exciton population caused by hot phonon-absorption. Photoinduced absorption processes were also observed when the selected values of  $E_{\text{probe}}$  correspond to off-resonance energies. When taken together, these time-resolved experiments clarify the role of both hot phonon-assisted band edge exciton depletion processes and the Auger process in the relaxation of excitons for individual SWNTs.

## 6.2 Experimental

To obtain detailed information about phonon-mediated PL processes, it is highly desirable to have one dominant ( $n, m$ ) species in the sample. The DNA-wrapped sample was prepared from SWNTs produced by the CoMoCAT process [99]. From the CoMoCAT-based, DNA-wrapped starting material, the (6, 5) enriched sample was then further prepared using ion exchange chromatography [93], and the pump-probe measurements were made in a 400  $\mu\text{L}$  glass spectrophotometer cell with a 1mm optical path.

The optical experiments were carried out at the Tokmakoff lab at MIT. A two-color pump-probe system assembled by Dr. M. Decamp was used for the pump-probe measurements. The pump and the probe pulses were generated using a scheme similar to the one described in a previous report [138]. The pump pulse was generated by the output of a 1.567eV, 1kHz Ti-Sapphire amplifier system, where the energy for the amplified output beam is about 1mJ. The output beam is split for white light generation and the pump pulse. The probe pulse was generated by the signal field of a home-built optical parametric amplifier (OPA) that uses a non-linear  $\text{LiNbO}_3$

crystal as the gain medium. The input seed to the OPA is generated by a white light continuum created by focusing a  $\mu\text{J}$  of energy into a quartz sapphire. The beam splitting of the output beams from the Ti-Sapphire amplifier system was controlled such that the pump pulse is at least 20 times more intense compared to the probe pulse. The OPA tunes the values of the  $E_{\text{probe}}$  between 1.272 to 1.158eV. The pump and probe pulses were both characterized using an optical spectrometer to determine the spectral profile, and the bandwidth for the spectral profiles are on the order of  $100\text{-}400\text{cm}^{-1}$ .

The transmitted probe pulse was collected using a fast silicon photodiode. A third reference beam was collected using a separate detector. However, since the signal to noise ratio for all of the samples were quite high, no shot normalization was carried out. The pump pulse intensity was controlled by a quartz  $\lambda/2$  waveplate and a quartz cube polarizer pair. The pump fluence was estimated by the measured pump power divided by the area of the light spot impinging on the sample, which ranges from 0.5 to  $12\text{ mm}^2$ . The sized of the light spots on the sample for the probe pulses is dependent on the energy for the probe pulses the focusing condition of the collimating optics. The pump pulse was chopped at 500Hz by a mechanical chopper, and a lock-in amplifier collected the modulated probe signal. The temporal and spatial cross-correlation of the pump and the probe pulses gives an instrument resolution of  $\sim 250\text{ fs}$ . The relative timing between the pump and probe pulses was maintained by a computer controlled mechanical delay line. Depending on the signal to noise ratio of a particular scan, the typical data acquisition routines being used in these experiments were carried out in steps of 30 fs with 30-240 accumulation. For detailed measurements of the  $\tau_{\text{slow}}$  component, the data acquisition routines were carried out in steps of 120fs with 60 accumulations.

### 6.3 Results

Figure 6-1 shows a typical differential transmission (DT) spectrum as a function of the pump-probe delay time. The  $E_{\text{pump}} \sim 1.567\text{ eV}$  was chosen to be close to the

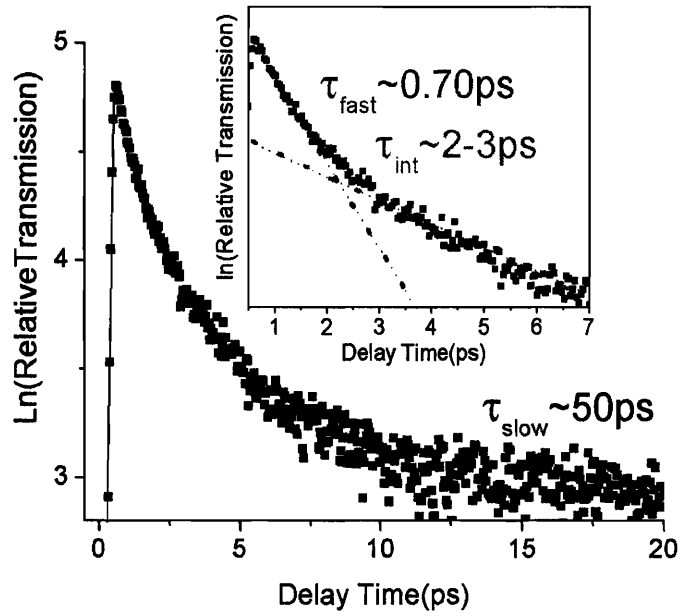


Figure 6-1: A transient spectrum monitoring the DT intensity vs. delay time, for  $E_{\text{probe}} \sim E_{11}^{0A_2}(6,5)$  at 1.252eV, for a (6,5) enriched DNA-wrapped nanotube sample, pumped with  $E_{\text{pump}} \sim 1.567\text{eV}$  (pump fluence level fixed at  $0.1\text{J/m}^2$ ). The  $\Delta T/T_0$  data are plotted on a natural log scale. The inset shows a magnified portion of the plot to show the range of the delay time pertinent to  $\tau_{\text{int}}$  more clearly.

energy of  $E_{11}^{0A_2}(6, 5) + 2\hbar\omega_D$ , while,  $E_{\text{probe}}$ , was set at  $\sim 1.252$  eV, which is close to the previously determined  $E_{11}^{0A_2}(6, 5)$  band edge for DNA-wrapped SWNTs [54, 135]. The quantity  $2\hbar\omega_D$  here denotes the energy of two D-band phonons for SWNTs.

The decay in the DT intensity,  $I(t)$ , as a function of delay time,  $t$ , can be decomposed into a simple multi-exponential decay function

$$I(t) = \sum_i^j A_i e^{-t/\tau_i} \quad (6.1)$$

in which the coefficient  $A_i$  denotes the relative weight of the  $i^{\text{th}}$  process associated with decay time  $\tau_i$ . For the present experiment, a tri-exponential ( $j = 3$ ) decay function can be resolved.

Upon excitation from the pump pulse, numerous excitons are created at an exciton-bound phonon state corresponding to  $E_{\text{pump}}$ . As a result of the special pump energy, a large number of the excitons non-radiatively decay to the band edge  $E_{11}^{0A_2}(6, 5)$ , following the two-phonon emission mechanism discussed in Sec. 6.4.1. The accumulation of the band edge exciton population forms a very fast rise ( $< 200$  fs) in the DT intensity of the dominant (6,5) SWNT.

This filling of the band edge exciton state is followed by a tri-exponential decay process, as shown in Fig. 6-1. The spectral decomposition of the spectrum in Fig. 6-1 shows that the initial 20ps of the decay is dominated by two exponential decay terms in Eq.1, each associated with a decay time of  $\sim 700$ fs ( $\pm 10\%$ ) and  $\sim 2$ -3ps ( $\pm 10\%$ ), respectively, and the two decay terms each account for  $\sim 45\%$  of the initial 20ps of the decay process. In addition, a small amount of the exciton decay process is associated with a slow process with a much longer decay time. The detailed measured fluence dependence of the different decay processes are summarized in Table 6.1.

To gain physical insights into the decay processes, the pump fluence dependence of the individual processes ( $\tau_{\text{fast}}$ ,  $\tau_{\text{int}}$  and  $\tau_{\text{slow}}$ ) was first studied by keeping  $E_{\text{probe}}$  close to  $E_{11}^{0A_2}(6, 5)$ . Figures 6-2(a) and (b) show the decay time evolution for the three processes identified in Fig. 6-1 at different pump fluences <sup>1</sup>. Both  $\tau_{\text{slow}}$  and  $\tau_{\text{int}}$

<sup>1</sup>Since it is difficult to accurately resolve  $\tau_{\text{slow}}$  within the initial decay of 20ps, the pump fluence dependence for  $\tau_{\text{slow}}$  shown in Fig. 6-2(b) was determined in a separate experiment with a longer

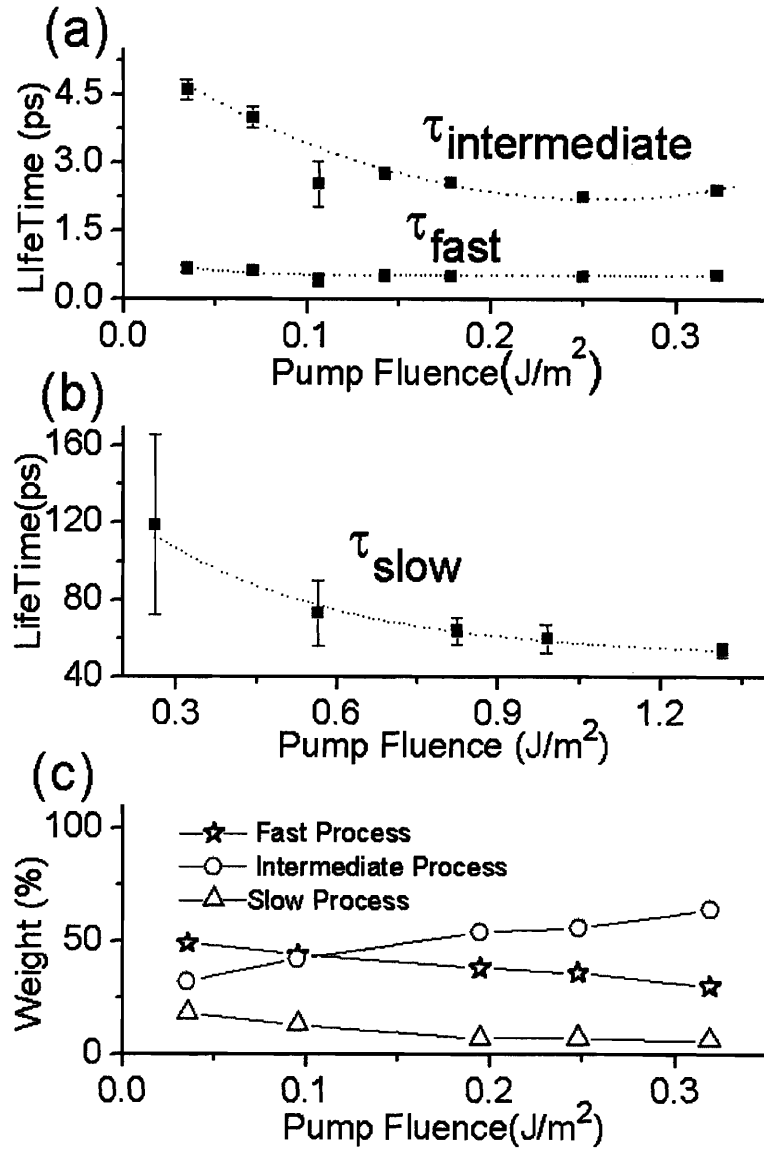


Figure 6-2: Fluence dependence of the different components in the relaxation dynamics for  $E_{probe} \sim 1.252\text{eV}$ . The dotted lines are guides to the eyes. The faster components were measured with higher time resolution (40fs), over 20ps. To determine  $\tau_{slow}$  more accurately, fluence-dependent experiments were carried out over 50ps with lower time resolution (120fs) and a higher pump fluence. Fluence dependence of the (a) two faster components corresponding to intraband processes and the (b) slower component corresponding to the dynamics of the interband recombination. (c) Shows that for the initial 20ps of the decay process, the relative weight for the intermediate process increases with the pump fluence.

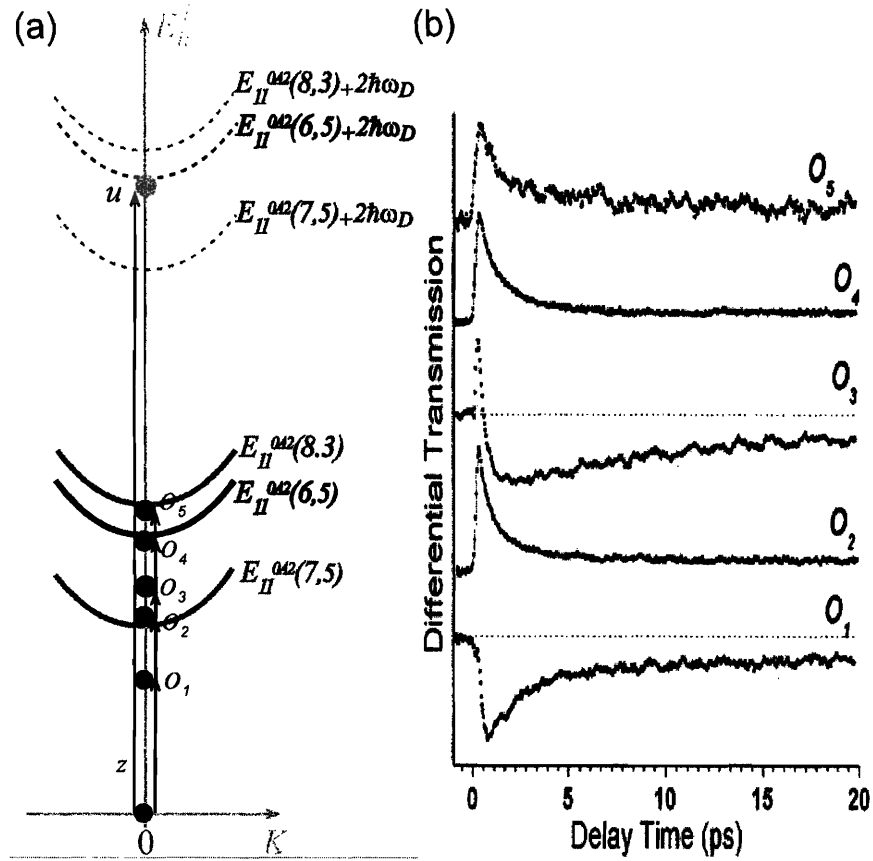


Figure 6-3: The schematic diagram and the respective DT spectra for five different probe energies. (a) A schematic diagram of different values of  $E_{\text{probe}}$  relative to the band edge energies of different nanotubes. The values of  $E_{\text{probe}}$  from  $O_1$  to  $O_5$ , respectively, are 1.158eV, 1.198eV, 1.222eV, 1.252eV, and 1.272eV. (b) DT spectra for different values of  $E_{\text{probe}}$ . Notice that DT changes sign as  $E_{\text{probe}}$  moves in and out of resonance with the (6, 5) and (7, 5) nanotubes. We use the dotted lines as guides for the eyes to mark the zero DT line for the respective DT spectra. The positive DT intensities are normalized to the maximum DT intensity to aid with the lineshape comparison.

show a clear pump fluence dependence, in which the decay processes occur faster with increasing fluence, whereas the fluence dependence for  $\tau_{fast}$  is less clear within the range of available pump fluence levels.

Figure 6-2(c) shows the relative weights in Eq.6.1 for each of the three components during the initial 20ps decay at different levels of pump fluence. The relative weight for  $\tau_{int}$  is found to increase with pump fluence. As discussed in the next section, the result of the increased weight of  $\tau_{int}$  with increasing pump fluence substantiates the proposed interpretation accounting for the intermediate decay time component, to be associated with an additional channel of phonon-mediated excitonic relaxation.

In order to further establish the identifications for the various decay processes, we extend the two-color experiment to excite different  $(n, m)$  SWNTs for which the  $E_{pump}$  does not correspond to specific exciton-phonon states [135]. We scrutinize the relaxation dynamics more generally by monitoring the DT spectral profiles when tuning  $E_{probe}$  between 1.158eV and 1.272eV at four values of  $E_{probe}$  that are different from  $E_{probe} = E_{11}^{0A_2}(6, 5)$ . The positions of the different  $E_{probe}$ , relative to the band edge energies of different  $(n, m)$  species in the sample, correspond to  $O_1$ ,  $O_2$ ,  $O_3$ , and  $O_5$  in the schematic diagram shown in Fig. 6-3(a).

In the cases of  $O_2$  and  $O_5$  in Fig. 6-3(a), the values of  $E_{probe}$  are close to the band edge energies,  $E_{11}^{0A_2}(7, 5)$  and  $E_{11}^{0A_2}(8, 3)$ , for two minority species in the sample. In these cases, even though a photo-bleaching behavior is also observed, the relative weight distributions for the individual decay processes are quite different from the case when  $E_{probe} \sim E_{11}^{0A_2}(6, 5)$  for the majority (6, 5) SWNTs in the sample. Lower overall signal intensities were obtained for the minority (7, 5) and (8, 3) SWNTs. Also, when the values of  $E_{probe}$  are chosen such that  $E_{probe}$  no longer corresponds to any band edge energy, as shown in Fig. 6-3(a), the intensity of the DT spectrum drops to negative values before rising back to equilibrium with time evolution, as shown in the DT spectra corresponding to  $O_1$  and  $O_3$  in Fig. 6-3(b). The negative DT intensity suggests the presence of a photoinduced absorption process. The analysis of the two different rising components, as will be discussed later, indicates that the different

---

scan time.

rise components in  $O_1$  and  $O_3$  mirror the decay times of the (6, 5) SWNTs shown in Fig. 6-1, but include, in addition, contributions from all  $(n, m)$  species in the sample.

## 6.4 Discussion

### 6.4.1 State filling via exciton-phonon interactions

In general, we determine the relative exciton population at the state being probed by  $E_{\text{probe}}$  from the corresponding DT intensity profile. The rising segment in a DT spectrum corresponds to state filling processes and the decaying segments correspond to population depletion processes at an energy corresponding to  $E_{\text{probe}}$ .

Because of the enhanced population of (6, 5) SWNTs in the sample and the corresponding reduced interference from optical signals originating from the other  $(n, m)$  SWNTs in the sample, we first set the  $E_{\text{pump}}$  at  $E_{11}^{0A_2}(6, 5) + 2\hbar\omega_D$  and  $E_{\text{probe}}$  at the  $E_{11}^{0A_2}(6, 5)$  band edge to study the pump-induced excitonic filling and depletion of the  $E_{11}^{0A_2}(6, 5)$  band edge.

As shown in Fig. 6-1, upon excitation by the pump pulse, a sharp initial rise was observed within the first 200fs (see Fig. 6-3(a) trace  $O_4$ ). This sharp rise can be related to rapid state filling processes at the  $E_{11}^{0A_2}(6, 5)$  band edge. In most two-color pump-probe studies where  $E_{\text{pump}} \sim E_{11}^{0A_2}(n, m) + \Delta E$  and  $E_{\text{probe}} \sim E_{11}^{0A_2}(n, m)$ , the  $(n, m)$  band edge state is filled by the  $E_{\text{pump}}$ -created higher energy excitons which lose energy via phonon emission events involving many different phonons [130]. In the present study, the excitons created by  $E_{\text{pump}}$  have an energy such that the energy difference between the pump and the probe pulses corresponds to the energy of two D-band phonons. As a result, a special bandedge filling process occurs, and a large fraction of the excitons created at 1.567eV is expected to efficiently relax non-radiatively to fill the  $E_{11}^{0A_2}(6, 5)$  band edge, following the mechanism described in Fig. 6-4(a) and discussed below.

Upon pump excitation, a large number of excitons are created by the pump pulse at state  $a$  in Fig. 6-4(a), from which the exciton can quickly emit a D-band phonon



with momentum  $q$  to access a dark exciton state with  $0E_\mu$  symmetry [58–60], denoted by  $b$  in Fig. 6-4(a). Here 0 denotes the  $n = 0$  envelope function state and  $E_\mu$  refers to its symmetry type for chiral SWNTs. From  $b$ , which is a real excitonic state, a second D-band phonon with momentum  $-q$  can be emitted to bring the exciton to the  $E_{11}^{0A_2}(6, 5)$  band edge state  $c$ . The mechanisms of the phonon scattering processes are specified by the symmetry of the phonon and the excitonic states [139]. In general, in carbon nanotubes, the A-symmetry  $\Gamma$  point phonons, such as the radial breathing modes and some G-band phonons, as well as the E-symmetry D-band phonons that scatter strongly near the  $K$  point zone boundary are the specific phonons which participate frequently in such scattering events. An A-symmetry  $\Gamma$ -point phonon would scatter an A-symmetry exciton to another A-symmetry excitonic state and an E-symmetry exciton to another E-symmetry excitonic state [139]. Similarly, an E-symmetry phonon would scatter an A-symmetry exciton to an E-symmetry excitonic state and vice versa [139]. Since the D-mode process is strong for E-symmetry phonons associated with electron-phonon coupling near the  $K$  point of the Brillouin zone [140], scattering events involving a D-band phonon will couple an A-symmetry zone center bright exciton band edge state and an E-symmetry dark exciton state.

Because of the high efficiency for the two optical phonon scattering processes described above (in Fig. 6-4(a)), we expect this mechanism to contribute significantly to the initial rise in the  $E_{11}^{0A_2}(6, 5)$  band edge exciton population, and a large number of D-band phonons will thus be created. Such hot phonons exist as quantized lattice vibrations associated with individual SWNTs in addition to the ordinary phonon distribution expected at a given temperature. Therefore, we use the name "hot" phonons to describe these non-equilibrium D-band phonons. These lattice vibrations can be transferred from one SWNT to a neighboring SWNT in solution via collisions.

Even though the energy chosen for  $E_{\text{pump}}$  in this experiment is close to the position of the previously reported  $E_{11}^{1A_1}(6, 5)$  (or 2p exciton) level [136] for (6, 5) SWNTs, we do not populate the  $E_{11}^{1A_1}(6, 5)$  level significantly by the intense pump pulse because the optical symmetry selection rule dictates that such a state cannot be accessed with a one photon excitation process [136]. Thus, the resulting pump-induced decay

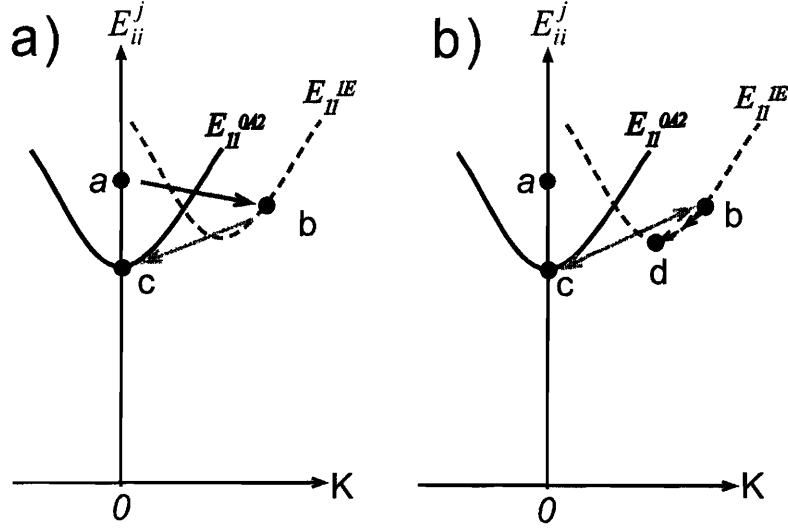


Figure 6-4: (a) A schematic diagram of relaxation from  $a$  to the  $0A_2$  excitonic state  $c$  by emitting two D-band phonons (see text). The black arrow denotes a fast phonon emission process originating from an exciton-bound phonon state, whereas the gray arrow denotes a slow process originating from a real excitonic state. (b) A schematic diagram of a scenario in which the band edge exciton population can be depleted via phonon-absorption. The pump-probe experiment was carried out for the case where  $E_{\text{probe}} = E_{11}^{0A_2}(6, 5)$ , corresponding to point  $c$ .

dynamics, should not be much affected by the  $E_{11}^{1A_1}(6, 5)$  state. Similarly, the lower lying dark excitons with  $1A_1$  symmetry are not optically active. However, this lower lying dark state can be populated by the higher energy band edge excitons from the bright state via phonon scattering.

### 6.4.2 Different Decay Channels

After the rapid initial state filling process is completed within the first 200fs, the DT spectra in Fig. 6-1 show three different components of exponential decay that correspond to three channels of band edge exciton depletion, with decay time  $\tau_{fast}$ ,  $\tau_{int}$ ,

and  $\tau_{slow}$ . The fast and the slow processes have been described and studied in detail in previous reports [127, 132, 141], while the detailed mechanism of the intermediate process has not yet been clarified.

The fast, sub-picosecond decay term observed in Fig. 6-1 has long been correlated with bandedge decay processes that are electronic in origin [123, 126, 132, 142]. Even though multiple mechanisms have been suggested to account for this process [123, 126, 142], prior pump-probe studies have shown that such a fast initial decay process is usually dominated by Auger processes [123, 125], whereby the collision of two excitons results in the annihilation of one of the excitons, which non-radiatively recombines. The excess of energy from the recombination event is simultaneously transferred to the other participating exciton, resulting in either the dissociation of that exciton into a free electron and hole in the continuum, or the promotion of the exciton into an  $E_{22}^{0A_2}(6, 5)$  state, as described in Ma *et al.* [125]. The free electron and hole in the continuum will further recombine via multiple recombination pathways without contributing to the DT spectra observed at  $E_{probe}$ .

The slow decay component has a decay timescale,  $\tau_{slow} \sim 50ps$ , and this range of long decay times is consistent with previously identified long decay time mechanisms that involves non-radiative processes occurring from the band edge, such as exciton phonon scattering, exciton-defect interactions, and relaxation by inter-tube energy transfer by colliding with metallic nanotubes [126, 143]. Since the quantum yield for the radiative recombination process for SWNTs is low ( $10^{-4}$ ), [121] a large fraction of the recombination events are expected to occur non-radiatively. Thus, we assign the slow decay component to contain contributions from both a weak radiative recombination process and a dominant phonon-assisted relaxation process, in which the band edge excitons are slowly depleted via phonon scattering. One such possible non-radiative decay scenario shows the decay of the  $E_{11}^{0A_2}$  band edge excitons via exciton-phonon interactions which slowly decay into a defect-induced trap state below the  $E_{11}^{0A_2}(6, 5)$  band edge [139].

The intermediate decay process is a more subtle process that only appears under special circumstances when the energy difference between the pump and the probe

pulses corresponds to two or more phonon energies, and where the phonon in question is associated with a highly efficient phonon-assisted process. The specificity observed in this study suggests that the  $\tau_{int}$  decay process can be attributed to the depletion of the band edge exciton population via the absorption of a specific phonon by the (6, 5) SWNT. In general, one expects such a phonon-absorption process to be in equilibrium with the corresponding phonon-emission events. Such a process would keep the band edge population at a steady state. However, it is possible, after a phonon-absorption event, that the exciton in question relaxes via other channels without returning to the band edge, resulting in a net decrease in the  $E_{11}^{0A_2}(6, 5)$  band edge exciton population. One of such scenario is described in Fig. 6-4(b).

As described earlier, during the initial exciton population build-up, a large number of hot D-band phonons are created by two phonon emission processes  $a \rightarrow b$  and  $b \rightarrow c$ , as shown in Fig. 6-4(a). Given the large abundance of hot D-band phonons for the first ps after the onset of the pump pulse, it is possible for the exciton at the band edge  $c$  to absorb a D-band phonon and return to  $b$ , thus establishing a quasi-equilibrium  $c \rightleftharpoons b$ , as shown in Fig. 6-4(b). However, a small fraction of the excitons at  $b$ , instead of following the  $b \rightarrow c$  path and returning to the  $E_{11}^{0A_2}(6, 5)$  band edge, can scatter with one or more small energy phonons and can leak into the band edge of the dark exciton state  $d$ . As shown in Fig. 6-4(b), once the exciton at  $b$  relaxes to  $d$ , the exciton is likely to be trapped and never return to  $c$ . Under this scenario, the "leaking" process will drive the equilibrium  $c \rightleftharpoons b$  to the right and remove excitons from  $E_{11}^{0A_2}(6, 5)$  permanently at the rate of the leaking process. Under this scenario, the  $\tau_{int}$  reflects the rate at which the exciton at  $b$  leaks into  $d$  in Fig. 6-4(b).

With the above described relaxation channels in mind, we can now understand the effects observed with increasing pump fluence. With increasing pump fluence, more excitons can be created at 1.567eV, and these excitons subsequently decay via hot phonon generation. As a result, the rate of hot D-band phonon generation increases with pump fluence, which increases the relative rate of exciton depletion at the  $E_{11}^{0A_2}(6, 5)$  band edge via the phonon absorption process described above and in Fig. 6-4(b). This mechanism is consistent with the observed pump fluence dependence

for  $\tau_{int}$ . On the other hand, with increasing fluence, even though more excitons are being generated at the  $E_{11}^{0A_2}(6,5)$  band edge and the rate of the electronic relaxation channel (such as Auger process) is more sensitive to the band edge exciton population, little fluence dependence is expected for  $\tau_{fast}$ . Our data show a possible small fluence dependence for  $\tau_{fast}$  at low fluence levels in Fig. 6-2(a), but the relative weight of  $\tau_{fast}$  decreases with increasing fluence. However, the detailed fluence dependence is not well resolved, in our data, for such a short decay time.

In general, we would expect a similar phonon-mediated state filling process and depletion process to be present for all  $(n, m)$  species, provided that  $E_{pump} \sim E_{11}^{0A_2}(n, m) + 2\hbar\omega_D$  for the particular  $(n, m)$  SWNT. However, out of the few prior pump-probe studies that have met these special energy requirements [134], the measurements were carried out on samples with many  $(n, m)$  species. For such samples, only a small percentage of the SWNTs in the sample could experience the special hot phonon process observed here for the (6, 5) SWNT and therefore the observed effects were smaller in magnitude than what is seen in our study.

In the present study, the hot phonon processes becomes a very pronounced feature in the resulting DT spectra for a (6, 5) enriched SWNT sample. The increasing importance of the  $\tau_{int}$  process with increasing fluence shown in Fig. 6-2(c) substantiates the phonon-assisted nature of this process. Note that Fig. 6-2(c) shows the relative weights of the three processes within the first 20ps. Even though the fast Auger process might be speeding up with increasing fluence, its relative weight appears to be decreasing while the weight of the clearly resolved intermediate process is increasing faster.

### 6.4.3 Probing The Minority Species In The Sample

The energy specificity for the hot phonon creation and absorption processes that lead to filling and depletion of the band edge exciton population can be demonstrated by the measurements carried out when  $E_{probe}$  is tuned to the  $E_{11}^{0A_2}$  band edge of the minority species in the sample, as represented by transitions  $O_2$ , and  $O_5$  in the schematic energy level diagram shown in Fig. 6-3(a).

Table 6.1: Decay times and weights of the individual processes measured at different probe energies

$E_{\text{probe}}$	Pump Fluence	$\tau_{\text{fast}}$ (fs)	$A_{\text{fast}}$ (%)	$\tau_{\text{int.}}$ (ps)	$A_{\text{int.}}$ (%)	$\tau_{\text{slow}}$ (ps)	$A_{\text{slow}}$ (%)
1.272eV	0.3J/m <sup>2</sup>	~900	~70	several ps	traces	~30	~30
1.252eV	0.1J/m <sup>2</sup>	~700	~45	3.0	~45	~50	~10
1.198eV	0.3J/m <sup>2</sup>	~800	~90	N/A	N/A	~40	~10

For  $O_2$  and  $O_5$  in Fig. 6-3(a), the values of  $E_{\text{probe}}$  are close to the  $E_{11}^{0A_2}(7, 5)$  and  $E_{11}^{0A_2}(8, 3)$  band edge states, respectively. As mentioned before, even though similar positive spectral profiles as Fig. 6-1 are observed, the different relative weight distributions for the individual decay processes suggest a difference in the intrinsic decay mechanisms involved.

Table 6.1 shows the normalized weights of the different processes in the DT spectra measured with different values of  $E_{\text{probe}}$ . With  $E_{11}^{0A_2}(6, 5) + 2\hbar\omega_D$ , three separate components can be resolved, as described in Fig. 6-1. When  $E_{\text{probe}}$  is close to  $E_{11}^{0A_2}(7, 5)$ , (trace  $O_2$  in Fig. 6-3(b)), a biexponential decay dynamics is observed, and the decay timescales for the two components are consistent with previous pump-probe studies [124–127, 129–133, 141].  $E_{\text{pump}}$  (1.567eV) here still corresponds to  $E_{11}^{0A_2}(7, 5) + \Delta E$ , but  $\Delta E$  no longer corresponds to  $2\hbar\omega_D$ . Thus for the (7, 5) SWNT, the DT decay does not get a significant contribution from the hot D-band phonon absorption process. The absence of the intermediate decay time component in this case supports the aforementioned identification that correlates  $\tau_{\text{int}}$  with the depopulation of  $E_{11}^{0A_2}$  band edge states via hot phonon-absorption processes.

When  $E_{\text{probe}}$  was tuned to ~1.272eV (trace  $O_5$  in Fig. 6-3(b)), which is close to  $E_{11}^{0A_2}(8, 3)$ , it is possible to decompose the exponential decay into three components, but the intermediate component is not clearly resolved. If instead, the transient spectrum is characterized by a biexponential decay, we find that both  $\tau_{\text{slow}}$  and  $\tau_{\text{fast}}$  are shifted slightly compared to the values obtained from the (6, 5) and (7, 5) SWNTs using three exponentials in the fit. Since the value of  $E_{11}^{0A_2}(8, 3) + 2\hbar\omega_D$

is  $\sim 34$  meV higher than  $E_{\text{pump}} = 1.56$  eV, it is possible for the tail of the  $E_{\text{pump}}$  to access  $E_{11}^{0A_2}(8, 3) + 2\hbar\omega_D$  and to trigger similar filling and depletion processes for the  $E_{11}^{0A_2}(8, 3)$  band edge exciton population by the hot phonon generation and absorption process described above. These hot phonons can thus contribute weakly to the DT decay and give rise to a small  $\tau_{\text{int}}$  component. As a result,  $\tau_{\text{int}}$  can then contribute weakly to the DT decay and can get partially mixed with  $\tau_{\text{fast}}$  and  $\tau_{\text{slow}}$ . The unresolved  $\tau_{\text{int}}$  component makes  $\tau_{\text{fast}}$  a little longer, and  $\tau_{\text{slow}}$  a little shorter. Since the  $E_{11}^{0A_2}(8, 3)$  energy is very close to that for  $E_{11}^{0A_2}(6, 5)$ , and since the (8, 3) SWNT is a minority species in the sample, it is possible that we are also observing optical responses from some (6, 5) SWNTs in the sample. A sample strongly enriched in (8, 3) nanotubes will be needed to distinguish the different contributions to the relaxation process more clearly.

The detailed similarities and differences of the relaxation processes for the (6, 5), (7, 5) and (8, 3) SWNTs thus provide a better understanding of the relaxation process for the (6, 5) SWNTs. Since the (7, 5) and (8, 3) SWNTs are minority species in the sample, the pump-probe signals corresponding to these tubes are weaker than the signal correlated with the (6, 5) SWNTs, and, therefore, a higher pump fluence has to be used to induce a noticeable optical response. Even though the experiments are here carried out under different pump fluence conditions, it is still possible to qualitatively compare the overall weights of the intermediate decay components for these different SWNTs and to reach some conclusions about the physical mechanisms that are involved.

#### 6.4.4 Photoinduced Absorption Processes

The negative DT intensities for the cases of  $O_1$  and  $O_3$  in Fig. 6-3(b) suggest the presence of photoinduced absorption processes. Similar absorption processes have been observed in prior pump-probe studies [127, 128, 130, 144, 145] under different experimental conditions, and multiple physical models have been proposed to account for these observations. [127, 130, 141, 144]

In the present experiment, since the values of  $E_{\text{probe}}$  remain in the IR range,

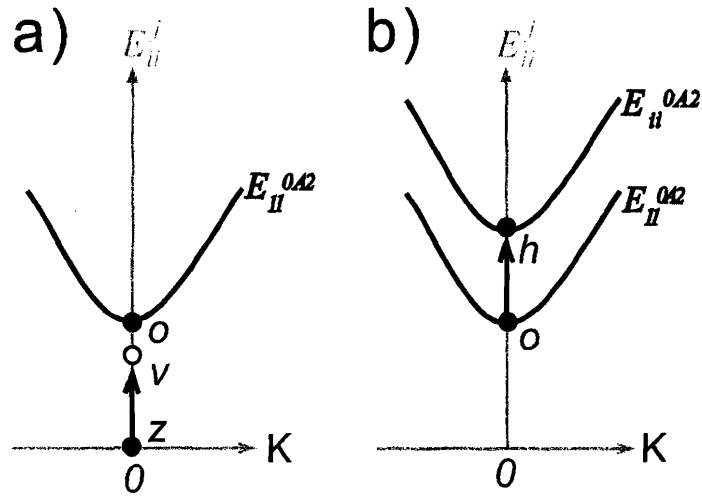


Figure 6-5: Schematic diagram of two possible scenarios for the photoinduced absorption process when  $E_{\text{probe}}$  does not correspond to excitonic band edge energies. (a) A band edge exciton at  $o$  is created by exciting an electron from the ground state  $z$  to a virtual state  $v$  and then combining with an optical phonon to reach state  $o$ . (b) A band edge exciton at  $o$  can combine with a photon and access a higher continuum mobile band state at  $E_{ii}^{0A2}$ , denoted by  $h$ .



it is not likely that the observed photoinduced absorption is introduced by plasmon interactions as described in a previous report [128]. As shown in Fig. 6-3, the values of  $E_{\text{probe}}$  at  $O_1$  and  $O_3$  do not have the right energies for exciton creation for the SWNTs contained in our sample, as shown in Fig. 6-5(a) for  $z$  to  $v$ . The photons from the  $E_{\text{probe}}$  pulse in this case can in fact be absorbed by the  $E_{11}^{0A_2}$  band edge excitons at  $o$  (which had been previously created by the pump pulse) by promoting these band edge excitons into either another higher band edge state or to a continuum mobile band state, denoted by  $E_{ii}^{0A_2}$  in Fig. 6-5(b). The pump-induced absorption events will decrease the corresponding optical transmission at the corresponding  $E_{\text{probe}}$  and will result in negative DT intensities. According to this model, the probe beam probes the population of the band edge states of the SWNTs in the sample indirectly through photoinduced absorption, and the timescale for the exponential rise should closely mirror the timescale for the exponential decay in the cases of photo-bleaching, when a specific band edge state is being probed. A detailed description of such photoinduced absorption processes is described in Korovyanko et al. [127]. According to this model [127], the photon energy of the  $E_{\text{probe}}$  is absorbed by a band edge exciton with no physical mechanism to discriminate one  $(n, m)$  SWNT from another. As a result, all of the  $(n, m)$  species in the sample should contribute to the photoinduced absorption process. However, since our sample is enriched in (6, 5) SWNTs, the DT spectra should mostly mirror the changes in the  $E_{11}^{0A_2}$  (6, 5) band edge population with time evolution.

For the cases of  $O_1$  and  $O_3$  in Fig. 6-3(b), the rising part of the spectra can be decomposed into multiple components using an expression similar to Eq. 6.1.

$$I(t) = \sum_i^j A_i (1 - e^{-t/\tau_i}) \quad (6.2)$$

Spectral analysis shows that the observed exponential rise in  $O_1$  and  $O_3$  can both be fit with a biexponential function with two ranges of rise time:  $\tau_{\text{rise1}} \sim 1\text{-}9\text{ps}$  and  $\tau_{\text{rise2}} \sim 30\text{-}100\text{ps}$ . The two ranges of rise times in the photoinduced absorption spectra are qualitatively consistent with the ranges of  $\tau_{\text{int}}$  and  $\tau_{\text{slow}}$ , observed in the cases when  $E_{\text{probe}} \sim E_{11}^{0A_2}$  (6, 5) and where photo-bleaching occurs. The experimental observations

in Fig. 6-3(b) substantiate the model proposed above.

In the case of  $E_{\text{probe}} \sim 1.222$  eV, shown as  $O_3$  in Fig. 6-3, the DT spectrum also shows a small positive peak before the intensity drops below zero. The small positive DT peak is attributed to the tail of the broad probe beam that excites excitons directly into the  $E_{11}^{0A_2}(7, 5)$  bandedge state at 1.19 eV, which is  $\sim 30$  meV from the  $E_{\text{probe}}$  centered energy, resulting in a small amount of photo-bleaching for short times after the pump is fired.

## 6.5 Summary

In this study, by using a carefully chosen  $E_{\text{pump}}$  that corresponds to  $E_{11}^{0A_2}(6, 5) + 2\hbar\omega_D$  and probing at  $E_{11}^{0A_2}(6, 5)$ , an intermediate decay time component that is associated with the hot D-band phonon-absorption relaxation process is studied in detail. By systematically varying the pump fluence and by varying the values of  $E_{\text{probe}}$  to be in and out of resonance with the minority  $(n, m)$  SWNT species in the sample, we looked into the detailed similarities and differences in the different channels of band edge exciton population decay mechanisms for the  $(6, 5)$ ,  $(7, 5)$  and  $(8, 3)$  SWNTs. The detailed information thus obtained from the experiment clarifies the role of hot phonon absorption and emission processes, as well as the Auger process, in the filling and depletion of band edge exciton populations for individual SWNTs.

# Chapter 7

## Finite length effects in DNA-wrapped carbon nanotubes

### 7.1 Introduction

Length separation of single walled nanotubes (SWNTs) has been one of the on-going themes in carbon nanotube research. The availability of SWNT samples with a precisely controlled geometry not only facilitates device engineering, but the availability of SWNT samples with average lengths much shorter than the wavelength of light also allows one to study the consequences of finite-size effects associated with the broken translation symmetry.

Extensive theoretical studies have been carried out to understand finite-length effects on the electronic and optical properties of carbon nanotubes [30, 146, 147]. In particular, the vibrational structure in the extended intermediate frequency modes (IFM) region between  $600\text{cm}^{-1}$  and  $1500\text{cm}^{-1}$  have been of special interest to nanotube scientists, since the broken translational symmetry in short SWNTs has been predicted to increase the ordinarily low Raman cross section for the many modes occurring in the extended IFM region. Previous resonance Raman studies have investigated the IFM features to determine their detailed  $(n, m)$  dependence [15, 53, 148, 149]. Fantini *et al.* [15] have explained the origin of the IFM features in the  $600\text{cm}^{-1}$  and  $1100\text{cm}^{-1}$  range, as well as their very special excitation energy,  $E_{laser}$ , depen-

dence, on the basis of the combination of zone-folded optical and acoustic branches from 2D graphite. Further resonance Raman studies have extended the model to relate the detailed spectral dispersion behavior to different SWNT diameter and metallicity-dependent resonant  $E_{ii}$  transitions [149]. On the other hand, no systematic study has been carried out to explore the IFM intensity dependence on nanotube length.

Recent developments in the size exclusion chromatography (SEC) technique [19] have enabled length separation of DNA-wrapped SWNTs into suspensions of isolated SWNTs samples with quite uniform length distributions, as described in Section 3.3. In this chapter, a systematic resonance Raman study is presented on such DNA-wrapped CoMoCAT SWNT samples with different average lengths, produced using SEC separation. The effects of the reduced translational symmetry and of the increased cap contribution to the vibrational structure of short SWNTs has been studied in detail. As the average nanotube length decreases, many of the features in the extended IFM region show an increased Raman cross section. The extent of the Raman intensity increase is found to be dependent on the physical origin of the IFM features. The IFM features originating from the scattering processes around the high-symmetry  $\Gamma$  point are found to have little or no dependence on the nanotube length, while the other features increase in relative intensity with decreasing nanotube length. The increased contribution of the end-cap in short nanotubes also yields enhanced intensities for several fullerene features. In addition, the changes in the D-band intensity are examined as the nanotubes become shorter, in the context of the crystalline size effect, when compared to the D-band intensity behavior in nano-graphite samples.

## 7.2 Experimental

Three samples of DNA-wrapped CoMoCAT SWNTs with average lengths of  $\sim 50\text{nm}$ ,  $\sim 70\text{nm}$ , and  $\sim 100\text{nm}$  were prepared using SEC, following procedures established in a previous report [19, 93](as described in Section 3.3). The average length for each

of the fractions has been previously determined by AFM measurements [19], and the variation in the nanotube length distribution is estimated to be about 10%. [19] The dried samples used for optical characterization were prepared from the fractionated liquid samples by dropping 15 $\mu$ Ls of the same stock solution onto a piece of sapphire substrate, one  $\mu$ L at a time. The drops were allowed to dry into a thick layer. Resonance Raman spectroscopic measurements were carried out using a home-built micro-Raman system [150], and the spectra taken at the same laser excitation energy are later normalized with respect to their G-band intensities. The laser excitation energies,  $E_{laser}$ , were generated from a Kr<sup>+</sup> ion laser and a dye laser (using DCM and Rhodamine 6G dyes), pumped by an Ar<sup>+</sup> ion laser. A thermoelectrically-cooled Si CCD detector was used in conjunction with the dye laser. The laser power level on the sample was kept below 0.45 mW through a 50 $\times$  microscope objective in the backscattering geometry to prevent overheating the sample.

### 7.3 Enhanced Features in the Extended IFM Region

For the first experiment, the value of  $E_{laser}$ , was chosen at 647nm (1.92eV) because this  $E_{laser}$  is resonant with the (7, 5) SWNT, which is one of the dominant majority species in the samples used in these experiment. The DNA-wrapped, as-grown SWNT sample (labeled as-grown) was used as a standard. Since the as-grown sample had not gone through the SEC fractionation process, the length distribution of the sample resembles that of typical CoMoCAT starting materials. The spectra for all of the samples are normalized with respect to their G-band intensities, and only one dominant radial breathing mode (RBM) associated with the (7, 5) SWNTs could be observed in Fig. 7-1 (a) for all of the samples. This particular choice of  $E_{laser}$  allows one to focus on one particular ( $n, m$ ) species and to emphasize the effects of nanotube length on the Raman spectra.

The spectral features shown in Fig. 7-1 (a) associated with the 100nm samples

closely resemble the features of the as-grown sample, in which the average lengths are estimated to be at least several hundred nanometers. As the average length of the SWNT samples decreases, more features appear in the Raman spectra in the extended IFM region, and higher relative intensities (relative to the G-band) are observed for these IFM features, as shown in the inset of Fig. 7-1 (a).

To show the effects of nanotube length on the Raman intensities more clearly, I plot in Fig. 7-1(b) the difference spectra between the SEC treated SWNT samples and the as-grown sample. Since previous AFM characterization [151] has shown the DNA coverage to be approximately the same for the as-grown sample as compared to the SEC fractionated samples, the difference spectra allow one to eliminate any weak spectral features in the extended IFM region arising from the DNA-wrapping agent.

In general, the Raman intensities in the IFM region are very low because many of the Raman-active IFM features correspond to long wavelength vibrations along the axial direction. [30] Since nanotube-shortening lowers the translational symmetry, more Raman-active features in this spectral region are expected to appear [30]. The reduced symmetry for short nanotubes has also activated several otherwise silent IR-active modes in the resonance Raman spectra, even though the  $sp^2$ -bonded carbon network is unlikely to support any static dipole. Several IR-active modes were consistently observed for all of the short DNA-wrapped SWNT samples at all values of  $E_{laser}$ . The frequencies for these observed IR modes are consistent with the ones reported previously [152] (See Fig. 7-3).

### 7.3.1 Length-Dependent Intensity Evolution

Most of the IFM frequencies observed are consistent with the mode frequencies reported in previous Raman studies [15, 149, 153], with a small frequency variation due to curvature effects. On the other hand, different length dependencies of the mode intensity are observed for different extended IFM features. These differences in the pattern of intensity evolution with length are associated with the different physical origins of the observed IFM features, as explained below.

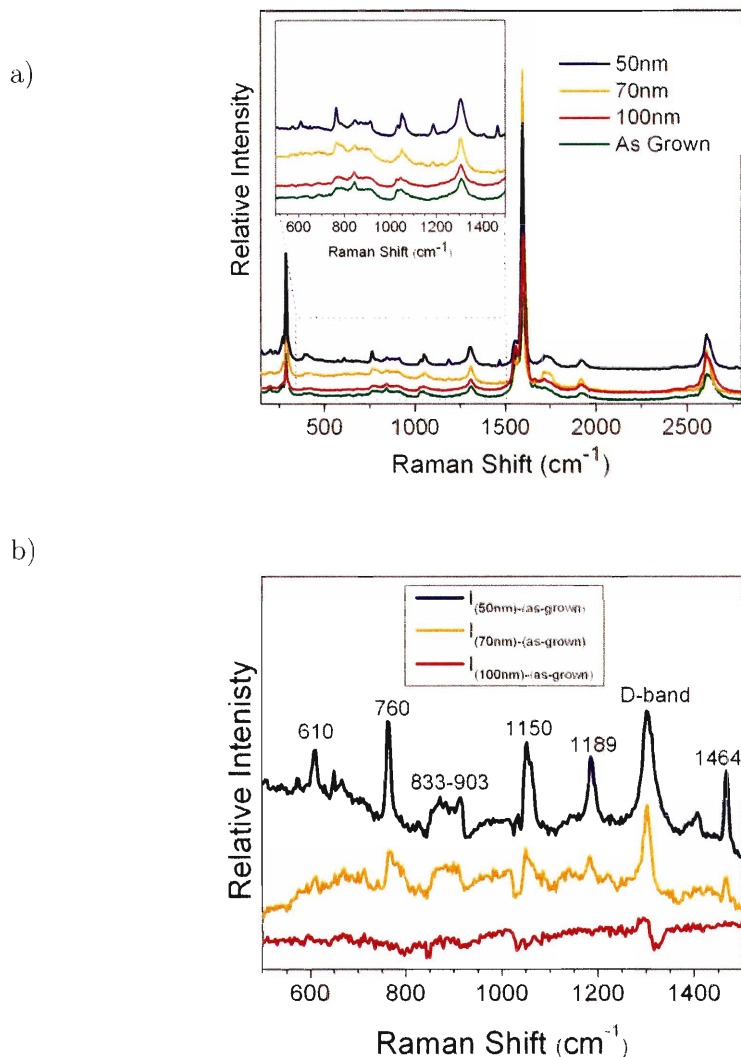


Figure 7-1: a) A comparison of the resonance Raman spectra for an ensemble of an as-grown SWNT sample wrapped with DNA (not fractionated) and three SWNT samples with an average length of 50nm, 70nm, and 100nm, respectively, that had been fractionated using SEC [19]. The spectra were taken with an excitation energy 647nm(1.92eV), which is highly in resonance with the (7, 5) SWNT species. The inset to the figure shows a magnified portion of the modes in the extended IFM region. All four spectra are normalized with respect to their G-band intensities. b) Shows the difference spectra between the finite-length sample and the as-grown sample in the extended IFM region between 600 – 1500 $cm^{-1}$ . The spectra in (b) were obtained by subtracting the spectra of the DNA-wrapped, as-grown sample from the spectra from each of the three short samples.

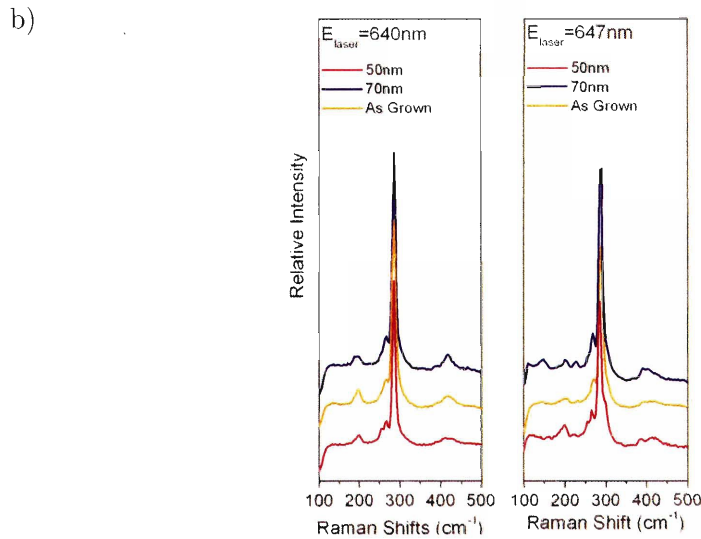
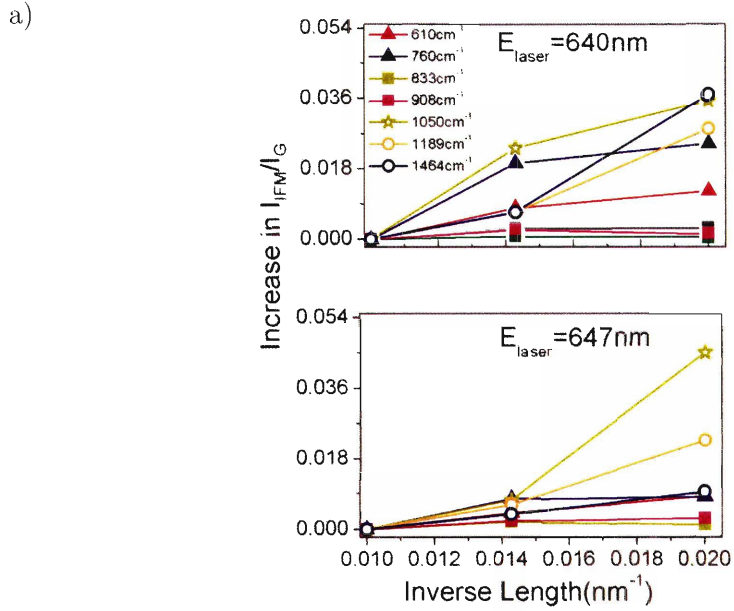


Figure 7-2: (a) Evolution of the *increase* in the relative IFM intensity, with respect to the G-band intensity ( $I_{IFM}/I_G$ ), as the average length of the nanotubes decreases from 100nm to 50nm. The relative intensities are plotted as a function of inverse nanotube length for  $E_{laser} = 647\text{nm}$  (1.92eV) and  $E_{laser} = 640\text{nm}$  (1.93eV) (b) A comparison of RBM features excited by 640nm and 647nm. The dominant RBM feature at  $297\text{cm}^{-1}$  corresponds to the (7, 5) SWNTs. The normalization of the spectra are to the G-band intensity in all cases.



### Transitions Originating from $\Gamma$ Point Processes

Figure 7-2(a) shows the detailed evolution of the relative IFM intensities at two values of  $E_{laser}$ , both in resonance with the (7, 5) SWNT. For both laser excitation energies, Fig. 7-2(b) shows that the (7, 5) SWNTs are the only dominant resonant species. However, since the 647nm (1.92eV) laser excitation is slightly off resonance, no clear pattern could be observed in the case of 647nm (1.92eV) when we compare the pattern of IFM intensity evolution with respect to nanotube length. As we tuned the  $E_{laser}$  slightly to 640nm (1.93eV) to get closer to  $E_{ii}$  for the (7, 5) SWNTs, the observed  $I_{IFM}/I_G$  are higher in general, and a clear pattern for IFM intensity evolution with respect to nanotube length can be identified.

For the two non-dispersive Raman features at  $840\text{cm}^{-1}$  and  $908\text{cm}^{-1}$  originating from the  $\Gamma$  point, their intensities do not increase significantly with decreasing length. This result showing little length dependence for these features is consistent with the identification of these peaks with the out-of-plane, totally symmetric vibrations. These two modes consistently show a weak or no dependence on length for all values of the  $E_{laser}$ .

### Transitions Originating from near- $M$ Point Processes

For Raman features observed around  $610\text{cm}^{-1}$  and  $760\text{cm}^{-1}$  in Fig. 7-1 (a), the relative Raman intensity goes through a rapid increase initially when the average length changes from 100nm to 70nm. The rates of the intensity increases for these two peaks slowed down when the average nanotube length changed from 70nm to 50nm. These features are identified with the near-M-point symmetry-breaking process (labeled in solid triangles), following previous IFM studies [15, 149, 153]. The two features are assigned to transitions with a similar origin due to the similar length-dependent pattern in their relative intensities. At the given values of  $E_{laser}$ , it is also possible to assign  $760\text{cm}^{-1}$  to a different combination IFM mode, as the counterpart for the observed  $908\text{cm}^{-1}$  combination IFM mode, which is identified as the linear combinations of optical and acoustic phonons. However, compared to the  $908\text{cm}^{-1}$  mode, the

$760\text{cm}^{-1}$  mode has a significantly larger intensity increase with respect to decreasing average nanotube length. It is possible that the sharp  $760\text{cm}^{-1}$  feature arises from a combination of the two mechanisms, and the near M-point process is responsible for the large intensity increase with decreasing average nanotube length.

### IR Active Modes and Fullerenic Features

The third class of IFM intensity behavior, as labeled by open circles in Fig. 7-2, is associated with the IR active and fullerenic modes in nanotubes. Raman features around  $1462\text{cm}^{-1}$ ,  $1402\text{cm}^{-1}$ , and  $1189\text{cm}^{-1}$  are consistently observed in the extended IFM spectra. These frequencies correspond to the vibrational energy of previously observed IR features, and they are likely to be activated by the reduced translational symmetry in short SWNTs.

On the other hand, the mode occurring at  $1462\text{cm}^{-1}$  has been a prominent vibrational feature observed in fullerenic structures, such as  $\text{C}_{60}$  and  $\text{C}_{70}$  [27]. The  $1402\text{cm}^{-1}$ , and  $1189\text{cm}^{-1}$  modes have also been observed in a few reports on fullerene studies. Since the short nanotube samples contain a larger sample fraction of hemispherical end caps, which have a similar geometric and vibrational structure as fullerenes, the large increase in the IFM intensity observed at these IFM frequencies can probably be partially attributed to contributions from the end caps, in addition to the activated IR modes. The intensities for these features increase rapidly as the average nanotube length changes from 100nm to 50nm.

The  $\sim 1050\text{cm}^{-1}$  Raman feature observed in all of the samples for all  $E_{laser}$  values, has been previously identified to be a signature of an asymmetric C-O stretch vibration originating from gas adsorption [153]. This explanation is consistent with the occurrence of the  $1050\text{cm}^{-1}$  peak observed for our sample, since the same transition has been reported to occur at the same frequency for all of the samples regardless of the diameter distributions for SWNTs synthesized using different methods [153]. For all values of the  $E_{laser}$  shown in Fig. 7-2, the relative intensity for this feature (shown in open stars) shows a large increase with decreasing nanotube length.

### (n,m) Dependence

As mentioned in Chapter 2, the IFM features have been previously observed as sharp peaks associated with the combination of optical and acoustic-like modes, exhibiting a step-like dispersive frequency behavior with changing  $E_{laser}$ . [15, 149] For larger diameter SWNTs produced using the laser ablation method, only  $\text{mod}(2n + m, 3) = 1$  carbon nanotubes with low chiral angle are observed. In the model proposed in this work [?, 149], additional selection rules for the electron-phonon scattering process allow only the contribution of low chiral angle semiconducting nanotubes belonging to the class  $\mathcal{S}_1$  ( $\text{mod}(2n + m, 3) = 1$ ) to the IFM spectra. [15, 149]

To further investigate the IFM structures of different (n,m) species, the samples were studied at three additional values of  $E_{laser}$  around the same energy region, as shown in Fig. 7-3. For these values of  $E_{laser}$ , several species of similar diameter semiconducting SWNTs with different chiral angles contribute significantly to each of the spectra. The common IFM features as well as their possible assignments are summarized in Table 7.1. For  $E_{laser} = 679\text{nm}$  (1.83eV), in which (8, 3) is emphasized, the detailed pattern of intensity evolution does not seem to change very much, but the frequencies of the peak appear to be highly dependent on the resonant (n, m) species. Compared to (7, 5) SWNT, (8, 3) SWNTs belongs to the same ( $2n + m = 19$ ) family (or ( $\text{mod}(2n + m, 3) = 1$ )), and the two species have similar diameter. However, the (7, 5) SWNT is a near armchair SWNT with  $\theta \sim 23.2$ , whereas (8, 3) has  $\theta \sim 15.3$ . The small difference in diameter and chiral angle reflect on the extended IFM spectra shown in Fig. 7-3(a) and (b). The starkly different spectra between Fig. 7-3(a) and (b) confirms that the scattering process associated with the combination modes in the extended IFM region is indeed very sensitive to the detailed nanotube geometric structure. The large intensity obtained in the extended IFM region for both (7, 5) and (8, 3) also suggests that it is possible for SWNTs with higher chiral angles to exhibit significant IFM intensities. Even though this observation is different from the model established using bundled HiPco and laser ablation SWNTs [15, 149], large IFM intensities have been previously reported for higher chiral angle SWNTs in the

case of isolated SWNTs grown on charged poly-silicon substrate [53]. It is possible that for SWNTs wrapped with DNA, similar charge transfer effects between DNA and SWNT (as described in Chapter 4) provides additional perturbation to the system and enhances the originally weak IFM features for SWNTs with high chiral angles. Further studies will be required to establish a better model to understand the large IFM intensities observed in these SWNTs with larger chiral angles.

For  $E_{laser} = 620\text{nm}$ , the (8, 3) SWNTs go out of resonance while (11, 0) SWNTs, zigzag SWNT, come into resonance. In this case, (7, 5) SWNTs remain in resonance. Assuming that Fig. 7-3(c) can be decomposed into the summation of contributions from (7, 5) and (11, 0) SWNTs, the effect of chirality can be identified by comparing Figs. 7-3(b) and (c). As more  $(n, m)$  species contribute to the spectra, more Raman features appear in the spectra. Even though the relative intensities for the near- $\Gamma$  point features around  $840\text{cm}^{-1}$  do not change much with nanotube length, they do appear much broader in the Raman spectra, as seen in Fig. 7-3 (c), because more components associated with the different resonant  $(n, m)$  species are observed at the corresponding  $E_{laser}$ .

Several extended IFM features observed in this experiment are not discussed in detail in terms of the length dependence of their intensities because the modes are either too weak or they don't appear consistently from one spectrum to another. One such peak is the feature at  $1401\text{cm}^{-1}$ , which is observed in many of the spectra and is identified to be either an IR-active mode, a fullerenic vibration, or a combination of both. However, since the peak is very weak, it is difficult to determine the length-dependent behavior. Similarly, the mode around  $1234\text{cm}^{-1}$  has been consistently observed when  $E_{laser} = 640\text{nm}$  (and sometimes when  $E_{laser} = 620\text{nm}$ ). Even though the vibrational frequency is close to one of the previously-reported IR modes, additional systematic studies will be needed to investigate and to explain both the specificity of this mode to the  $E_{laser}$  and the large intensity increase with decreasing nanotube length.

Even though pure poly(GT) DNA does give rise to weak vibrational features in the IFM region, the resonantly enhanced Raman modes arising from carbon nanotubes

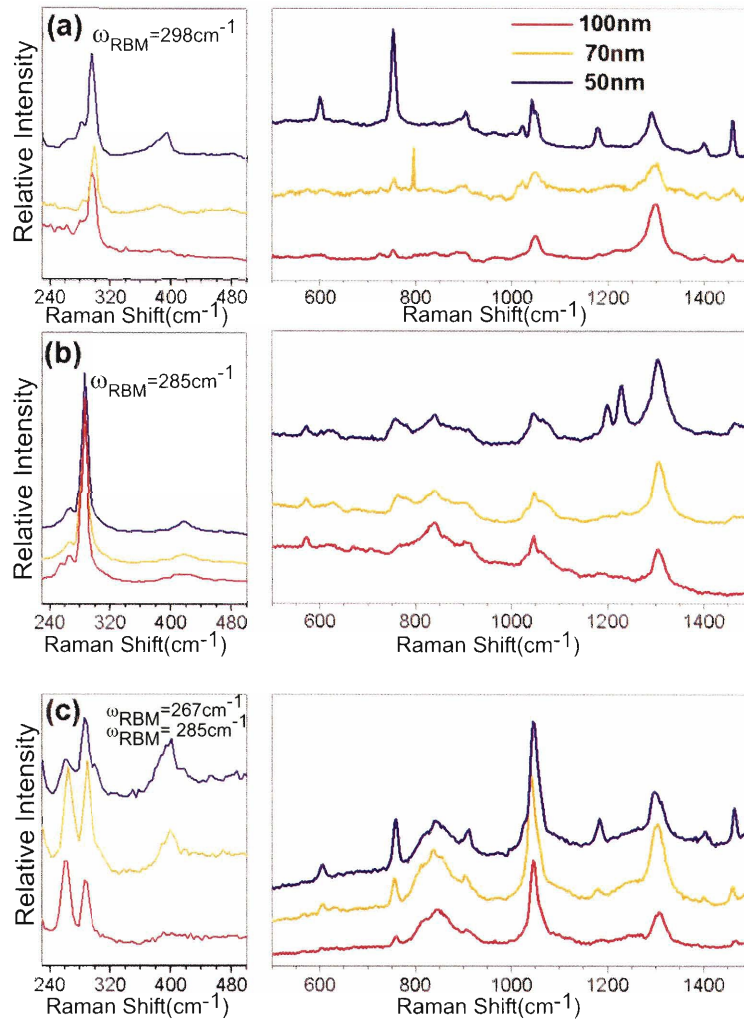


Figure 7-3: Resonance Raman spectra in the RBM and IFM regions of DNA-wrapped SWNTs with different average lengths, taken at (a)  $E_{laser} = 679\text{nm}$  ( $1.83\text{eV}$ ), (b)  $E_{laser} = 640\text{nm}$  ( $1.97\text{eV}$ ), and (c)  $E_{laser} = 620\text{nm}$  ( $2.00\text{eV}$ ). The values of  $E_{laser}$ , respectively, emphasize (a) (8, 3) (b) (7, 5), and (c) (7, 5) and (11, 1) semiconducting SWNT species.

Table 7.1: IFM frequencies and their assignments

$E_{laser}$ in $\lambda(\text{nm})$	Shift ( $\text{cm}^{-1}$ )	assignment [15, 152]	intensity behavior
647,679,620	610	oTO/ITA near M point	increases with decreasing length
647,679,640,620	761	oTO/iTA near M point	increases with decreasing length
647,679,640,620	761	combination IFM	increases with decreasing length
647,679,640,620	833-842	oTO	small length dependence
647,679,640,620	908	Combination IFM Mode	small length dependence
647,679,640,620	1045-1051	C-O vibration	increases with decreasing length
647,679,640,620	1189	IR and fullerenic modes	increases with decreasing length
640,620	1234	possibly IR mode	increases with decreasing length
647,679,640,620	1291-1309	D-band	increases with decreasing length
647,679,640,620	1403-1410	IR and fullerenic modes	increases with decreasing length
647,679,640,620	1460	IR and fullerenic modes	increases with decreasing length

are roughly one order of magnitude higher in intensity in the IFM region. Therefore, the observed increasing IFM intensities most likely arise from the intrinsic property of the carbon nanotubes instead of from DNA. As the value of  $E_{laser}$  becomes greater than 2.2eV, a broad fluorescence background arising from DNA can be observed for all of the samples. This fluorescence background interferes with the intensity analysis of the lower intensity IFM features discussed in this section. As a result, the detailed intensity analysis for this energy region is not presented.

## 7.4 Other Crystalline Size Effects in Carbon Nanotubes

### 7.4.1 D-band intensities and End-Cap Effects

An important consequence of the reduced aspect ratio in SWNTs is the reduced crystalline graphitic sidewall length and the resulting increased fractional contribution of the end-caps to the nanotube structure. This structural characteristic is reflected

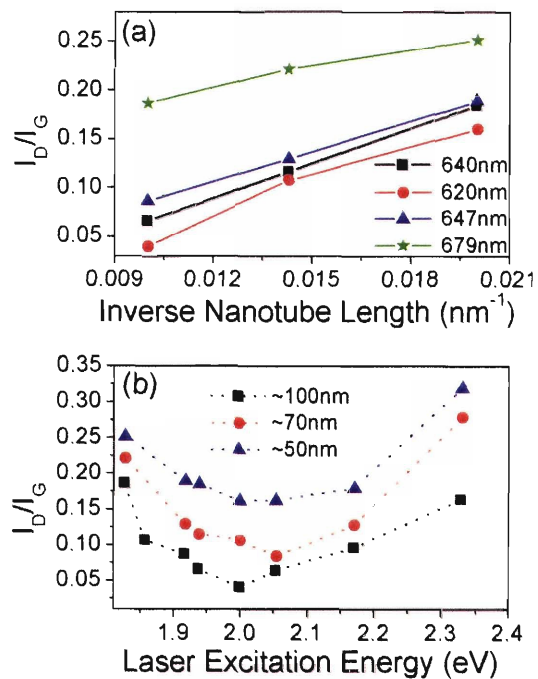


Figure 7-4: (a) D-band intensities (normalized to that of the G-band) plotted as a function of inverse nanotube length, excited at different excitation energies (b) Normalized D-band to G-band intensity ratio,  $I_D/I_G$ , for DNA-wrapped SWNTs of different lengths plotted as a function of laser excitation energy.

in the Raman intensity for the D-band spectra. The D-band is activated in the first-order Raman scattering process by the presence of in-plane defects, vacancies or by finite size effects, all of which lower the crystalline symmetry of the quasi-infinite lattice. In the case of short nanotubes, the increased defect-induced scattering by the end cap and the reduced crystalline length along the nanotube axis are expected to significantly increase the relative D-band intensity through a similar mechanism.

Figure 7-4(a) shows the D-band intensity, normalized to the G-band intensity, as a function of inverse nanotube length at four different values of  $E_{laser}$  that are in resonance with small diameter semiconducting SWNTs. A clear correlation is observed between the average inverse length and the relative D-band intensity,  $I_D/I_G$ , that is commonly plotted in materials characterization studies of disordered carbon systems [154–156].

Figure 7-4 (b) shows the  $I_D/I_G$  ratio as a function of  $E_{laser}$  for samples with different average lengths. Within the energy range below 2eV, where the value of  $E_{laser}$  emphasizes smaller diameter semiconducting nanotubes, the values of  $I_D/I_G$  decrease with increasing  $E_{laser}$  for all of the samples. This observation is consistent with the general D-band behavior observed for  $sp^2$  carbon materials [154–156]. On the other hand, the relative D-band intensity increases with  $E_{laser}$  as the values of  $E_{laser}$  become greater than 2eV. This increase in  $I_D/I_G$  ratio is attributed to a larger fraction of the tubes that come into resonance with  $E_{laser}$  being metallic nanotubes. Our observation is consistent with previous findings that the metallic SWNTs have a larger D-band intensity than semiconducting SWNTs [155, 156]. In this higher excitation energy range where more metallic nanotubes are in resonance, a broad baseline arising from the DNA fluorescence signal is also observed, and this broad fluorescence baseline interferes with the intensity analysis of the weaker intensity IFM features. To avoid confusion, the IFM analysis shown in this chapter has focused on the values of  $E_{laser}$  that are in resonance with semiconducting SWNTs.

Historically, the ratio of the D and G-band intensities ( $I_D/I_G$ ) has been used as a qualitative measure of crystalline size, based on several empirical studies that combine crystallography and spectroscopy [154]. A recent optical study of nanographitic ma-



terials has further established an universal relation regarding the  $E_{laser}$  dependence that applies to the characterization of all graphitic materials [25] and is given by

$$L_{\alpha}(nm) = \frac{560}{E_{laser}^4} \left( \frac{I_D}{I_G} \right)^{-1} \quad (7.1)$$

where  $L_{\alpha}$  corresponds to the crystallite size. In our experiments, the observed nanotube length dependence of  $I_D/I_G$  ratio can be seen as an analog of the crystalline-size effect observed in nano-graphitic materials that has a  $E_{laser}^4$  dependence on the laser excitation energy. The linear correlation observed in our experiments suggests that the  $I_D/I_G$  ratio can be used as a qualitative indicator to estimate the length of the carbon nanotubes. However, the  $I_D/I_G$  dependence on crystalline size,  $L_{\alpha}$ , in the present experiment does not follow Eq. 7.1 closely. Figure 7-5 shows the comparison between the universal relation derived for nano-graphitic materials and our measurements for the short SWNT samples studied here. In general, the  $I_D/I_G$  ratios for SWNT are higher than the corresponding values for nano-graphites at the same laser excitation energy. The curvature and resonance enhancement in SWNTs is probably responsible for these larger values of  $I_D/I_G$ . Additional study will be needed to determine if such a universal relation applies to SWNT systems.

## 7.5 Other Second Order Raman Features

Several second order Raman features, such as the M-band, iTOLA, and G' band features are consistently observed in the spectral region between  $1650\text{cm}^{-1}$  and  $2700\text{cm}^{-1}$  for all values of  $E_{laser}$ . In general, the relative intensities for these observed overtone features are found to have little or no dependence on nanotube length.

Since the M-band and the iTOLA mode are associated with vibrations near the  $\Gamma$  point in which totally symmetric vibrations are involved, we can understand the lack of a length dependence using the same logic as is explained in Section 7.3, where the length dependence of the first order  $\Gamma$  point processes is discussed.

In contrast to the first order D-band process discussed in the previous section, the process associated with the second-order G' band is symmetry-allowed by momentum

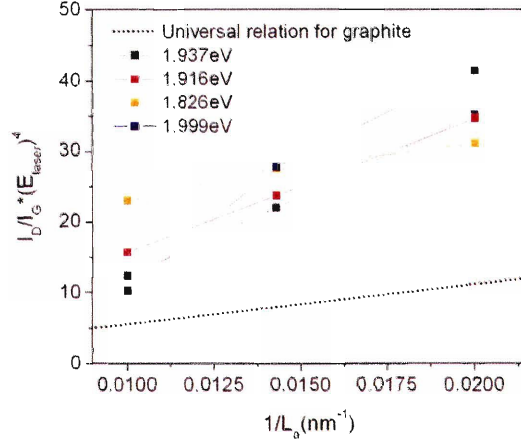


Figure 7-5: A comparison between the length dependence of the  $I_D/I_G$  ratio for short nanotubes samples, excited at multiple laser excitation energies, and the universal relation for the crystalline size dependence of the  $I_D/I_G$  ratio in graphite, empirically determined from nanographites. [25]

conservation requirements. Since no defects or symmetry-breaking mechanism is required in the scattering process, the mode is an intrinsic feature of all  $sp^2$  carbons. As a result, the broken translational symmetry in short nanotubes is not expected to introduce a length dependence into the relative intensity of the  $G'$  band, in agreement with observation.

## 7.6 Summary

In this chapter, a systematic resonance Raman study has been carried out on DNA-wrapped SWNTs as a function of nanotube length, using different values of  $E_{laser}$ , as well as their  $(n, m)$  dependence. We have observed a large increase in Raman and IR mode intensity in the IFM region with decreasing average length. The extent of the Raman intensity increase is found to be dependent on the origin of the IFM features. The changes in the D-band intensity are also examined in the context of the crystalline size effects as the nanotubes become shorter. The correlation observed

between the  $I_D/I_G$  ratio and nanotube length indicates that the  $I_D/I_G$  ratio can be used as a qualitative gauge for estimating the average nanotube length.

# Chapter 8

## Conclusions

### 8.1 Conclusions

The optical studies presented in this thesis have contributed to the understanding of nanotube sciences and one dimensional physics in several respects. Using resonance Raman spectroscopy (RRS) and photoluminescence spectroscopy (PL), a careful characterization is carried out on different DNA-wrapped SWNT samples to study the effects of DNA wrapping on the electronic and vibrational structure of SWNTs. Based on the comparison between the SWNTs wrapped with DNA and SWNTs encapsulated in the more commonly used SDS encapsulating agent, a simple guideline can be established for characterizing SWNTs in different environments. Even though the different wrapping agents and the fractionation process perturb the electronic structure of the nanotubes and shift the excitonic transition energies, this perturbation does not alter the optical properties of the nanotubes enough to affect the  $(n, m)$  identification based on the  $(2n+m=\text{constant})$  family patterns.

The DNA-wrapping not only serves as an encapsulating layer for SWNTs, the layer also provides a means to selectively produce a sample that is highly enriched in one specific  $(n, m)$  species using ion exchange chromatography. The availability of such an enriched sample introduces the possibility to study subtle optical processes that are originally too weak and too confusing to study in an ensemble sample consisting of many different  $(n, m)$  species. By tailoring the range of the excitation energies in

the PL experiment to avoid the strongly resonant electronic transitions, it is possible to separately identify the weaker individual phonon-assisted processes that could not be clearly observed in bulk materials system. The experiments shown in this thesis has identified these discrete phonon assisted relaxation channels in great detail. In light of the recent developments in the excitonic theory of 1D systems, the observed phonon-assisted processes are interpreted and examined in terms of excitonic states. The phonon energies associated with these phonon-assisted transitions in SWNTs mirror the phonon energies observed in its bulk counterpart. On the other hand, in contrast to the optical phonons observed in 3D graphite, the slightly shifted G-band phonon energy observed in PL spectra of SWNTs suggests the presence of a strongly coupled exciton-phonon bound state due to the strong 1D confinement condition. The presence of such exciton-phonon bound state can be well-correlated with previous theoretical prediction, and the experimental result confirms the excitonic nature of the optical transitions observed in semiconducting SWNTs.

To further understand the role of phonon assisted processes in exciton relaxation, the dynamics of such phonon-assisted processes is studied using time-resolved spectroscopy. By using a carefully chosen  $E_{\text{pump}}$  that corresponds to  $E_{11}^{0A_2}(6, 5) + 2\hbar\omega_D$  and probing at  $E_{11}^{0A_2}(6, 5)$ , an intermediate decay time component that is associated with the hot D-band phonon-absorption and relaxation process is identified and studied in detail. In addition to the extensively studied (6, 5) SWNTs, similar mechanisms for the minority species in the sample are also investigated by systematically varying the pump fluence and by varying the values of  $E_{\text{probe}}$ . The detailed similarities and differences in the different channels of band edge exciton population decay mechanisms for the (6, 5), (7, 5) and (8, 3) SWNTs are examined. Photoinduced absorption processes were also observed when the selected values of  $E_{\text{probe}}$  correspond to off-resonance energies. The experimental results suggest that in the event of a multi-phonon assisted relaxation process, it is possible for an additional excitonic state to participate in the relaxation process and give rise to the intermediate relaxation time component. A possible mechanism of this process involving the dark E-symmetry exciton is proposed in Chapter 6. The detailed information obtained from the experimental

studies clarifies the role of hot phonon absorption and emission processes, as well as the Auger process, in the filling and depletion of band edge exciton populations for individual SWNTs. The experimental result also gives insights on how dark excitons predicted by theory might indirectly participate in the exciton relaxation process, and consequently lower the quantum yield significantly in optoelectronic processes.

Lastly, to further understand the structural-property relation for short nanotubes, as the separation techniques are developed to gain further control in nanotube length, a series of resonance Raman study is carried out on DNA-wrapped SWNTs samples that are sorted by length using size exclusion chromatography. The consequences of finite-size effects are examined by monitoring the intensities of the Raman features in the extended intermediate frequency mode (IFM) region between  $600\text{cm}^{-1}$  and  $1500\text{cm}^{-1}$ . Many of the features in the extended IFM region show an increased Raman cross section with decreasing average length. The extent of the Raman intensity increase is found to be dependent on the origin of the IFM features. The changes in the D-band intensity are also examined in the context of the crystalline size effects as the nanotubes become shorter.

## 8.2 Future Studies

Many important questions arise as we learn more about the system of DNA-wrapped SWNTs. These unanswered questions hold promises for important developments in the field, and they will need to be addressed in future works. I will end the chapter with a few suggestions on possible future studies.

The optical characterization of the DNA-wrapped nanotubes has provided guidelines on the characterization of SWNTs that are conjugated with biological species. Since the emphasis of the study was on optical characterization, most of the analysis has been carried out on first order Raman features that gives the direct information on nanotube structures. On the other hand, preliminary data have shown that, all of the DNA-wrapped SWNTs are found to have surprisingly intense and well-defined combination mode features around  $1650\text{-}2200\text{cm}^{-1}$  when the laser excitation energies

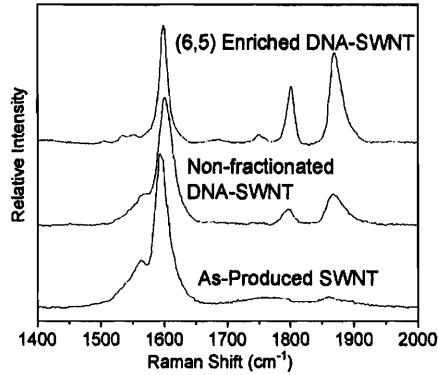


Figure 8-1: (a) Shows a comparison of the intensity of combination modes for different samples that have gone through different wrapping and fractionation procedure. The spectra were taken using  $E_{laser} = 1.63eV$ .

are in the near IR region. Figure 8-1 shows a comparison of the combination mode region spectra for the as-produced CoMoCAT SWNT sample with no DNA wrapping, CoMoCAT SWNT sample wrapped with DNA, and the (6,5) enriched fractionated DNA-SWNT sample. As the SWNT become isolated from one another and with ion exchange fractionation, the relative intensities for these combination modes such as the M-bands and the iTOLA modes increases. As the SWNT become isolated from one another through DNA-wrapping, the relative intensities for these combination modes such as the M-bands and the iTOLA modes increases. It would greatly advance our understanding of the overtone and double resonance process in carbon nanotubes to study such features in detail. Also, since most of the studies carried out in this thesis are done on bulk SWNTs samples. It would clarify our understanding of the bundling effects by depositing the SWNTs on substrate and study the similar optical processes at the single nanotubes level.

The detailed PL study discussed in this thesis has identified the different non-radiative, phonon-assisted relaxation channels in 1D systems. The time-resolved study of these processes further clarified the possible roles of phonon assisted processes and dark excitonic states in the relaxation of excited excitons. On the other hand, the identification of phonon sideband for multi-phonon processes discussed in Chapter 5

has not been studied in detail. Even though multiple transitions were observed and the consistent shift in phonon energy indicates the presence of such state, a more rigorous theoretical investigation that takes into account of the different excitonic states will be needed to understand the nature of a bound state of an exciton and multiple phonons. More detailed time-resolved experiments on enriched sample can also be designed to probe the role of different dark excitons play in exciton relaxation. In addition, a systematic investigation of the fluorescence resonance energy transferring (FRET) mechanism in aligned nanotubes will also yield important information on the distance-dependence of the energy transfer mechanism between different nanotubes.

Furthermore, the broken translational symmetry observed in short nanotubes is expected to have an effect in the relaxation dynamics. Previous study on quantum dots and quantum well has shown that the relaxation dynamics in nano-scaled systems is highly dependent on the dimension of the system. However, no systematic study has been carried out on the size dependence of relaxation dynamics in nanotube system. I expect that a systematic study of the finite-size effects of nanotubes in the time domain will lead to important results.



# Bibliography

- [1] R. Saito, G. Dresselhaus, and M. S. Dresselhaus, *Physical Properties of Carbon Nanotubes* (Imperial College Press, London, 1998).
- [2] R. Saito, M. Fujita, G. Dresselhaus, and M. S. Dresselhaus, *Appl. Phys. Lett.* **60**, 2204–2206 (1992).
- [3] Ge. G. Samsonidze, R. Saito, A. Jorio, M. A. Pimenta, A. G. Souza Filho, A. Grüneis, G. Dresselhaus, and M. S. Dresselhaus, *Journal of Nanoscience and Nanotechnology* **3**, 431–458 (2003).
- [4] J. Maultzsch, S. Reich, C. Thomsen, H. Requardt, and P. Ordejon, *Phys. Rev. Lett.* **92**, 075501 (2004).
- [5] R. A. Jishi, L. Venkataraman, M. S. Dresselhaus, and G. Dresselhaus, *Chem. Phys. Lett.* **209**, 77–82 (1993).
- [6] C. Oshima, T. Aizawa, R. Souda, Y. Ishizawa, and Y. Sumiyoshi, *Solid State Commun.* **65**, 1601 (1988).
- [7] A. Jorio, M. A. Pimenta, A. G. Souza Filho, R. Saito, G. Dresselhaus, and M. S. Dresselhaus, *New Journal of Physics* **5**, 1.1–1.17 (2003).
- [8] C. Fantini, A. Jorio, M. Souza, A. J. Mai Jr., M. S. Strano, M. S. Dresselhaus, and M. A. Pimenta, *Phys. Rev. Lett.* **93**, 147406 (2004).
- [9] V. W. Brar, Ge. G. Samsonidze, G. Dresselhaus, M. S. Dresselhaus, R. Saito, A. K. Swan, M. S. Ünlü, B. B. Goldberg, A. G. Souza Filho, and A. Jorio, *Phys. Rev. B* **66**, 155418 (2002).

- [10] A. Jorio, R. Saito, J. H. Hafner, C. M. Lieber, M. Hunter, T. McClure, G. Dresselhaus, and M. S. Dresselhaus, *Phys. Rev. Lett.* **86**, 1118–1121 (2001).
- [11] R. Saito, A. Jorio, J. H. Hafner, C. M. Lieber, M. Hunter, T. McClure, G. Dresselhaus, and M. S. Dresselhaus, *Phys. Rev. B* **64**, 085312–085319 (2001).
- [12] A. Jorio, M. A. Pimenta, A. G. Souza Filho, Ge. G. Samsonidze, A. K. Swan, M. S. Ünlü, B. B. Goldberg, R. Saito, G. Dresselhaus, and M. S. Dresselhaus, *Phys. Rev. Lett.* **90**, 107403 (2003).
- [13] M. S. Dresselhaus, G. Dresselhaus, R. Saito, and A. Jorio. In *Carbon Nanotubes*, edited by Susumu Saito, Elsevier, Netherlands, 2005.
- [14] R. Saito, A. Jorio, A. G. Souza Filho, G. Dresselhaus, M. S. Dresselhaus, and M. A. Pimenta, *Phys. Rev. Lett.* **88**, 027401 (2002).
- [15] C. Fantini, A. Jorio, M. Souza, L. O. Ladeira, M. A. Pimenta, A. G. Souza Filho, R. Saito, Ge. G. Samsonidze, G. Dresselhaus, and M. S. Dresselhaus, *Phys. Rev. Lett.* **93**, 087401 (2004).
- [16] A. Jorio, A. G. Souza Filho, G. Dresselhaus, M. S. Dresselhaus, R. Saito, J. H. Hafner, C. M. Lieber, F. M. Matinaga, M. S. S. Dantas, and M. A. Pimenta, *Phys. Rev. B* **63**, 245416–(1–4) (2001).
- [17] J. Liu, S. Fan, and H. Dai, *Bulletin of the Materials Research Society* **29**, 244–250 (2004).
- [18] S. M. Bachilo, L. Balzano, J. E. Herrera, F. Pompeo, D. E. Resasco, and R. B. Weisman, *J. Am. Chem. Soc.* **125**, 11186–11187 (2003).
- [19] X. Huang, R. S. Mclean, and M. Zheng, *Anal. Chem.* **77**, 6225 (2005).
- [20] M. S. Strano, *J. Am. Chem. Soc.* **125**, 16148–16153 (2004).
- [21] M. S. Strano, *Nano Lett.* **4**, 543 (2004).

- [22] Y. Miyauchi, S. Chiashi, Y. Murakami, Y. Hayashida, and S. Maruyama, *Chem. Phys. Lett.* **387**, 198 (2004).
- [23] M. J. O'Connell, S. M. Bachilo, X. B. Huffman, V. C. Moore, M. S. Strano, E. H. Haroz, K. L. Rialon, P. J. Boul, W. H. Noon, C. Kittrell, J. Ma, R. H. Hauge, R. B. Weisman, and R. E. Smalley, *Science* **297**, 593–596 (2002).
- [24] S. M. Bachilo, M. S. Strano, C. Kittrell, R. H. Hauge, R. E. Smalley, and R. B. Weisman, *Science* **298**, 2361–2366 (2002).
- [25] L. G. Cancado, K. Takai, T. Enoki, M. Endo, Y. A. Kim, H. Mizusaki, A. Jorio, L. N. Coelho, R. Magalhaes-Paniago, and M. A. Pimenta, *Appl. Phys. Lett.* **88(16)**, 163106 (2006).
- [26] M. S. Dresselhaus, G. Dresselhaus, and Ph. Avouris, *Carbon Nanotubes: Synthesis, Structure, Properties and Applications* (Springer-Verlag, Berlin, 2001), Vol. 80 of *Springer Series in Topics in Appl. Phys.*
- [27] M. S. Dresselhaus, G. Dresselhaus, and P. C. Eklund, *Science of Fullerenes and Carbon Nanotubes* (Academic Press, New York, NY, San Diego, CA, 1996).
- [28] M. S. Dresselhaus, G. Dresselhaus, and R. Saito, *Phys. Rev. B* **45**, 6234 (1992).
- [29] E. Richter and K. R. Subbaswamy, *Phys. Rev. Lett.* **79**, 2738 (1997).
- [30] R. Saito, T. Takeya, T. Kimura, G. Dresselhaus, and M. S. Dresselhaus, *Phys. Rev. B* **59**, 2388–2392 (1999).
- [31] R. A. Jishi, D. Inomata, K. Nakao, M. S. Dresselhaus, and G. Dresselhaus, *J. Phys. Soc. Jpn.* **63**, 2252–2260 (1994).
- [32] M. S. Dresselhaus, G. Dresselhaus, A. Jorio, A. G. Souza Filho, Ge. G. Samsonidze, and R. Saito, *J. Nanosci. Nanotech.* **3**, 19–37 (2003).
- [33] M. A. Pimenta, A. Marucci, S. Empedocles, M. Bawendi, E. B. Hanlon, A. M. Rao, P. C. Eklund, R. E. Smalley, G. Dresselhaus, and M. S. Dresselhaus, *Phys. Rev. B Rapid* **58**, R16016–R16019 (1998).

- [34] S. D. M. Brown, A. Jorio, P. Corio, M. S. Dresselhaus, G. Dresselhaus, R. Saito, and K. Kneipp, *Phys. Rev. B* **63**, 155414 (2001).
- [35] A. Jorio, G. Dresselhaus, M. S. Dresselhaus, M. Souza, M. S. S. Dantas, M. A. Pimenta, A. M. Rao, R. Saito, C. Liu, and H. M. Cheng, *Phys. Rev. Lett.* **85**, 2617–2620 (2000).
- [36] J. Maultzsch, S. Reich, and C. P. Thomsen, *Phys. Rev. B* **65**, 233402 (2002).
- [37] R. Saito, A. Grüneis, Ge. G. Samsonidze, V. W. Brar, G. Dresselhaus, M. S. Dresselhaus, A. Jorio, L. G. Cançado, C. Fantini, M. A. Pimenta, and A. G. Souza Filho, *New Journal of Physics* **5**, 157.1–157.15 (2003).
- [38] L. G. Cançado, M. A. Pimenta, R. Saito, A. Jorio, L. O. Ladeira, A. Grüneis, A. G. Souza Filho, G. Dresselhaus, and M. S. Dresselhaus, *Phys. Rev. B* **66**, 035415 (2002).
- [39] M. A. Pimenta, E. B. Hanlon, A. Marucci, P. Corio, S. D. M. Brown, S. A. Empedocles, M. G. Bawendi, G. Dresselhaus, and M. S. Dresselhaus, *Brazilian J. Phys.* **30**, 423–427 (2000).
- [40] S. D. M. Brown, A. Jorio, G. Dresselhaus, and M. S. Dresselhaus, *Phys. Rev. B* **64**, 073403 (2001).
- [41] A. Grüneis, M. Hulman, Ch. Kramberger, H. Peterlik, H. Kuzmany, H. Kataura, and Y. Achiba. In *Proc. of the XV Int. Winter School on Electronic Properties of Novel Materials (IWEPNM'01)*, edited by H. Kuzmany, J. Fink, M. Mehring, and S. Roth, page 319, American Institute of Physics, Woodbury, N.Y., 2001. *AIP Conference Proceedings*, (2001).
- [42] A. G. Souza Filho, A. Jorio, Ge. G. Samsonidze, G. Dresselhaus, M. A. Pimenta, M. S. Dresselhaus, A. K. Swan, M. S. Ünlü, B. B. Goldberg, and R. Saito, *Phys. Rev. B* **67**, 035427(1–7) (2003).
- [43] C. Thomsen and S. Reich, *Phys. Rev. Lett.* **85**, 5214 (2000).

- [44] C. Thomsen and S. Reich, *Phys. Rev. Lett.* **85**, 5214 (2000).
- [45] J. Kürti, V. Zólyomi, A. Grüneis, and H. Kuzmany, *Phys. Rev. B* **65**, 165433(1–9) (2002).
- [46] A. G. Souza Filho, A. Jorio, Anna K. Swan, M. S. Ünlü, B. B. Goldberg, R. Saito, J. H. Hafner, C. M. Lieber, M. A. Pimenta, G. Dresselhaus, and M. S. Dresselhaus, *Phys. Rev. B* **65**, 085417 (2002).
- [47] A. G. Souza Filho, A. Jorio, Ge. G. Samsonidze, G. Dresselhaus, M. S. Dresselhaus, A. K. Swan, M. S. Ünlü, B. B. Goldberg, R. Saito, J. H. Hafner, C. M. Lieber, and M. A. Pimenta, *Chem. Phys. Lett.* **354**, 62–68 (2002).
- [48] A. G. Souza Filho, A. Jorio, G. Dresselhaus, M. S. Dresselhaus, R. Saito, A. K. Swan, M. S. Ünlü, B. B. Goldberg, J. H. Hafner, C. M. Lieber, and M. A. Pimenta, *Phys. Rev. B* **65**, 035404–(1–6) (2002).
- [49] M. S. Dresselhaus, G. Dresselhaus, A. Jorio, A. G. Souza Filho, and R. Saito, *Carbon* **40**, 2043–2061 (2002).
- [50] S. D. M. Brown, P. Corio, A. Marucci, M. A. Pimenta, M. S. Dresselhaus, and G. Dresselhaus, *Phys. Rev. B* **61**, 7734–7742 (March 2000).
- [51] Carbon nanotube can be thought as a sheet of graphite rolled up to form a cylinder. The structure is defined by its diameter ( $d_t$ ) and chiral angle ( $\theta$ ). The  $d_t$  and  $\theta$  nanotube parameters are well represented by the chiral vector  $\mathbf{C}_h = n\mathbf{a}_1 + m\mathbf{a}_2$  that spans the nanotube circumference and is defined by the two integers  $(n, m)$  giving  $\mathbf{C}_h$  with respect to the 2D graphite basis vectors  $\mathbf{a}_1$  and  $\mathbf{a}_2$ . These two simple geometric parameters  $(d_t, \theta)$  or  $(n, m)$  are indeed responsible for the large diversity of nanotubes, each  $(n, m)$  representing a different molecule with different energy levels and physical properties.
- [52] L. Alvarez, A. Righi, T. Guillard, S. Rols, E. Anglaret, D. Laplaze, and J.-L. Sauvajol, *Chem. Phys. Lett.* **316**, 186–190 (2000).

- [53] H. Son, Y. Hori, S. G. Chou, D. Nezich, Ge. G. Samsonidze, G. Dresselhaus, M. S. Dresselhaus, and E. Barros, *Appl. Phys. Lett.* **85**, 4744–4746 (2004). November 29, 2004 issue of *Virtual Journal of Nanoscale Science & Technology*.
- [54] S. G. Chou, H. B. Ribeiro, E. Barros, A. P. Santos, D. Nezich, Ge. G. Samsonidze, C. Fantini, M. A. Pimenta, A. Jorio, F. Plentz Filho, M. S. Dresselhaus, G. Dresselhaus, R. Saito, M. Zheng, G. B. Onoa, E. D. Semke, A. K. Swan, M. S. Ünlü, and B. B. Goldberg, *Chem. Phys. Lett.* **397**, 296–301 (2004).
- [55] S. Niyogi, M. A. Hamon, H. Hu, B. Zhao, P. Bhowmik, R. Sen, M. E. Itkis, and R. C. Haddon, *Acc. Chem. Res.* **35**, 1105–1113 (2002).
- [56] A. Ugawa, A. G. Rinzler, and D. B. Tanner, *Phys. Rev. B* **60**, R11305 (1999).
- [57] M. Y. Sfeir, F. Wang, L. Huang, C.-C. Chuang, J. Hone, S. P. O'Brien, T. F. Heinz, and L. E. Brus, *Science* **306**, 1540 (2004).
- [58] E. B. Barros, , A. Jorio, G. Dresselhaus, and M. S. Dresselhaus, (2006).
- [59] R. B. Capaz (Private Communication).
- [60] H. Zhao, S. Mazumdar, et al., *Phys. Rev. Lett.* **93**, 157402 (2004).
- [61] D.S. Bethune, C.H. Kiang, M.S. DeVries, G. Gorman, R. Savoy, and R. Beyers, *Nature* **363**, 605 (1993).
- [62] C. Journet, W.K. Maser, P. Bernier, A. Loiseau, M. Lamy de la Chapelle, S. Lefrant, P. Deniard, R. Lee, and J.E. Fischer, *Nature* **388**, 756 (1997).
- [63] A. Thess, R. Lee, P. Nikolaev, H. Dai, J. Robert P. Petit, C. Xu, Y.H. Lee, S.G. Kim, A.G. Rinzler, D.T. Colbert, G.E. Scuseria, D. Tomnek, J.E. Fischer, and R.E. Smalley, *Science* **273**, 483 (1996).
- [64] M. S. Dresselhaus, G. Dresselhaus, K. Sugihara, I. L. Spain, and H. A. Goldberg, *Graphite Fibers and Filaments* (Springer-Verlag, Berlin, 1988), Vol. 5 of *Springer Series in Materials Science*.

- [65] H. O. Pierson, *Handbook of Chemical Vapor Deposition* (Noyes Publications, Park Ridge, NJ, 1992).
- [66] M. J. Hampden-Smith and T.T. Kodas, *Chem. Vap. Deposition* **1**, 8 (1995).
- [67] M. Endo, A. Oberlin, , and T. Koyama, *Jpn. J. Appl. Phys.* **16**, 1519 (1977).
- [68] H.G. Tennent, U.S. Patent No. **4, 663**, 230 (1987).
- [69] J. Kong, H. T. Soh, A. M. Casswell, C. F. Quate, and H. Dai, *Nature (London)* **395**, 878–881 (1998).
- [70] M. Endo, K. Takeuchi, K. Kobori, K. Takahashi, H. Kroto, and A. Sarkar, *Carbon* **33**, 873 (1995).
- [71] H. Dai, G. Rinzler, P. Nikolaev, D.T. Colbert A. Thess, and R.E. Smalley, *Chem. Phys. Lett.* **260**, 471 (1996).
- [72] J. Kong, A.M. Cassell, and H.J. Dai, *Chem. Phys. Lett.* **292**, 567 (1998).
- [73] J.H. Hafner, M.J. Bronikowski, B.R. Azamian, P. Nikolaev, A.G. Rinzler, D.T. Colbert, K.A. Smith, and R.E. Smalley, *Chem. Phys. Lett.* **296**, 195 (1998).
- [74] A. V. Nilolaev, M. J. Bronikowski, R. K. Bradley, F. Rohmund, D. T. Colbert, K. A. Smith, and R. E. Smalley, *Chem. Phys. Lett.* **313**, 91–97 (1999).
- [75] M. J. Bronikowski, P. A. Willis, D. T. Colbert, K. A. Smith, and R. E. Smalley, *J. Vacuum Sci. Technol. A* **19**, 1800 (2001).
- [76] B. Zheng, C. Lu, G. Gu, A. Makarovski, G. Finkelstein, and J. Liu, *Nano Lett.* **2**, 895 (2002).
- [77] K. Bladh, L.K.L. Falk, and F. Rohmund, *Appl. Phys. A.* **70**, 317 (2000).
- [78] B. Kitiyanan, W.E. Alvarez, J.H. Harwell, and D.E. Resasco, *Chem. Phys. Lett.* **317**, 497 (2000).

- [79] W.E. Alvarez, B. Kitiyanan, A. Borgna, and D.E. Resasco, *Carbon* **39**, 547 (2001).
- [80] H.C. Choi, W. Kim, W. Wang, and H.J. Dai, *J. Phys. Chem. B* **106**, 12361 (2002).
- [81] Y.M. Li, W. Kim, Y.G. Zhang, M. Rolandi, D.W. Wang, and H.J. Dai, *J. Phys. Chem. B* **105**, 11424 (2001).
- [82] Z.K. Tang, H.D. Sun, J. Wang, J. Chen, and G. Li, *Appl. Phys. Lett.* **73**, 2287 (1998).
- [83] L. An, J.M. Owens, L.E. McNeil, and J. Liu, *J. Am. Chem. Soc.* **124**, 13688 (2002).
- [84] G.S. Duesberg, J. Muster, V. Krstic, M. Burghard, and S. Roth, *Appl. Phys. A* **67**, 117 (1998).
- [85] M.F. Islam, E. Rojas, D.M. Bergey, A.T. Johnson, and A.G. Yodh, *Nano Lett.* **3**, 269 (2003).
- [86] M. Zheng, A. Jagota, E. D. Semke, B. A. Diner, R. S. Mclean, S. R. Lustig, R. E. Richardson, and N. G. Tassi, *Nature Materials* **2**, 338 (2003).
- [87] S.K. Doorn, I.R.F. Fields, H. Hu, M. Hamon, R.C. Haddon, J.P. Selegue, and V. Majidi, *J. Am. Chem. Soc.* **124**, 3169 (2002).
- [88] Chattopadhyay D., Lastella S., Kim S., and Papadimitrakopoulos F., *J. Am. Chem. Soc.* **124**, 728–729 (2002).
- [89] M.A. Hamon, J. Chen, H. Hu, Y. Chen, A.M. Rao, P.C. Eklund, and R.C. Haddon, *Adv. Mater.* **11**, 834 (1999).
- [90] Ge. G. Samsonidze, S. G. Chou, A. P. Santos, V. W. Brar, G. Dresselhaus, M. S. Dresselhaus, A. Selbst, A. K. Swan, M. S. Ünlü, B. B. Goldberg, D. Chattopadhyay, S. N. Kim, and F. Papadimitrakopoulos, *Appl. Phys. Lett.* **85**, 1006–1008 (2004). URL: <http://dx.doi.org/10.1063/1.1777814>.



- [91] R. Krupke, F. Hennrich, H. V. Löhneysen, and M. M. Kappes, *Science* **301**, 344 (2003).
- [92] M.S. Strano, C.A. Dyke, M.L. Usrey, P.W. Barone, M.J. Allen, H. Shan, C. Kittrell, R.H. Hauge, J.M. Tour, and R.E. Smalley, *Science* **301**, 1519 (2003).
- [93] M. Zheng, B. A. Diner, et al., *J. Am. Chem. Soc.* **126**, 15390 (2004).
- [94] M. Zheng, M. S. Strano, A. P. Santos, S. G. Chou, G. B. Onoa, and E. Semke, *Science* **302**, 1545–1548 (2003).
- [95] G. S. Duesberg, W. J. Blau, H. J. Byrne, J. Muster, M. Burghard, and S. Roth, *Chem. Phys. Lett.* **310**, 8–14 (1999).
- [96] E. Farkas, M. Elizabeth Anderson, Z. Chen, and A.G. Rinzler, *Chem. Phys. Lett.* **363**, 111 (2002).
- [97] Chen G., Sumanasekera G. U., Pradhan B. K., Gupta R., Eklund P. C., Bronikowski M. J., and Smalley R. E., *J. Nanosci. Nanotech.* **2**, 621–626 (2002).
- [98] V. W. Brar, Ge. G. Samsonidze, A. P. Santos, S. G. Chou, D. Chattopadhyay, S. N. Kim, F. Papadimitrakopoulos, M. Zheng, A. Jagota, G. B. Onoa, A. K. Swan, M. S. Ünlü, B. B. Goldberg, G. Dresselhaus, and M. S. Dresselhaus, *J. Nanosci. & Nanotech.* **5**, 209–228 (2005).
- [99] S. M. Bachilo, L. Balzano, J. E. Herrera, F. Pompeo, D. E. Resasco, and R. B. Weisman, *Journal of American Chemical Society* **125**, 11186 (2003).
- [100] D. Resasco, W. E. Alvarez, F. Pompeo, L. Balzano, J. E. Herrera, H. Kitiyanan, and A. Borgan, *Journal of Nanoparticles Research* **4**, 131–136 (2002).
- [101] A. G. Souza Filho, A. Jorio, J. H. Hafner, C. M. Lieber, R. Saito, M. A. Pimenta, G. Dresselhaus, and M. S. Dresselhaus, *Phys. Rev. B* **63**, 241404R (2001).
- [102] J. Lefebvre, P. Finnie, and Y. Homma, *Phys. Rev. B* **70**, 045419 (2004).

- [103] J. Lefebvre, J. M. Fraser, P. Finnie, and Y. Homma, *Phys. Rev. B* **69**, 075403 (2004).
- [104] J. Lefebvre, J. M. Fraser, Y. Homma, and P. Finnie, *Appl. Phys. A* **78**, 1107 (2004).
- [105] H.Htoon, M.J.O'Connell, P.J.Cox, S.K.Doorn, and V.I.Klimov, *Phys. Rev. Lett.* **93**, 027401 (2004).
- [106] J. Jiang, R. Saito, A. Grüneis, S. G. Chou, Ge. G. Samsonidze, A. Jorio, G. Dresselhaus, and M. S. Dresselhaus, *Phys. Rev. B* **71**, 045417–1–9 (2005).
- [107] D. E. Watson, , 1992).
- [108] V. Perebeinos, J. Tersoff, and Ph. Avouris, *Phys. Rev. Lett.* **92**, 257402 (2004).
- [109] /cond-mat/papers/0508/0508232.pdf.
- [110] F. Plentz, H. B. Ribeiro, A. Jorio, M. S. Strano, and M. A. Pimenta, *Phys. Rev. Lett.* **95**, 247401 (2005).
- [111] X. Qiu, M. Freitag, V. Perebeinos, and P. Avouris, *Nano Lett.* **5**, 749–752 (2005).
- [112] L. Stryer and R. Haugland, *Proc Natl Acad Sci U S A* **58**, 719–726 (1967).
- [113] T. Goto and Y. Nishina, *Phys. Rev. B* **17**, 4565 (1978).
- [114] R. Heitz et al., *Phys. Rev. B* **64**, 241305(R) (2001).
- [115] R. Heitz et al., *Phys. Rev. B* **56**, 10435 (1997).
- [116] H. Benisty et al., *Phys. Rev. B.* **51**, 13281 (1995).
- [117] S. Moehl et al., *J. Appl. Phys.* **93**, 6265 (2003).
- [118] H. Zhao et al., *Phys. Rev. B* **66**, 08533 (2002).
- [119] H. Zhao et al., *Appl. Phys. Lett.* **80**, 1391 (2002).

- [120] S. M. Bachilo, M. S. Strano, C. Kittrell, R. H. Hauge, R. E. Smalley, and R. B. Weisman, *Science* **298**, 2361–2366 (2002).
- [121] M. Jones, C. Engtrakul, W. K. Metzger, R. J. Ellingson, A. J. Nozik, M. J. Heben, and G. Rumbles, *Phys. Rev. B* **71**, 115426 (2005).
- [122] F. Wang, G. Dukovic, L. E. Brus, and T. F. Heinz, *Phys. Rev. Lett.* **92**, 177401 (2004).
- [123] F. Wang, G. Dukovic, E. Knoesel, L. E. Brus, T. F. Heinz, et al., *Phys. Rev. B* **70**, 241403(R) (2004).
- [124] Y. Z. Ma, J. Stenger, J. Zimmermann, S. M. Bachilo, R. E. Smalley, R. B. Weisman, and G. R. Fleming, *J. Chem. Phys.* **120**, 3368 (2004).
- [125] Y. Z. Ma, L. Valkunas L, S. L. Dexheimer, S. M. Bachilo, and G. R. Fleming, *Phys. Rev. Lett.* **94**, 157402 (2005).
- [126] J. Kono et al., *Appl. Phys. A* **78**, 1093–1098 (2004).
- [127] O. J. Korovyanko, C.-X. Sheng, Z.V. Vardeny, A. B. Dalton, R. H. Baughman, et al., *Phys. Rev. Lett.* **92**, 017403 (2004).
- [128] J. S. Lauret, C. Voisin, G. Cassabois, P. Roussignol, C. Delalande, L. Capes, E. Valentin, and O. Jost, *Semicond. Sci. Technol.* **19**, S486–S488 (2004).
- [129] G. N. Ostojic, S. Zaric, J. Kono, M. S. Strano, V. C. Moore, R. H. Hauge, and R. E. Smalley, *Phys. Rev. Lett.* **92**, 117402 (2004).
- [130] G. N. Ostojic, S. Zaric, J. Kono, V. C. Moore, R. H. Hauge, and R. E. Smalley, *Phys. Rev. Lett.* **94**, 097401 (2005).
- [131] A. Hagen and T. Hertel, *Nanoletters* **3**, 383–388 (2003).
- [132] A. Hagen, G. Moos, V. Talalaev, and T. Hertel, *Appl. Phys. A* **78**, 1137–1145 (2004).

- [133] D. J. Styers, S. P. Ellison, C. Park, K. E. Wise, J. M. Papanikolas, et al., *Journal of Physical Chemistry A* **109**, 289–292 (2005).
- [134] Rubtsov et al., *Appl. Phys. A* **79**, 1747 (2005).
- [135] S. G. Chou, F. Plentz Filho, J. Jiang, R. Saito, D. Nezich, H. B. Ribeiro, A. Jorio, M. A. Pimenta, Ge. G. Samsonidze, A. P. Santos, M. Zheng, G. B. Onoa, E. D. Semke, G. Dresselhaus, and M. S. Dresselhaus, *Phys. Rev. Lett.* **94**, 127402 (2005).
- [136] F. Wang, G. Dukovic, L. E. Brus, T. F. Heinz, et al., *Science* **308**, 838 (2005).
- [137] C. Rulliere, *Femtosecond Laser Pulses: Principles and Experiment* (Springer Science + Business Media, Inc.).
- [138] C. J. Fecko, J. J. Loparo, and A. Tokmakoff, *Optics Communications* **241**, 521–528.
- [139] C. D. Spataru, S. Ismail-Beigi, R. B. Capaz, and S. Louie, *Phys. Rev. Lett.* **95**, 247402 (2005).
- [140] V. Perebeinos, J. Tersoff, and P. Avouris\*, *Phys. Rev. Lett.* **94**, 086802 (2005).
- [141] J. S. Lauret, C. Voisin, G. Cassabois, C. Delalande, Ph. Roussignol, O. Jost, and L. Capes, *Phys. Rev. Lett.* **90**, 057404 (2003).
- [142] A. Hagen, M. Steiner, M.B. Raschke, Ch. Lienau, T. Hertel, H. Qian, A.J. Meixner, and A. Hartschuh, *Phys. Rev. Lett.* **95**, 197401 (2005).
- [143] F. Wang, G. Dukovic, L. E. Brus, and T. F. Heinz, *Phys. Rev. Lett.* **92**, 177401–1–4 (2004).
- [144] J.-P. Yang, M. M. Kappes, H. Hippler, A.-N. Unterreiner, et al., *Phys. Chem. Chem. Phys.* **7**, 512 (2005).
- [145] A. Maeda, S. Matsumoto, H. Kishida, T. Takenobu, Y. Iwasa, M. Shiraishi, M. Ata, and H. Okamoto, *Phys. Rev. Lett.* **94**, 047404 (2005).

- [146] A. Rochefort, D. R. Salahub, and P. Avouris, *J. of Phys. Chem. B* **103**, 641–646 (1999).
- [147] A. Rahmani, J.-L. Sauvajol, S. Rols, and C. Benoit, *Phys. Rev. B* **66**, 125404 (2002).
- [148] L. Alvarez, A. Righi, S. Rols, E. Anglaret, and J. L. Sauvajol, *Chem. Phys. Lett.* **320**, 441–447 (2000).
- [149] C. Fantini, E. Cruz, A. Jorio, M. Terrones, H. Terrones, Van Lier G, J.-C. Charlier, M. S. Dresselhaus, R. Saito, Y. A. Kim, T. Hayashi, H. Muramatsu, M. Endo, and M. A. Pimenta, *Phys. Rev. B* **72**, 085446 (2006).
- [150] H. B. Son (Unpublished Work).
- [151] M. Zheng (Private communication).
- [152] U. J. Kim, X. M. Liu, C. A. Furtado, G. Chen, R. Saito, J. Jiang, M. S. Dresselhaus, and P. C. Eklund, *Phys. Rev. Lett.* **95**, 157402 (2005).
- [153] C. Fantini, A. Jorio, M. Souza, R. Saito, Ge. G. Samsonidze, M. S. Dresselhaus, and M. A. Pimenta, *Phys. Rev. B* page in press (2005).
- [154] F. Tuinstra and J. L. Koenig, *J. Phys. Chem.* **53**, 1126 (1970).
- [155] S. D. M. Brown, A. Jorio, M. S. Dresselhaus, and G. Dresselhaus, *Phys. Rev. B* **64**, 073403–(1–4) (2001).
- [156] M. A. Pimenta, A. Jorio, S. D. M. Brown, A. G. Souza Filho, G. Dresselhaus, J. H. Hafner, C. M. Lieber, R. Saito, and M. S. Dresselhaus, *Phys. Rev. B* **64**, 041401–(1–4) (2001).

### **Education**

2001 – present Massachusetts Institute of Technology Cambridge, MA  
Doctor of Philosophy in Physical Chemistry, expected June 2006.  
Advisor: Prof. Mildred S. Dresslehaus

1997– 2001 Bryn Mawr College. *Cum Laude* Bryn Mawr, PA  
Bachelor of Art in Chemistry and Physics, with honor in Physical Chemistry, 2001

### **Research Experience**

2001 – present *Doctoral Research*  
MIT, Dept. of Chemistry (Prof. M. S. Dresselhaus in Electrical Engineering/Physics) Cambridge, MA

- Examine the mechanism of phonon-assisted relaxation processes in one dimensional systems using resonance Raman, photoluminescence. The dynamics of such phonon-assisted processes is further studied using time-resolved measurements.
- Evaluated the finite-length effects for short nanotubes sorted using size exclusion chromatography using resonance Raman spectroscopy.
- Developed optical methods to evaluate separation efficiency of different nanotube separation methods. The same optical characterization technique was applied to biologically assisted sorting and assembly of nanotube devices by Dupont.

2000– 2001 *Undergraduate Honors Research Supported by the Dorothy Nepper Marshall Fellowship*  
Bryn Mawr College, Dept. of Chemistry (Prof. M. Francl) Bryn Mawr, PA

- Calculated transition state species of alkylaluminum reactions using Density Functional Theory.

2000 *Undergraduate Summer Research*  
Academia Sinica, Center of Atomic and Molecular Science (Dr. X. Yang) Taipei, Taiwan

- Carried out experiments using the Rydberg tagging technique to study the  $D_2 + H_2O$  reaction dynamics.

1999– 2000 *Undergraduate Research*  
Haverford College, Dept. of Chemistry (Prof. C. Miller) Haverford, PA

- Analyzed microwave spectra of  $DNO_3$  and calculated the  $O_3 + Cl^-$  reaction energy path with DFT theory.
- The work has resulted in one publication in Journal of Molecular Spectroscopy.

1999 *NSF Summer Research Experience for Undergraduate Students*  
University of Pittsburgh, Dept. of Chemistry (Prof. D. Pratt) Pittsburgh, PA

- Carried out high resolution spectroscopy of diphenylacetylene dendrimer and performed ab initio calculations to identify excited electronic state in diphenylacetylene molecules in gas phase.
- The work has resulted in one publication in *Chemical Physics Letters*.

### **Teaching Experience:**

Fall 2004 Teaching Assistant for Graduate Solid State Physics course at MIT Electrical Engineering Department  
Fall 2001 Teaching Assistant for Introductory Chemistry at MIT Chemistry Department  
2000 – 2001 Teaching Assistant for Physical Chemistry as a Marshall Teaching Fellow at Bryn Mawr College

### **Awards:**

2005 Silver Award, Materials Research Society Graduate Student Award (Fall Meeting)  
2004 Morse Travel Fellowship  
2001 General Electric Fellowship  
2001 American Chemical Society Scholastic Achievement Award  
2001 NSF Graduate Fellow competition Honorable Mention  
2000 Dorothy Nepper Marshall Fellowship

## Conferences Presentations (Oral and Poster):

2004/05/06 American Physical Society March Meeting, Oral Presentations  
2004/05 International Conf. of Sci. and Tech. of Carbon Nanotubes, Poster Presentations  
2002/03/04/05/06 Materials Research Society Fall Meeting, Oral and Poster Presentations  
2002/03/04/05 Dupont-MIT Alliance Student Symposium, Oral Presentations

## Invited Talks:

2005 MIT Nanotube Club monthly symposium  
2004 MIT Modern Optical Spectroscopy Fall Seminar Series.  
2002 New England Microscopy Society Fall Meeting.

## Publication List:

**S. G. Chou**, H. Son, M. Zheng, A. Jorio, M. S. Dresselhaus. Optical Studies of Finite Length Effects in Singled Walled Carbon Nanotubes. *Manuscript in Preparation*.

**S. G. Chou**, H. Son, M. Zheng, A. Jorio, M. S. Dresselhaus. D-band Intensity Dependence on Crystalline Size Effects in Singled Walled Carbon Nanotubes. *Manuscript in Preparation*.

J. Jiang, R. Saito, Ge. G. Samsonidze, A. Jorio, S. G. Chou, G. Dresselhaus, M. S. Dresselhaus. Chirality Dependence of the Exciton Effects in Single-Wall Carbon Nanotubes. *Phys. Rev. B. submitted (2006)*

F. Villapando-Paez, A. Zamudio, A. L. Elias, H. Son, E. B. Barros, S. G. Chou, Y.A. Kim, H. Muramatsu, T. Hayashi, J. Kong, H. Terrones, G. Dresselhaus, M. Endo, M. Terrones and M. S. Dresselhaus, Synthesis and Characterization of Long Strands of Nitrogen Doped Single-Walled Carbon Nanotubes. *Chem. Phys. Lett. in press (2006)*

J. Jiang, R. Saito, Ge. G. Samsonidze, **S. G. Chou**, A. Jorio, Dresselhaus, M. S. Dresselhaus. Electron-Phonon Matrix Elements in Single-Wall Carbon Nanotubes. **Phys. Rev. B. 72**, 235408 (2005)

**S. G. Chou**, M. F. DeCamp, J. Jiang, Ge. G. Samsonidze, E. B. Barros, F. Plentz, A. Jorio, M. Zheng, G. B. Onoa, E. D. Semke, A. Tokmakoff, R. Saito, G. Dresselhaus, M. S. Dresselhaus. A Study Of Phonon-Assisted Exciton Relaxation Dynamics For A (6,5) Enriched DNA-Wrapped Single Walled Carbon Nanotube Sample. **Phys. Rev. B. 72**, 195415 (2005)

(Selected to be featured in the November 28<sup>th</sup>, 2005 issue of Virtual Journal of Nanoscale Science & Technology).  
(Selected to be featured in the December, 2005 issue of Virtual Journal of Ultrafast Science).

M. Endo, M. Terrones, Y. A. Kim, T. Hayashi, H. Muramatsu, R. Saito, F. Villapando, **S. G. Chou**, M. S. Dresselhaus. Nanotube Coalescence Inducing Mode: A Novel Vibrational Mode in Carbon Systems. **Small**, in press (2006)

J. Jiang, R. Saito, A. Grüneis, **S. G. Chou**, Ge. G. Samsonidze, A. Jorio, G. Dresselhaus, M. S. Dresselhaus. Intensity Of The Resonance Raman Excitation Spectra Of Single-Wall Carbon Nanotubes. **Phys. Rev. B. 71**, 205420 (2005).

M. S. Dresselhaus, Ge. G. Samsonidze, **S. G. Chou**, G. Dresselhaus, J. Jiang, R. Saito, A. Jorio. Recent Advances in Carbon Nanotube Photophysics. **Physica E**, 29 (3-4): 443-446 (2005).

**S. G. Chou**, F. Plentz, J. Jiang, R. Saito, D. Nezich, H. B. Ribeiro, A. Jorio, and co-authors. Photo-Excited Electron Relaxation Process Observed In Photoluminescence Spectroscopy Of DNA-Wrapped Carbon Nanotube. **Phys. Rev. Lett. 94** (12), 127402 (2005).

(Selected to be featured in the April 11<sup>th</sup>, 2005 issue of Virtual Journal of Nanoscale Science & Technology).

J. Jiang, R. Saito, A. Grüneis, **S. G. Chou**, Ge. G. Samsonidze, A. Jorio, A. G. Souza Filho, and co-authors. Photo-Excited Electron Relaxation Processes In Single Wall Carbon Nanotubes. **Phys. Rev. B. 71**(1), 045417 (2005).

**S. G. Chou**, F. Plentz, J. Jiang, R. Saito, D. Nezich, H. B. Ribeiro, A. Jorio, and co-authors. Photo-Excited Electron Relaxation Process Observed In Photoluminescence Spectroscopy Of DNA-Wrapped Carbon Nanotube. **MRS Proceedings**, Volume 737, Paper HH13.13, Materials Research Society Press, Warrendale, PA (2005).

A. Jorio, L. G. Cancado, B. R. A. Neves, M. Souza, C. Fantini, M. A. Pimenta, G. Medeiros-Ribeiro, Ge. G. Samsonidze, **S. G. Chou**, G. Dresselhaus, M. S. Dresselhaus and co-authors. Resonance Raman Spectroscopy To Study And Characterize Defects On Carbon Nanotubes And Other Nano-Graphite Systems. **MRS Proceedings**, Volume 737, Materials Research Society Press, Warrendale, PA (2005).

- Ge. G. Samsonidze, R. Saito, J. Jiang, A. Gruneis, N. Kobayashi, A. Jorio, **S. G. Chou**, G. Dresselhaus, M. S. Dresselhaus. Corrections to the Optical Transition Energies in Single-Wall Carbon Nanotubes of Smaller Diameters, **MRS Proceedings**, Volume 737, Materials Research Society Press, Warrendale, PA (2005).
- J. Jiang, R. Saito, A. Gruneis, **S. G. Chou**, Ge. G. Samsonidze, A. Jorio, G. Dresselhaus, M. S. Dresselhaus. Intensity of The Resonance Raman Excitation Spectra Of Single-Wall Carbon Nanotubes. **Phys. Rev. B.** 71(1), 205420 (2005).
- Ge. G. Samsonidze, R. Saito, N. Kobayashi, A. Gruneis, J. Jiang, A. Jorio, **S. G. Chou**, and co-authors. Family Behavior Of The Optical Transition Energies In Single-Wall Carbon Nanotubes of Smaller Diameters **Appl. Phys. Lett.** 85, 5703-5705 (2004).
- S. G. Chou**, H. B. Ribeiro, E. Barros, A. P. Santos, D. Nazich, Ge. G. Samsonidze, C. Fantini, and co-authors. Optical Characterization Of DNA Wrapped Carbon Nanotube Hybrids. **Chem. Phys. Lett.** 397, 296-301(2004).
- H. Son, Y. Hori, **S. G. Chou**, Ge. G. Samsonidze, D. Nazich, M. S. Dresselhaus, and co-authors. Environmental Effect On The Raman Spectra Of Individual Single Wall Carbon Nanotubes: Suspended And Grown On Polysilicon. **Appl. Phys. Lett.** 85, 4744 (2004).
- V. W. Brar, Ge. G. Samsonidze, A. P. Santos, **S. G. Chou**, and co-authors. Resonance Raman Spectroscopy Characterization Of Single-Wall Carbon Nanotube Separation By Their Metallicity And Diameter. **J. Nanosc. and Nanotech.** 5, 209-228 (2005).
- S. B. Cronin, T. Barnett R, M. Tinkham, **S. G. Chou**, O. Rabin, M. S. Dresselhaus, A. K. Swan, and co-authors. Electrochemical Gating of Individual Single-Wall Carbon Nanotubes Observed by Electron Transport Measurements and Resonant Raman Spectroscopy. **Appl. Phys. Lett.** 84 (12): 2052-2054 (2004).
- M. Zheng, A. Jagota, M. S. Strano, A. P. Santos, P. Barone, **S. G. Chou**, B. A. Diner, and co-authors. Structure-Based Carbon Nanotube Sorting By Sequence-Dependent DNA Assembly. **Science** 302 (5650): 1545-1548 (2003).
- A. G. Souza Filho, **S. G. Chou**, Ge. G. Samsonidze, G. Dresselhaus, M. S. Dresselhaus, and co-authors. Stokes and Anti-Stokes Raman Spectra Of Small Diameter Isolated Carbon Nanotubes. **Phys. Rev. B** 69 (11), 115428 (2004).
- Ge. G. Samsonidze, **S. G. Chou**, A. P. Santos, A. Selbst, G. Dresselhaus, M. S. Dresselhaus, and co-authors. Quantitative Evaluation of The Octadecylamine-Assisted Bulk Separation Of Semiconducting And Metallic Single-Wall Carbon Nanotubes By Resonance Raman Spectroscopy. **Appl. Phys. Lett.** 85 (6): 1006-1008 (2004).
- Feng Li, **S. G. Chou**, Wencai Ren, J. A. Gardecki, and co-authors. Identification Of The Constituents Of Double-Walled Carbon Nanotubes Using Raman Spectra Taken With Different Laser-Excitation Energies. **J. Mat. Res.** 18 (5): 1251-1258 (2003).
- P. Corio, P. S. Santos, V. W. Brar, Ge. G. Samsonidze, **S. G. Chou**, M. S. Dresselhaus. Potential Dependent Surface Raman Spectroscopy Of Single Wall Carbon Nanotube Film On Platinum Electrodes. **Chem. Phys. Lett.** 370, 675 (2003).
- S. G. Chou**, M. S. Dresselhaus, E. B. Humphreys, and co-authors. Raman Analysis of Carbon Nanotube Bundles for Bio-electronic Applications. Quantum Confined Semiconductor Nanostructures: **MRS Proceedings**, Volume 737, Paper F8.10, Materials Research Society Press, Warrendale, PA (2002).
- S. G. Chou**, D. T. Petkie, R. A. H. Butler, C. E. Miller. Rotational Spectroscopy of DNO<sub>3</sub>. **J. Mol. Spec.**, 211(2): 284-285 (2002).
- D. R. Borst, **S. G. Chou**, D. W. Pratt. Identification Of The Light-Absorbing States In Toluene With Potential Relevance To Self-Similar Phenylacetylene Dendrimers. **Chem. Phys. Lett.** 343 (3-4): 289-295 (2001).